THE UNIVERSITY *of* EDINBURGH

Deformable Models for Adaptive Radiotherapy Planning

Kun Cheng

Doctor of Philosophy

THE UNIVERSITY OF EDINBURGH

2015

To the years in Edinburgh,

With You Guys

Abstract

Radiotherapy is the most widely used treatment for cancer, with 4 out of 10 cancer patients receiving radiotherapy as part of their treatment. The delineation of gross tumour volume (GTV) is crucial in the treatment of radiotherapy. An automatic contouring system would be beneficial in radiotherapy planning in order to generate objective, accurate and reproducible GTV contours. Image guided radiotherapy (IGRT) acquires patient images just before treatment delivery to allow any necessary positional correction. Consequently, real-time contouring system provides an opportunity to adopt radiotherapy on the treatment day. In this thesis, freely deformable models (FDM) and shape constrained deformable models (SCDMs) were used to automatically delineate the GTV for brain cancer and prostate cancer.

Level set method (LSM) is a typical FDM which was used to contour glioma on brain MRI. A series of low level image segmentation methodologies are cascaded to form a case-wise fully automatic initialisation pipeline for the level set function. Dice similarity coefficients (DSCs) were used to evaluate the contours. Results shown a good agreement between clinical contours and LSM contours, in 93% of cases the DSCs was found to be between 60% and 80%.

The second significant contribution is a novel development to the active shape model (ASM), a profile feature was selected from pre-computed texture features by minimising the Mahalanobis distance (MD) to obtain the most distinct feature for each landmark, instead of conventional image intensity. A new group-wise registration scheme was applied to solve the correspondence definition within the training data. This ASM model was used to delineated prostate GTV on CT. DSCs for this case was found between 0.75 and 0.91 with the mean DSC 0.81.

The last contribution is a fully automatic active appearance model (AAM) which captures image appearance near the GTV boundary. The image appearance of inner GTV was discarded to spare the potential disruption caused by brachytherapy seeds or gold markers. This model outperforms conventional AAM at the prostate base and apex region by involving surround organs. The overall mean DSC for this case is 0.85.

Lay Summary

Cancer, more commonly described in terms of a tumour, is an abnormal cell growth with the potential to spread to other parts of the body. Medical scans such as computed tomography (CT) and magnetic resonance imaging (MRI) are widely used in the diagnosis and treatment of cancers. Radiotherapy, which is commonly used to treat cancer, uses a beam of high energy rays to kill the tumour cells. However, the beams used in radiotherapy can also damage healthy cells therefore it is very important that the tumour region is accurately defined to prevent the side effects which could be caused by the treatment. Based on the CT and MRI scan a doctor and a team of medical physicists will produce a radiotherapy treatment plan indicating where should be radiated and where should be spared. Because of the limited image resolution and other disadvantages of the current medical imaging techniques, it is not easy for doctors to produce the treatment plan. It usually takes a long time (up to two weeks) to prepare a treatment plan which may be used throughout the course of a 5 to 6 week course of radiotherapy. The aim of the thesis was to build a computer software system which can automatically identify tumours on medical images using a series of image processing approaches. The software system developed was able to process medical images (MRI and CT) and assist in radiotherapy planning in a very short time (10 to 50 minutes per patient).

Acknowledgements

First of all, I would like to express immeasurable appreciation and deepest gratitude to my supervisor Dr William Nailon for his consistent steering of my research work and daily life here in Edinburgh. His thoughtful advice and patient proof readings helped me enormously to form the publications and the integrity of this thesis. He has been both friend and mentor. I could not have imagined having a better supervisor for my PhD study. I also would like thank Prof Stephen McLaughlin from Heriot Watt University for the insightful advices. Special thank goes to Dr Duncan McLaren and Dr Sara Erridge who serves as our consultant oncologists and provided me training data and clinical reviews of my experimental results.

I should thank the College of Medicine and Veterinary Medicine, the University of Edinburgh and the Department of Oncology Physics, Western General Hospital Edinburgh for giving me the opportunity of this PhD program. I want to thank the labmates Mr Yang Feng, Mr Dean Montgomery, Miss Roushanak Rahmat and the former labmates Dr Hanqing Liao, Miss Yuan Tian and Dr Robin Steel, with whom I had good time and hard time, but never bad time.

On a more personal level, I would like to thank my family, in particular my parents Mr Shuhui Cheng and Mrs Zhihui Wang, for their consistent supports and encouragements from 7529 miles away. I also want to thank my girlfriend Miss Mengmeng Ren for her sweet love and company here in Edinburgh. The proposal will be right after the graduation and please say YES.

Last but not least, I want to thank the folks I met within the four years in Edinburgh, Dr Liang Song, Mr Chang Zong, Mr Qixiang Zhong, Mr Yi Zhang, Mr Yuan Liu, Mr Mantou (male labrador), the legendary A2 team and the basketball fellows. Thank you all for making my life in Edinburgh so joyful.

Declaration

I declare that this thesis was composed by myself, that the work contained herein is my own except where explicitly stated otherwise in the text, and that this work has not been submitted for any other degree or professional qualification except as specified.

Kun Cheng

Contents

Figures and Tables

Figures

Tables

Nomenclature

Abbreviations

2D	Two-dimensional
3D	Three-dimensional
3DCRT	Three dimensional conformal radiotherapy
4DRT	Four-dimensional radiation therapy
AAM	Active appearance model
ASM	Active shape model
CBCT	Cone beam computed tomography
CGRRT	Computer-guided real-time radiotherapy
CNS	Central nervous system
CPD	Coherent point drift
CT	Computed tomography
CTV	Clinical target volume
DNA	Deoxyribonucleic
DRR	Digitally reconstruction radiography
DSC	Dice coefficient
ECC	Edinburgh cancer centre
EM	Expectation maximization
FDM	Freely deformable models
FFD	Free form deformation
GMM	Gaussian mixture model
GTV	Gross tumour volume
GVF	Gradient vector flow
HD	Hausdorff distance
ICP	Iterative closest points

ICRU	International commission on radiation units and measurement
IGRT	Image guided radiotherapy
IMRT	Intensity modulated radiotherapy
ITV	Internal target volume
LDR	Low dose rate
LFW	Labelled faces in the wild
LINAC	Linear accelerator
LSF	Level set function
LSM	Level set methods
MaD	Mallow distance
MD	Mahalanobis distance
MDL	Minimum description length
MRI	Magnetic resonance imaging
NBAAM	Narrow band active appearance model
OAR	Organs at risks
OBI	On board imaging
PCA	Principal component analysis
PDE	Partial differential equation
PDM	Points distributed model
PET	Positron emission tomography
PSA	Prostate specific antigen
PTV	Planning target volume
RIQF	Regional intensity quantile functions
ROI	Region of interest
RPM	Robust point matching
SBRT	Stereotactic body radiotherapy
SCDM	Shape constrained deformable model
SDF	Signed distance function
SNR	Signal to noise ratio

SPH	Spherical harmonic representation
SRT	Stereotactic radiotherapy
SSM	Statistical shape model
SVD	Singular value decomposition
TPS-RPM	Thin plate spline robust point matching
TRUS	Trans-rectal ultrasound
TUR	Trans-urethral resection

Symbols

δ	Dirac function
Γ	Transformation of image registration
μ_k	Central moments
$\mu_{water}, \mu_{tissue}$	X-ray attenuation coefficient
ψ	B-spline control points
Σ	Covariance matrix
${}^{60}c_o$	Cobalt 60
B	B-spline basis function
b	Shape parameters/eigenvalue of active shape model
C	Two dimensional contour
c	Shape and appearance parameters of active appearance model
D	Diffusion tensor
E	Energy functional of a deformable model
G	Gaussian function
g	Appearance/Profile vector
G_σ	Gaussian function with standard deviation
H	Heaviside function
HU	Hounsfield unit
$I(x,y)$	Two dimensional image as a function of spatial index x and y
$i(x,y)$	Image intensity of a two dimensional image
$I(x,y,z)$	Three dimensional image as a function of spatial index x, y and z

$i(x,y,z)$	Image intensity of three dimensional image
J	Structure tensor
k	Appearance model parameter update step size
L	Landmark-wise feature selection vector
m	Mean
N	Number
p	Probability
$P(x,y)$	Two dimensional point set
$P(x,y,z)$	Three dimensional point set
P_g	Eigenvectors of the appearance deformation
P_s	Eigenvectors of the shape deformation
R	Appearance model parameter update matrix
r	Appearance residual
S	Three dimensional surface
s	Scale parameter
U	Model parameters of active appearance model
V	Image volume
T	Transformation of point set registration

Chapter 1

Introduction

1.1 Cancer

It is estimated that the total number of cells in the human body is 3.72^{13} [2]. Each of these cells performs a specific job to maintain the function of organs. Cells proliferate to replace worn-out cells by cell division and every doubling process consumes small segments of deoxyribonucleic acid (DNA). This is known as a telomere and can be thought of as the code of cell division. After many cell divisions, the cells are no longer able to divide again. This is when they reach the Hayflick limit [3], which is on average 52 times. The Hayflick limit does not apply to certain types of cells, for example cancer cells which are infinitely replicative. Without the control of the Hayflick limit the division of cancer cells is allowed to proceed indefinitely, forming a malignant growth commonly known as a tumour.

The causes of cancer varies and includes but is not limited to, genetic make up, environmental conditions, lifestyle factors, virus and bacterial infection. There are over 100 types of cancers which are classified depending on the different organs or body structures within which the cancer cells develop. The most common cancers are found in the prostate, breast, brain, and lung. In 2010 in the UK, 49,564 women were diagnosed with breast cancer - approximately 157 cases per 100,000 women; 23,175 men diagnosed with lung cancer - approximately 76 cases per 100,000 men; 2,286 men diagnosed with testicular cancer - approximately 7 cases per 100,000 men [4]. It is interesting to study cancer statistics among sex, country and ages, because this could shed light on the causes of different cancers. Breast cancer is the most common in women, with 31 out of every 100 cancers diagnosed in women. But in women aged 15-24, melanoma and Hodgkin lymphoma are the most common (16% each), with less than

1% women diagnosed with breast cancer in this age group [4]. The lowest incidence of breast cancer is in Japan accounting for 16.7% of all cases of cancer, which is much lower than in the USA where it accounts for 30.4% of all cancers. The incidence of breast cancer in Japanese women living years in the USA is however the same as for the general population of American women [5]. Genitourinary cancers affect the human pelvic region including the urinary tract, bladder, kidneys, prostate, testicles and penis. Prostate cancer has emerged as a common cancer among men within the UK and Europe, with 25 out of every 100 male cancers. For men from aged 25-49, testicular cancer is the most common (15%), while prostate cancer only accounts for 4% of male cancers in this age group. There were 41,736 new cases of prostate cancer in males in the UK in 2011, and 10,793 deaths from prostate cancer in the same year. Within Europe, the highest prostate cancer mortality rates are in the Baltic region (Estonia, Latvia and Lithuania) and in Denmark, Norway and Sweden [6].

The aim of cancer treatment is to remove or kill the cancer cells while sparing healthy cells. This can be challenging because if any cancer cells survive the treatment they have the potential to reproduce into a new tumour. This includes cancer cells left at the site of original tumour after treatment and cancer cells that have spread to other sites of the body. The tumour recurrence rate in brain cancer was reported based on 36 patients treated by Stereotactic Radiotherapy (SRT), 47% (17/36) recurred over all, 35% (6/17) recurred at the original tumour site, (6/17) recurred at distant sites within the brain, and 18% (3/17) recurred at both the original and distant brain sites [7]. Another study reported a median term (45 months) probability of prostate cancer recurrence after radical prostatectomy, 50% (125/250) patients experienced disease progression, within which 49 (10%) patients developed distant metastases and 20 (4%) recurred at the original prostate region [8]. Brain and prostate cancers are the main anatomical sites of interest in this radiotherapy thesis, where the goal is to improve treatment outcome with the help of medical image analysis techniques.

The main techniques used to treat cancer are listed below:

Surgery is a common option in which cancer cells are removed by cutting away the tumour and some tissues. Surgery is often followed by radiotherapy or chemotherapy to ensure that any remaining cancerous tissue is treated.

Chemotherapy uses cytotoxic drugs to kill cancer cells. These are given as a tablet, injection, infusion, or directly into a vein.

Radiotherapy, also known as radiation treatment, can be applied internally or externally. External beam radiotherapy uses focused X-rays generated from an external source outside the body to kill cancer cells. Internal radiotherapy, or brachytherapy, uses a radioactive source placed close to the tumour inside the body.

1.2 Radiotherapy

Radiotherapy is the most widely used treatment for cancer, with 4 out of 10 cancer patients receiving radiotherapy as part of their treatment. Radiotherapy uses high-energy radiation to kill cancer cells by damaging their DNA. Plots of the probability of tumour control and normal tissue morbidity are shown in Figure 1.1. In Figure 1.1(a), the two curves are widely separated and the ideal treatment dose D_o is shown to kill most of the diseased cells while the damage to healthy cells is kept to an acceptable level. However, in practice shown in Figure 1.1(b), it is difficult to identify D_o and as a result a compromise must be made regarding the amount of dose delivered to the tumour and the normal tissue that will be affected. Throughout this

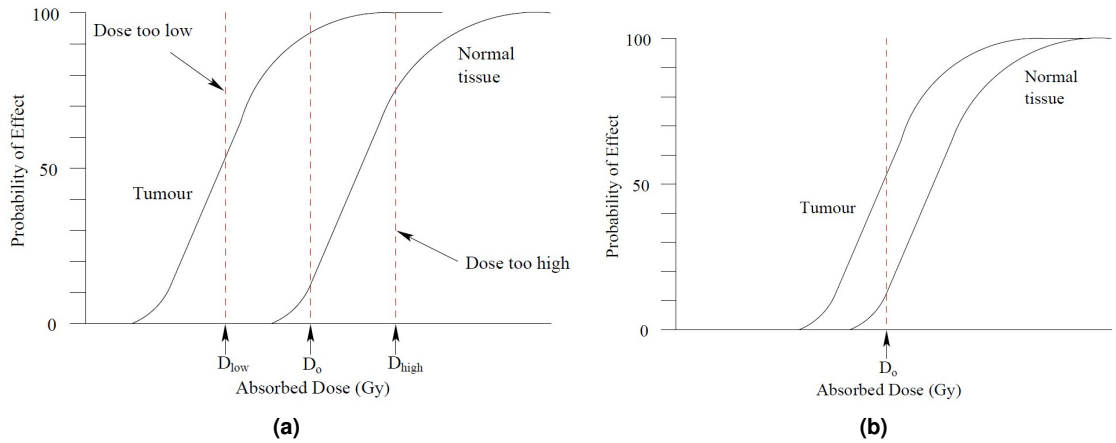

Figure 1.1: Probability of tumour control and normal tissue morbidity plotted against dose for (a) the ideal case and (b) the practical situation. D_o is the treatment dose and response is a measure of the cells killed.

thesis, radiotherapy specifically refers to external beam radiotherapy. A full radiotherapy cy-

cle comprises imaging, treatment planning, simulation/verification and radiation delivery. In treatment planning clinicians provide detailed instructions in the form of contours defining the gross tumour volume (GTV) and organs at risk (OAR); where should be irradiated; where should be avoided; and the dose of radiation that should be given to the GTV and OAR based on a patient's radiotherapy planning image. Simulation treatment ensures that the plan can be delivered and the verification process verifies that the treatment doses can be delivered as planned. In the final treatment delivery phase the pre-defined amount of radiation is divided into fractions and the patient receives a fraction on a daily or weekly basis. Planning is an important step in the radiotherapy process, and has a significant impact on the treatment outcome. Within all the three steps of the radiotherapy process, the treatment planning process is perhaps the most important and calls for the joint efforts of radiation oncologists, radiation therapists, medical physicists and medical dosimetrists. The delineation of the GTV is usually the very first step in the planning process, other target volume definition and dose calculation are based on the GTV definition. Consequently, even a small bias created from GTV contouring has the potential to degrade the final treatment plan and the performance of the whole treatment. The following section explains the role of GTV contouring in target volume definitions in the radiotherapy planning.

1.2.1 Tumour Volumes in Radiotherapy Planning

The International Commission on Radiation Units and Measurement (ICRU) issued a series of reports to define appropriate volumes which are useful for radiotherapy planning [9, 10, 11] (Figure 1.2). In ICRU report 62, the GTV is defined as the malignant growth of the tumour. The clinical target volume (CTV) is a sub-clinical region including the GTV and margin around the GTV where there may be microscopic involvement. The planning target volume PTV is described by specifying the margins that must be added around the CTV or GTV to compensate for external treatment inaccuracies as the effects of organ, tumour and patient movements, inaccuracies in beam and patient setup, and any other uncertainties. Consequently, the bias of a sub-optimal GTV contour will be enlarged multiple times from the corresponding planning target volume (PTV), and unnecessarily increases the volume of healthy tissue radiated.

Steenbakker et.al showed that in radiotherapy for lung cancer, within all the geometric uncertainties the inter-observer variability of contouring the target volume are much larger than the setup variation and organ motion [12]. It is also reported that high inter- and intra- clinical variability exists in many other medical image interpretation cases for example cervical esophageal cancer, brain cancer, prostate cancer and bladder cancer [13, 14, 15, 16]. Figure 1.3 shows a study of the inter-observer variability of contouring for prostate cancer planning. A large inter-observer variability is expected when the boundaries are not well presented on the image [17]. Contouring is challenging because often the images on which the clinician is defining the tumour volume and OARs, suffers from low image resolution and poor soft tissue contrast. As a result, the definition of the GTV or CTV on pelvic computed tomography (CT) images can be highly subjective and imprecise, which could lead to the error propagation in the radiotherapy planning process and compromise the final treatment outcome.

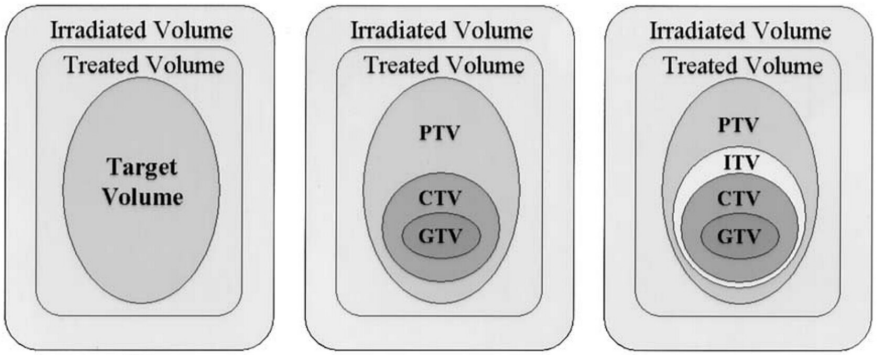

Figure 1.2: Left: Boundaries of the volumes defined by ICRU Report 29: target volume, treatment volume, and irradiated volume; Middle: boundaries of the volumes defined by ICRU Report 50, GTV, CTV, PTV, treated volume, and irradiated volume; Right: boundaries of the volumes defined by ICRU Report 62: GTV, CTV, internal target volume (ITV), PTV, treated volume, and irradiated volume.

1.2.2 Image Analysis in Radiotherapy

Medical image analysis techniques have the potential to assist clinicians in radiotherapy planning in many ways.

Image Enhancement: Reduction of observer variability can be achieved by applying image enhancement to the planning CT [12], or registering multiple imaging modalities [18].

Reproducibility: By identifying the GTV boundary using image statistics and mathematical

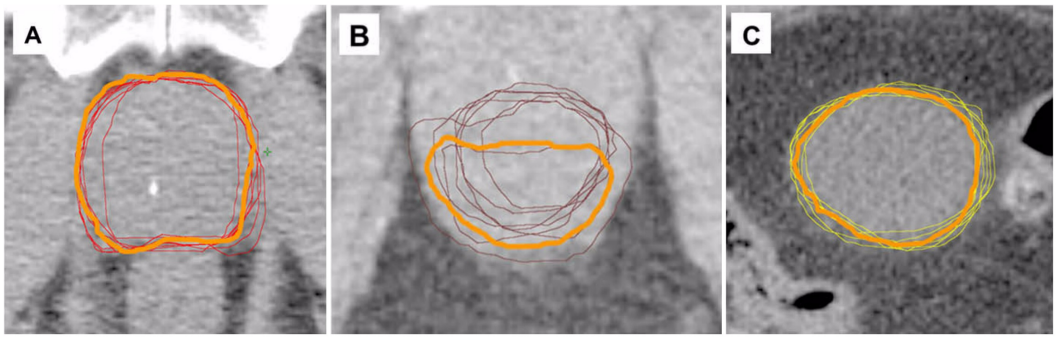

Figure 1.3: Illustration of the inter-observer variability in delineation for prostate cancer planning, bladder and rectum are contoured as OARs. Illustration of the computer segmented (thicker line) and 7 radiation oncologists' contours (thin lines): (A) prostate GTV, (B) rectum as an OAR, (C) bladder as an OAR [17].

algorithms, it is possible to generated contours which are inherently reproducible. This completely removes inter- and intra- variation in contouring.

Time Saving: Standard radiotherapy requires a significant amount of clinician time to outline the target volumes and plan a treatment. With the assistance of powerful computers and computerised contouring algorithms, image contouring time could be efficiently reduced.

Adaptability: Contours defined by a clinician during the planning phase are often used throughout five or six weeks of treatment delivery. However, during this time the tumour may change in size and shape, although the ability to change or adapt GTV outlines remains a challenging task.

1.3 Medical Image Analysis

Medical image analysis is one of the most popular research areas having expanded from the simple visualization of human internal structure to inspection and analysis of anatomic organ structures. It has now become a popular tool for surgical planning, intra-operative navigation, radiotherapy planning, and for tracking the progress of disease. The advances of medical imaging technology, especially the increasing of resolution and contrast, offers new opportunities for improving radiotherapy treatment. A variety of medical image analysis methods have been developed, and more accurate and reliable solutions have been produced for sophisticated medical problems. This has been helped by the development of computing power, with ever

increasing the computational requirement of algorithms.

1.3.1 Medical Image Segmentation

A very important branch of the medical image analysis is medical image segmentation, particularly auto-segmentation/delineation. Image segmentation refers to the partitioning of an image/volume into multiple segments, or extracting the contour/surface of interest from the image/volume background. Medical image segmentation, also known as contouring, is usually performed by a doctor or an oncologist, because it is highly specialised and requires a considerable amount of clinical experience and anatomical knowledge. Through years of research, automatic segmentation algorithms have achieved success in many medical delineation tasks. However, significant challenges still remain, particularly in brain, head and neck, and pelvic regions where there are many complicated structures, of which the automatic segmentation of the GTV and surrounding OAR is the focus of this thesis.

1.3.2 Deformable Models

Shape and appearance are two of the most important and useful properties in a medical image analysis. Segmentation methods can partition ROIs using image appearance information, ROI shape prior information, or a combination of these. Methods segmenting ROIs using image appearance information can be further classified into region based methods and edge based methods. Widely used edge based methods include edge detection operators and gradient flow based level set methods [19, 20]. Active contour, clustering, and texture classification are categorised as region based methods [21, 22, 23]. Shape prior information can also be used to segment objects, for example the Hough transform is widely used for detecting simple shapes, such as straight lines, circles or ellipses [24]. Another important category of segmentation methods combining the appearance information and shape prior are deformable models. Deformable models find the balance between shape change and local appearance difference by moving the points on a contour/surface. Segmentation methodologies by deformation can be generally divided into two kinds: freely deformable models (FDM), including active contours and level set methods [21, 25], whose deformation has no constraint and proceeds until an edge

of contour is reached; and shape constrained deformable model (SCDM) whose deformation is constrained by a pre-learnt shape variation, and periodically refines the deformable model to maintain a reasonable shape. The widely investigated SCDMs refers mainly to the active shape model (ASM) and active appearance model (AAM) and their extensions [26, 27]. The SCDMs require a training archive and have the advantage that the target volume has a more stable shape and predictable variation than the FDMs. The FDMs are capable of segmenting target volumes with large variations, these methods require careful initialisation to avoid propagation across weak or missing boundaries. In practice, successful segmentation of a medical image requires a pipeline consisting of a combination of these methods. The segmentation techniques described above gather information about shape, appearance or both of them from the segmentation target to build a mathematical model, which can be used to segment ROIs on new images.

1.4 Objectives of the Research

The aim of this work was to improve radiotherapy by employing medical image analysis techniques. The main objectives were to:

1. **An automatic contouring system for brain cancer radiotherapy planning**

   At present, manual delineation of the GTV and OARs is still the most widely used method for creating radiotherapy plans. This requires a significant amount of clinical experience and is time consuming. It is further complicated by the fact that the volume size and shape of the GTV may appear different, sometimes quite significantly, depending on the imaging modality used to visualise the tumour [10, 11]. Often, the boundary between cancerous regions and healthy tissue is too difficult to be defined accurately. Clinicians contour the GTV using anatomical knowledge, in addition to their experience, resulting in significant variability being reported in the manual segmentation in brain cancer [28]. An automatic contouring system would be beneficial in radiotherapy planning in order to generate objective, accurate and reproducible GTV contours. The first research objective of this thesis was to build an automatic contouring system for brain cancer based on an analysis of magnetic resonance imaging (MRI) scans.

2. **An automatic contouring system for prostate cancer radiotherapy planning and treatment plan update on CT and MRI**

   There has been significant development in treatment delivery over the past two decades with intensity modulated radiotherapy (IMRT) delivery using multiple beams with a highly non-uniform dose across the field. This results in a sparing of normal tissue. Image guidance is essential in the use of IMRT because the customised non-uniform dose distribution carries a risk of overdosing the normal tissue. Image guided radiotherapy (IGRT) has helped with this, where it is now possible to acquire cone beam computed tomography (CBCT) images before, during and after treatment delivery to allow positional correction. Real-time contour/shape matching or registration methods allow corrections to be applied between treatment fractions, leading to an adaptive radiotherapy planning framework. Consequently, there is now the potential to improve patient treatment by adapting sub-optimal radiotherapy plans based on the on board imaging (OBI), using deformable models. The second research objective was to develop two automatic contouring systems for prostate GTV on CT and MRI respectively.

3. **A new framework for radiotherapy treatment using multi-modality image information based on automatic contouring systems**

   Automatic contouring systems can be employed both in original treatment planning and in updating the treatment plan based on the IGRT information. There is potential to improve the current radiotherapy protocol by implementing computerised contouring, IGRT and IMRT, towards a new radiotherapy framework. The new framework takes advantage of the joint efforts of the contouring systems, designed for inter-patient and intra-patient contouring, and the patient-specific clinical information. Using deformable model applications, the new framework is compatible with CT, MRI, CBCT and other medical imaging modalities. This framework has the potential to produce an optimised contouring solution and make full use of IMRT and IGRT, leading to an improved treatment outcome.

1.5 Contributions

In realisation of the objectives major contributions of this thesis are:

1. **Automatic GTV contouring of higher grade glioma on brain MRI (Chapter 4)**

   Gliomas are the most common primary brain tumours, Grade IV gliomas, also known as glioblastoma multiforme, are the most rapidly growing where the treatment is made difficult by the spread within the brain. The field of active contour, also known as a 'snake', is based on the framework of level set methods (LSM) which have shown potential in segmenting gliomas on MRI scans of brain cancer patients. Here a series of low level image segmentation methodologies were cascaded to form a case-wise fully automatic initialisation pipeline for the level set segmentation of gliomas.

2. **A new group-wise shape registration scheme (Chapter 5)**

   Obtaining dense correspondence across a group of shapes of deformable objects is the first step of construction of an SCDM. Errors in establishing such correspondences can lead to large shape variability and meaningless shape models [29]. It is common practice to perform a pairwise registration of each subject in the group to a reference, or the group mean. However these approaches lead to difficulties in medical cases, due to the pronounced anatomic variability between individuals [30]. A new group-wise registrations scheme is introduced to register multiple subjects, using a combination of the iterative closest points (ICP) and the coherent point drift (CPD) method. By registering all subjects in the training set to a unit sphere the group-wise correspondence is indirectly and accurately defined.

3. **An ASM of prostate GTV driven by optimised texture features (Chapter 5)**

   In genitourinary cancer the treatment of high risk prostate cancer commonly includes the prostate gland and the seminal vesicles. There is good statistical shape coherence among a large patient population for this disease [31]. Given a sufficiently large training archive SCDMs have the potential to capture the shape variation of prostate GTV including the cancerous invasion adjacent to prostate gland. The conventional ASM methods [26] drives the landmarks displacement using local image gray level patterns, which may not be capable of distinguishing GTV exterior and interior on planning CT. Here a

set of 3D texture features including intensity, derivative, mean, variance, coarseness, skew, kurtosis, energy and entropy was pre-calculated. Based on the defined points correspondence, a texture optimisation procedure finds a specific image feature for each landmark on a GTV surface, which most efficiently distinguishes the GTV interior and exterior. The segmentation is driven by the optimised texture features which intuitively contains more information than the statistics of individual pixels.

4. **An automatic initialisation & pre-segmentation algorithm for the AAM proposed (Chapter 6)**

   The initialisation of conventional AAM is achieved by building a multi-resolution model of object appearance [27], in which the segmentation starts at a coarse resolution and iterates to convergence at each resolution level before projecting the current initialisation to the next level of the model. This scheme produces a reliable initialisation while increasing the computational cost both in the training and segmentation process significantly. Here a novel initialisation scheme is proposed, which take into account regional image quantile and the AAM appearance variation. The initialisation is applied in a coarse-to-fine manner, by minimising the regional image quantile difference an estimated location of the GTV is obtained, which will be refined using the AAM appearance variation. The GTV scale variation is also fitted in the initialisation to increase the capture range of the AAM.

5. **A narrow band AAM of prostate GTV (Chapter 6)**

   The unparalleled soft tissue contrast on MRI provides more clinical information by image appearance, which is the key to building an AAM. Prostate cancer is considered to be a multi-focal disease, therefore the conventional AAM modelling scheme is not suited to analysing prostate GTV appearance. Vincent et al. [32] showed that the conventional AAM method has poor results at the apex and the base of the prostate and can be improved by involving surrounding structure such as the bladder. A novel narrow band AAM algorithm is proposed to remedy this issue, which accounts for the interior appearance near the GTV boundary and the exterior appearance, including part of neighbouring organs. This is achieved by expanding the GTV surface 1 cm

perpendicular to the surface, interiorly and exteriorly. The resulted appearance void in the middle also spares the potential disruption caused by brachytherapy seeds or gold markers.

1.6 Outline of Thesis

The outline of the thesis is as follows:

In Chapter 2 a detailed background of cancer radiotherapy is presented. This includes imaging modalities in Section 2.2, anatomical information in Section 2.3, cancer treatment in Section 2.4, and external beam radiotherapy in Section 2.5.

Chapter 3 provides a systematic review of medical image processing and analysis methodologies relevant to this thesis. In Section 3.2, thresholding, edge indicators, and morphological operations are introduced as low level segmentation methods. Section 3.3 covers the major existing image registration methodologies, which include rigid and non rigid registrations. In Section 3.4, texture analysis is covered, including first order statistics, higher level statistics, and gray level co-occurrence matrix. Unconstrained deformation models are reviewed including, active contour and level set methods. In the last section conventional ASM and AAM are presented as the constrained deformation models.

In Chapter 4 a level set method for automatic delineation of brain cancer GTV on MRI is introduced. The data set is defined in Section 4.2 and Section 4.3 covers the work flow of the proposed algorithm followed by the results and discussion in Section 4.4.

Chapter 5 introduces the extended narrow band AAM method modelling only the GTV boundary regions. Data definition includes the construction of 3D image volumes from MRI stacks in Section 5.2. The proposed algorithm is described in Section 5.3 and the results and discussion in chapter 5.4.

Chapter 6 demonstrates an algorithm based on an extended ASM method using selected texture features instead of image grey levels. This algorithm automatically segments the prostate GTV on CT images, the pipeline of which is detailed in Section 6.3. Further discussion and result analysis is covered in section 5.4.

Chapter 7 concludes this thesis with a summary, conclusion and discussions on the future

direction of this work.

Chapter 2

Background

2.1 Introduction

Radiotherapy quickly followed the identification of X-rays in 1895 by Roentgen [33]. It was soon recognized that radiation produced dramatic effects on normal tissues and within a few years it was being used to irradiate tumours. The ICRU was founded in 1925 to standardise the quantity and accuracy of the radiation delivered. This was long before the major advances in radiotherapy that have taken place since the 1940s and the discovery of new radionuclides $^{60}c_o$ (Cobalt 60) and the invention of the linear accelerator (LINAC). Radiation protection is an important concern in radiotherapy because when radiation sensitive organs such as the stomach, rectum, prostate and prostate nodes receive radiation the effect could be fatal. A major LINAC development was the ability to perform IMRT and IGRT, which can deliver more focused radiation to the the PTV. By using a combination of several intensity modulated beams from different directions, IMRT minimises the damage to surrounding radiation sensitive tissues particularly OARs. Before the invention of IGRT, a larger than necessary PTV would have been used to compensate for localisation errors. IGRT is possible because of the invention of OBI which allows the imaging of the treatment field just before, during or after the delivery of radiotherapy. In theory this allows a radiotherapy plan to be adjusted before each faction of treatment.

Radiotherapy is a sophisticated and complicated process, which requires a significant collaboration between oncologists, physicists, radiographers and engineers, all of whom have knowledge and experience in their respective fields in order to deliver the optimal treatment. In this chapter essential background information on the imaging modalities, anatomy of the organs investigated, with special emphasis on external beam radiotherapy procedures, is presented.

2.2 Medical Imaging

Medical imaging systems create visual representations of the interior of the human body for clinical analysis and medical intervention. They can provide immediate and accurate digital information about a patient's condition in the form of digital images, which can be efficiently analysed, stored, replicated and communicated. Many different medical image modalities are used in the treatment of cancer. CT, MRI, CBCT and Positron Emission Tomography (PET) are the most commonly used modalities in radiotherapy. CT and MRI are discussed here in more detail because they are the main image modality used in this thesis (refers to [34, 35] for more information about PET and CBCT).

2.2.1 Computed Tomography

CT is the most widely used imaging modality throughout cancer treatment. The first CT scanner was developed in 1972 by Godfrey Hounsfield, which consisted of an X-ray tube that rotated around a patient with an opposing detector to receive the X-ray beam. CT scanners have been through 4 major evolutions since this time resulting in an increase in detectors, decrease in the scan time and the geometry of the scanner. The four generations of CT scanner are shown in Figure 2.1 [36].

A CT machine produces gray levels (CT numbers) image where the values are measured in Hounsfield units (HU), which corresponds to the X-ray attenuation after going through the irradiated materials defined by [37],

$$H = \frac{\mu_{tissue} - \mu_{water}}{\mu_{water}} \times 1000 \tag{2.1}$$

where the μ_{water} and μ_{tissue} refer to the X-ray attenuation coefficients of water and the scanned object. Hence CT inherently provides the electron density information which is necessary for estimating dose in radiotherapy. The geometric consistency of CT images is preserved from both the data acquisition and the image reconstruction. CT has less spatial distortion than any other medical image modality, such as MRI which suffers from significant spatial distortion. It is important to maintain an accurate relationship between HU and the electron density in order

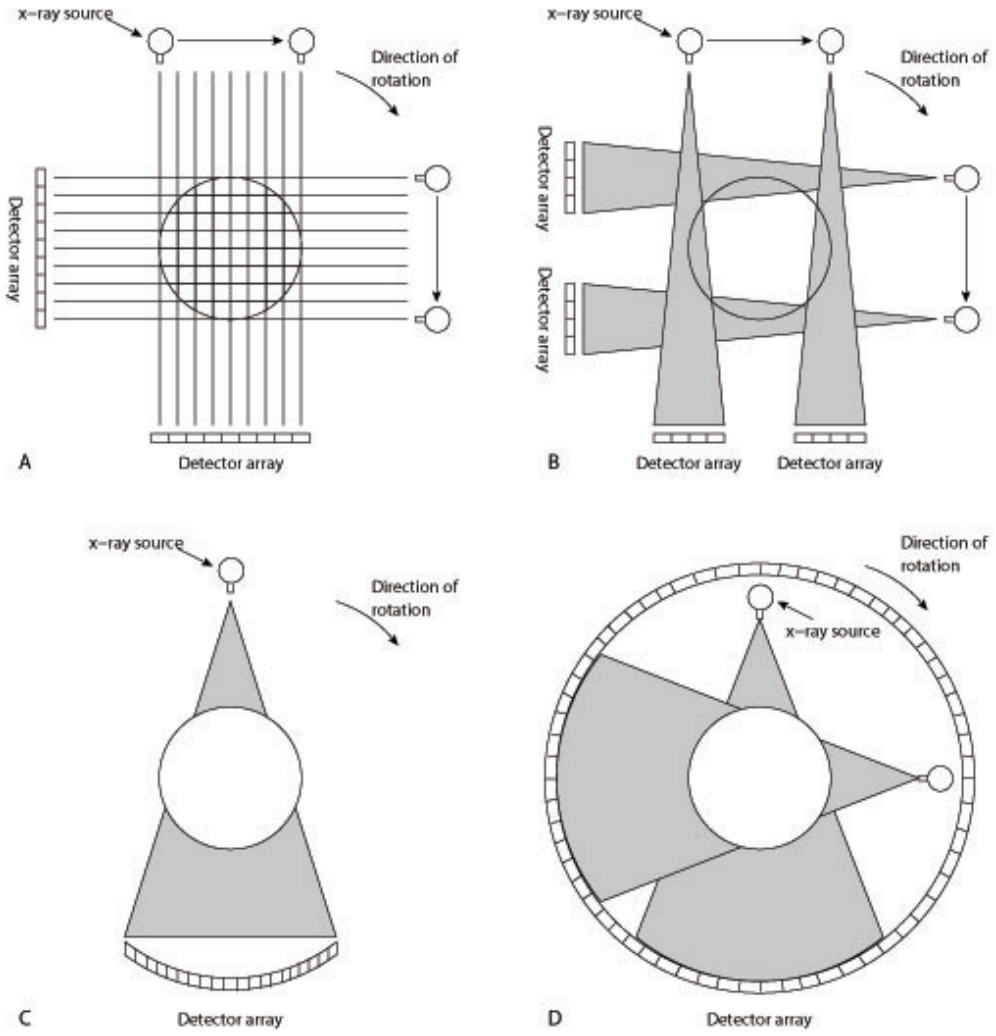

Figure 2.1: (A) First-generation CT scanner in which a pencil beam X-ray and detecting element is translated and rotated around a stationary patient. (B) Second-generation CT scanner that uses a fan beam X-ray and an array of detector elements. The X-ray source and detectors translate and rotate as before. (C) Third-generation CT scanner which has a rotating X-ray source and rotating array of detectors. (D) Fourth-generation CT scanner has a stationary array of detectors and a rotating X-ray source [36].

to guarantee a precise treatment. This is achieved by scanning a calibration phantom containing multiple inhomogeneities, which usually are air, water, soft bone, cortical bone and lung tissue as shown in Figure 2.2. The mean and variance of the CT numbers within each material should fall in a tight interval defined by international guidelines. Consequently the volume constructed from CT images is accurate and reliable. The most significant disadvantage of CT imaging is the poor soft tissue contrast.

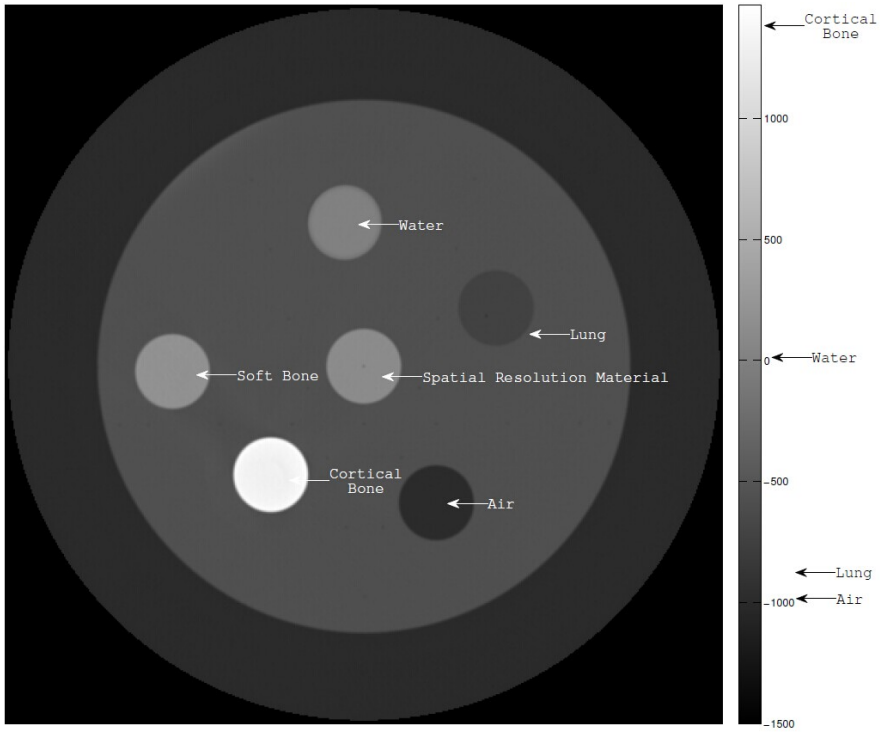

Figure 2.2: Six inhomogeneities calibration containing air, water, soft bone, cortical bone, lung and a spatial resolution object. The mean CT numbers of each material is indicated by arrows, while the variance is controlled within a tight interval.

2.2.2 Magnetic Resonance Imaging

MRI is another popular medical imaging modality, making use of the magnetic properties of certain atomic nuclei. Hydrogen nuclei are present in water and therefore all over the human body. In acquiring an MRI a strong uniform magnetic field is firstly generated by the scanner to align the nuclei. The hydrogen nuclei can be rotated using radio waves, and subsequently oscillate in the magnetic field and simultaneously emit a radio signal, as shown in Figure 2.3. Radio signals are received by a coil and can be used to make detailed images of the scanned tissue. The molecular environment of healthy and pathological tissues influence the behaviour of regional nuclei, which in turn influences the characteristics of the received MRI signal, giving an unparalleled soft tissue contrast on MRI images [38]. Relaxation time influences the emitted MRI signals, image contrast of MRI images may be weighted by T1 (spin-lattice) relaxation time and T2 (spin-spin) relaxation time to highlight anatomical structures or pathology of interest. T1 weighted MRI tends to display better contrast on anatomical structures,

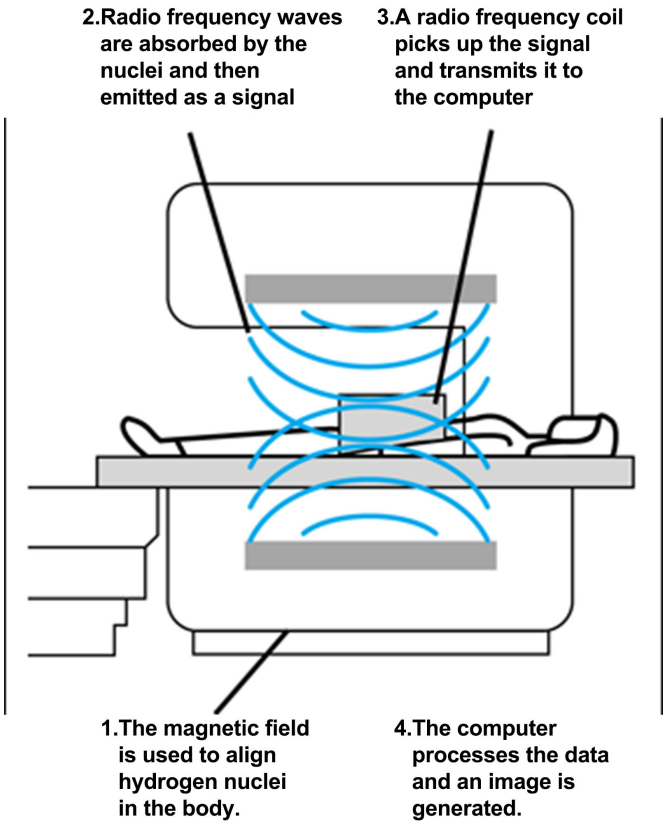

Figure 2.3: The major parts of an MRI scanner [39].

while T2 weighted MRI is more useful for pathological investigation and widely used for diagnosis. Figure 2.4 shows a series of rigidly registered images acquired on a patient treated for prostate cancer highlighting the difficulty in interpreting critical structures in different imaging modalities. These images were re-sampled into the same resolution and geometry, resulting in a slice-by-slice correspondence. It can be observed that T1- and T2-weighted MR images (top left and right) provide unparalleled resolution and contrast for pelvic structures and a more detailed information within the prostate gland on T2 weighted MRI (top right). Soft tissue matching is difficult because of the atrophy induced in the prostate by the neo-adjuvant hormones administered between MR and CT acquisition. The hyper-intense gold markers implanted within the prostate gland and used for positional verification are clearly visible on CT and CBCT images (bottom left and right). Alignment is complete and treatment begins when the hyper-intense markers are aligned on CT and CBCT.

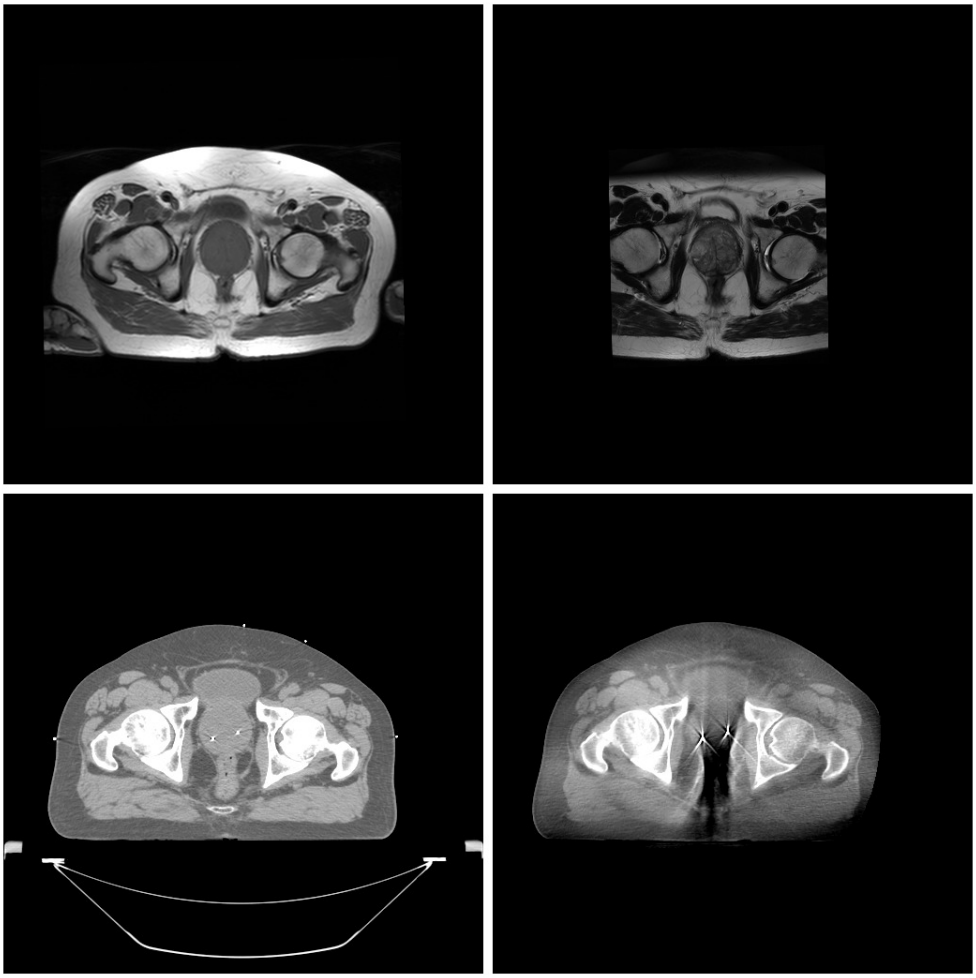

Figure 2.4: Top left and right: T1- and T2-weighted MR images acquired on a Siemens Symphony 1.5T scanner (Siemens, Munich, Germany). Bottom Left: Radiotherapy planning CT acquired on a Philips Brilliance Big Bore CT scanner fitted with a flat couch. Bottom right: Corresponding pre-treatment CBCT image acquired on a Varian system used for positional verification. Two gold markers are implanted for the use of spatial alignment, which are shown clearly on CT and CBCT scans.

2.2.3 Other Imaging Modalities

CBCT is a higher resolution, lower scan dose alternative to multi-slice helical CT [40, 41]. A cone shape X-ray is directed through the patient's region of interest and projected onto an area X-ray detectors. It requires only one rotation to gather information needed to construct an image [35], which makes CBCT an useful imaging tool for IGRT.

PET provides functional imaging information by using radioactive tracer in the organ or area of the body being examined and is usually registered with CT [34].

2.3 Anatomical Information

It is essential to know anatomy around the suspect tumour regions when creating a radiotherapy treatment plan, because an optimal radiotherapy plan usually contains definition of the GTV volume and nearby radiation sensitive OARs. Medical image processing approaches developed in this thesis were applied to brain and prostate cancer cases, therefore the anatomical properties of the human brain and pelvic region are presented in this section.

In prostate cancer, cancerous cells usually develop and form multiple small areas of malignant growth inside the prostate gland, called the 'focus', and quickly spread within the gland and invade the surrounding tissues in the genitourinary organs. As a result the GTV defined for prostate cancer usually contains the prostate gland and its immediately adjacent cancerous structures. OARs are often very close to the GTV in the pelvis. In prostate cancer treatment, the rectum and bladder are considered as OARs. The difficulties of prostate cancer planning is in treating the cancer and sparing the OARs.

The human central nervous system (CNS) is responsible for integrating sensory information and responding accordingly. It consists of the brain and spinal cord. The brain is the major part of CNS and performs as the processing unit of the CNS. Therefore in the case of brain cancer radiotherapy, it is important to maintain the nerve function when radiation is delivered to the invasive tumour volume.

The remainder of this section, deals with the human coordinates, following by more detailed radiotherapy-specific anatomy of the brain and pelvis respectively.

2.3.1 Human Coordinates

Human anatomy and anatomical atlases use axial, sagittal, and coronal planes to plot human anatomy. In a 3D coordinate system this consists of three axes, superior-inferior, anterior-posterior, left-right, forming three planes as shown in Figure 2.5. The coronal plane goes through human body from chest (anterior) to back (posterior), the sagittal plane from left hand to right hand, and axial plane expand from head (superior) to foot (inferior). Medical image scans are usually acquired axially in 2D from patient superior to inferior plane. These can be stacked into a 3D volume image for investigation in other planes. This is known as a digitally

reconstruction radiography (DRR).

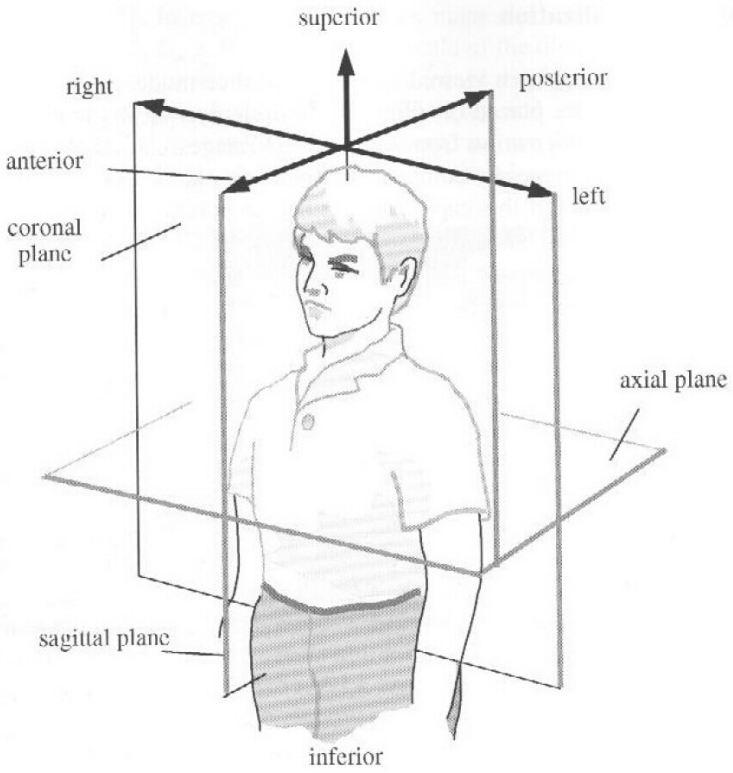

Figure 2.5: The coordinate system used for anatomical description (image from [42]). There are three pairs of directions: superior-inferior (head to feet), anterior-posterior (chest to back) and left-right. Three planes as indicated: axial, sagittal and coronal. The images can be stacked together to form a 3D image and the 3D image may then be re-sampled into arbitrary planes.

2.3.2 Anatomy of the Brain

The human brain is enclosed in the skull and protected by the cranium. As the major part of CNS it can be considered as the central processing unit for the human body. The brain analyses sensory information from other parts of the body and passes responses accordingly. There are 12 pairs of cranial nerves in the head and neck region which are labelled as shown in Figure 2.6a [43]. These cranial nerves are involved in sensation and control of the muscles. They are radiation sensitive and where possible should be excluded from the GTV definition. Damage to the cranial nerves is unrecoverable and may cause a loss of certain sensations and weakness in muscle control. It is therefore important to consider the immediate and long-term function of the CNS when making a radiotherapy plan for brain tumour patients. Figure 2.6b

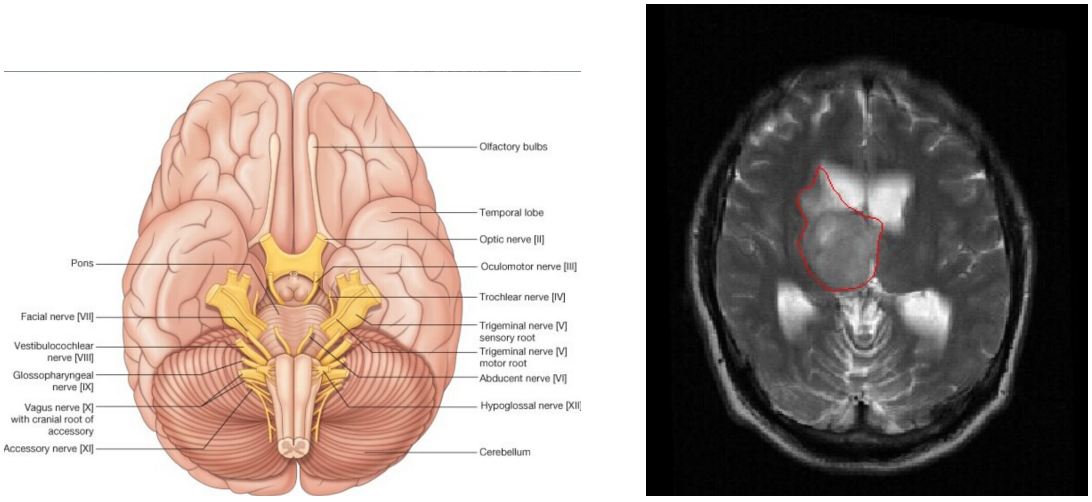

(a) (b)

Figure 2.6: (a) Labelled cranial nerves from [43], (b) A MRI scan shows the invasion of glioma into cranial nerves, red contour: GTV volume. Comparing (a) and (b), it is clear that the oncologist has left the optic nerve out of the GTV contour to ensure that the patient not lose sight after treatment.

shows an MRI scan of a patient with a grade IV glioma which is invading into the optic nerves where the red contour denotes the GTV volume defined by an oncologist. In this case the oncologist delineated the GTV and excluded healthy areas of the optic nerves to preserve nerve function after radiotherapy.

2.3.3 Anatomy of the Pelvis

The prostate is a walnut sized organ of the male reproductive system, which is located in the human pelvis. Figure2.7a, taken from [44], shows the prostate anatomy in the transverse (axial) and sagittal planes. The base of the prostate is attached to the inferior end of the bladder, where there is no fat plane between the two organs. The bladder is a distensible hollow organ used for storing urine. The amount of bladder filling changes its volume and shape and the shape of the adjacent prostate. The bladder as an OAR in radiotherapy also presents another difficulty in the contouring of the GTV. Due to the limited soft tissue contrast of CT, it is difficult to define the boundary between the bladder and prostate, as shown in Figure 2.7b. The rectum is the last section of the gastrointestinal tract, located at the posterior of the prostate. Similarly, the rectum has an unpredictable shape and appearance on CT and MRI, due to filling

and digestive movement. Rectal distension and movements can result in a significant anterior-posterior prostate gland displacement. Planning and delivery of radiotherapy needs to take into account these organ movements [45]. This may also result in a correlated shape change between the prostate and other OARs.

2.4 Treatment of Cancer

The standard procedure leading to the treatment of cancer includes: diagnosis, grading, staging, planning and treatment delivery. Medical imaging plays an essential role throughout this process. This section reviews the diagnosis, grading, staging and choice of treatment with respect to brain cancer and prostate cancer treatment at the Edinburgh Cancer Centre (ECC). Both grading and staging are based primarily on pathology, which provides essential clinical information for treatment choice and also can be applied as a prior in the whole treatment process. In this thesis, treatment delivery refers to the delivery of external beam radiotherapy and will be covered in detail in Section 2.5.

2.4.1 Cancer Diagnosis

Diagnosis is the very first step of cancer treatment. There are many tests that can be applied to a patient with suspected cancer. Usually, two or more tests are combined to confirm the presence of a certain type of cancer. The most commonly used method for diagnosis of brain and prostate cancer are briefly discussed in the following sections.

Brain Cancer Diagnosis

A **Physical Examination** including a test of the nervous system will firstly be carried out on the patient when a tumour is considered as a secondary brain tumour, which has spread from somewhere else in the body. This is followed by a **Blood test** in which the level of specific chemical markers in the blood signify certain type of tumours, such as pineal region tumours or germ cell tumours that change the level of particular hormones. **Image based diagnosis** includes the investigation on MRI and CT scans of the patient, where a contrast medium is

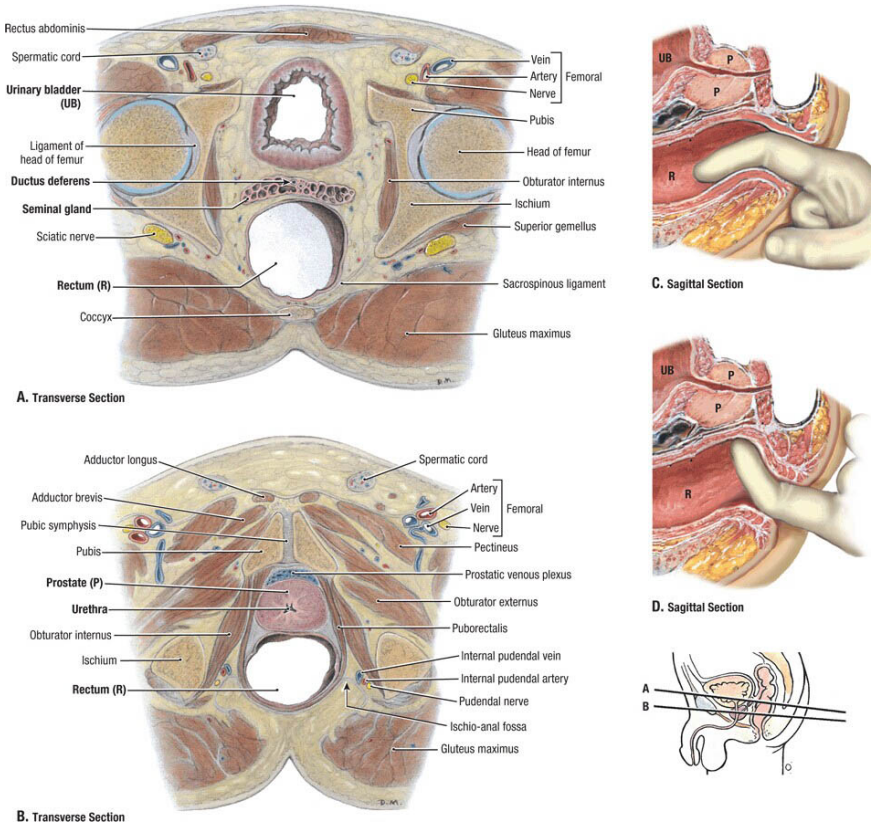

(a)

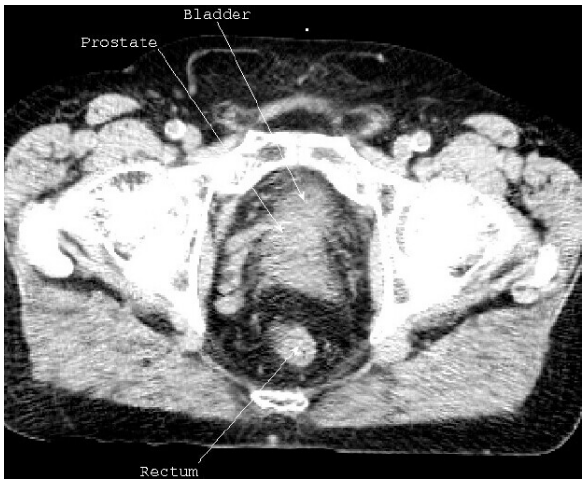

(b)

Figure 2.7: (a): The axial atlas of human pelvis from [44]. (b): The CT image corresponds to the position of the atlas [46]. On the CT image it can be seen that the soft tissue resolution and contrast is limited, and the boundary of bladder and prostate cannot be seen clearly. To define the extent of tumour growth requires considerable experience, and is subject to significant inter- and intra-clinical variability.

usually used to make the tumour clear. MRI is more frequently used in the diagnosis of a suspected brain tumour because of the clear anatomical detail and pathological information it provides.

Prostate Caner Diagnosis

A **Blood Test** is widely used to diagnose prostate cancer. Prostate-specific antigen (PSA) is a protein produced by cells of the prostate gland. High levels of PSA in the blood indicate the possibility of prostate cancer. **Image based diagnosis** of prostate cancer usually involves MRI, CT and transrectal ultrasound (TRUS). In TRUS, a small ultrasound device is inserted into patient's rectum to produce sound waves that create a clear picture of the patient's pelvis. A **Physical examination** is also used to diagnosis prostate cancer. This includes the examination of the breasts, abdomen, and rectum, where a doctor will use a finger to check for signs, such as a lumpy, hard prostate. A **Needle Biopsy** is the only sure way to identify tumour type and grade. It takes samples of tissue for pathological investigation using a needle injected into organs. The tissues obtained are investigated under a microscope, which gives a definite diagnosis. Prostate biopsies are normally guided using the TRUS.

2.4.2 Grading

Grading is performed after cancer is diagnosed using pathological information from a biopsy. The brain cancer can be graded as low, intermediate or malignant. Gliomas are the most common primary brain tumours with an incidence of six to eight in 100,000 [47]. They are characterised by the range of clinicopathological features defined by the World Health Organisation (WHO) grading scheme [48]. Grade I gliomas (benign), which are commonly found in children, are slow growing with good survival after treatment. Total resection is often the only treatment required, however, this depends on the location of the tumour and the degree of infiltration of areas controlling vital sensory function. Grade II (malignant) to IV (highly-malignant) tumours are more diffuse and aggressive and are associated with poor prognosis (WHO grade II, 5-10 years, WHO grade III, 2-3 years, WHO grade IV, 1 year) [47]. Complete tumour resection is made difficult by the spread within the brain and is usually followed by radiotherapy or

chemotherapy to ensure that any remaining cancerous tissue is treated. High grade gliomas

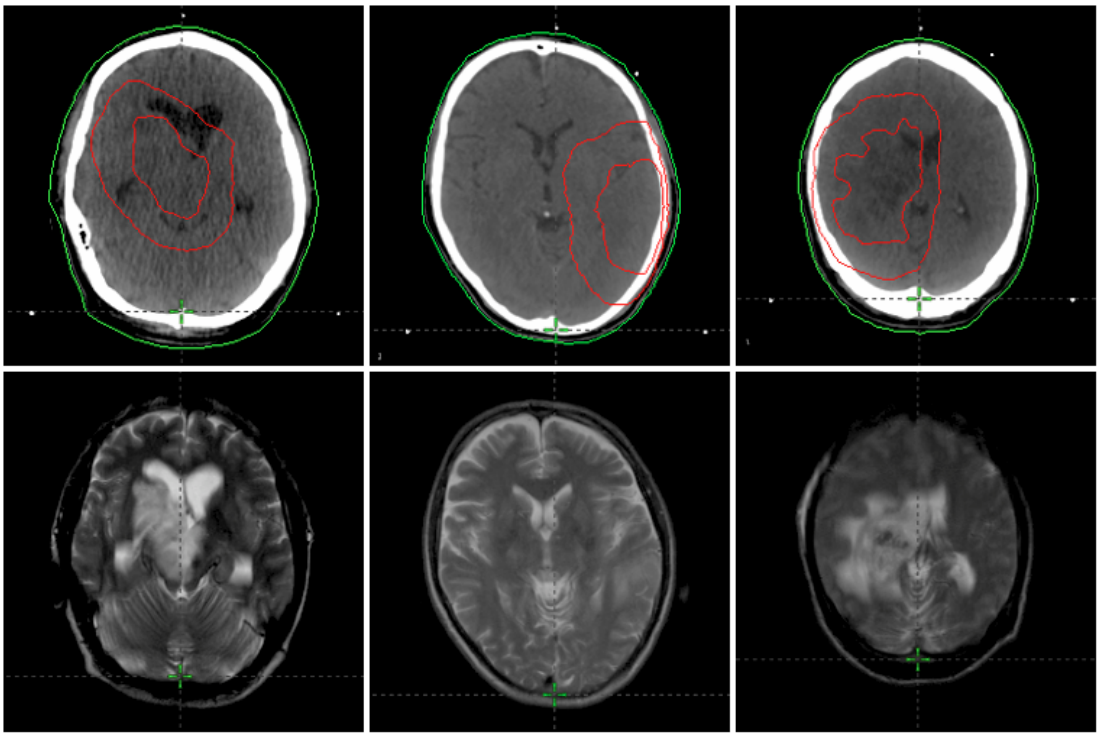

Figure 2.8: Extent of Grade II, (left), Grade III (middle) and Grade IV (right) glioma on registered post-surgical CT (top) and pre-surgical T2-weighted axial MR (bottom) images. The green contour visible on the CT images is the body contour used for radiotherapy planning. The outer red contour is the PTV, which takes account variations in size, shape and position, and the inner red contour is the GTV [10, 11]. The hyper-intense regions on the T2-weighted MR image volumes show the variability between grade II-IV gliomas.

tend to diffuse into surrounding healthy tissue more rapidly than low grade tumours, which proliferate relatively slowly. Grade IV tumours, which are particularly aggressive, form new vascularisation to support growth around a necrotic core. Figure 2.8 shows the MR and post-surgical CT for Grade II, III and IV brain tumours. The CT images also show the GTV contour (inner red contour) and the PTV (outer red contour), which takes into account variations in size, shape and position relative to the treatment beams [10, 11]. An irregular volume of the glioma can be observed in Figure 2.8, which demonstrates that the volume of glioma is highly unpredictable.

The Gleason grading system is used to evaluate prostate cancer. Prostate cancer is graded by its microscopic appearance of the biopsy specimen, by grade 1 to 5. Cancer with a higher Gleason grade are more aggressive and have a worse prognosis [49]. Pathologists examine

tumour tissue patterns and usually assign grades to the primary and secondary pattern observed in the specimen. These grades are then added to create the final Gleason score from 2 to 10. Gleason grade 3+3 or less tumour are considered as low risk cancer and have little danger of spreading rapidly. A score of 7 (4+3 or 3+4) is a moderate grade. Gleason scores 8 to 10 are more aggressive and tend to spread quickly and be associated with seminal vesicle involvement and node positivity.

2.4.3 Staging

The stage of a cancer defines the extent of the tumour growth and how far the cancer has spread. It is particularly important to know the stage before a decision is made about a treatment. It is a trivial job to stage brain tumours because most primary brain tumours do not usually spread beyond the CNS, hence there is no regularised staging system for brain cancer. The staging of prostate cancer is usually done by analysing diagnostic CT and MRI scans. Currently the most popular staging system is the TNM system (tumour, node, metastasis). A T category prostate cancer remains in the local area of primary tumour, N category cancer indicates enlarged lymph nodes while M category cancer refers to remote metastasis. In this thesis, only T category cancer are discussed. In prostate cancer, T category prostate cancer can be further classified into 4 stages:

T1: The tumour is within a small area in prostate gland, and it cant be felt by rectal examination.

T2: The tumour is larger than T1 stage, and can be felt by rectal examination.

T3: The tumour has spread outside of the prostate gland, invading into the seminal vesicles.

T4: The tumour has spread into the surrounding organs in the pelvic region, such as rectum, bladder and muscles of the pelvis.

2.4.4 Choice of Cancer Treatment

As previously mentioned, there are many treatment methods available for cancer patients: surgery, radiotherapy, chemotherapy, biological therapy, and more commonly a combination of two or more of these.

Surgery refers to the removal of tumours by a surgical procedure. A craniotomy is the most

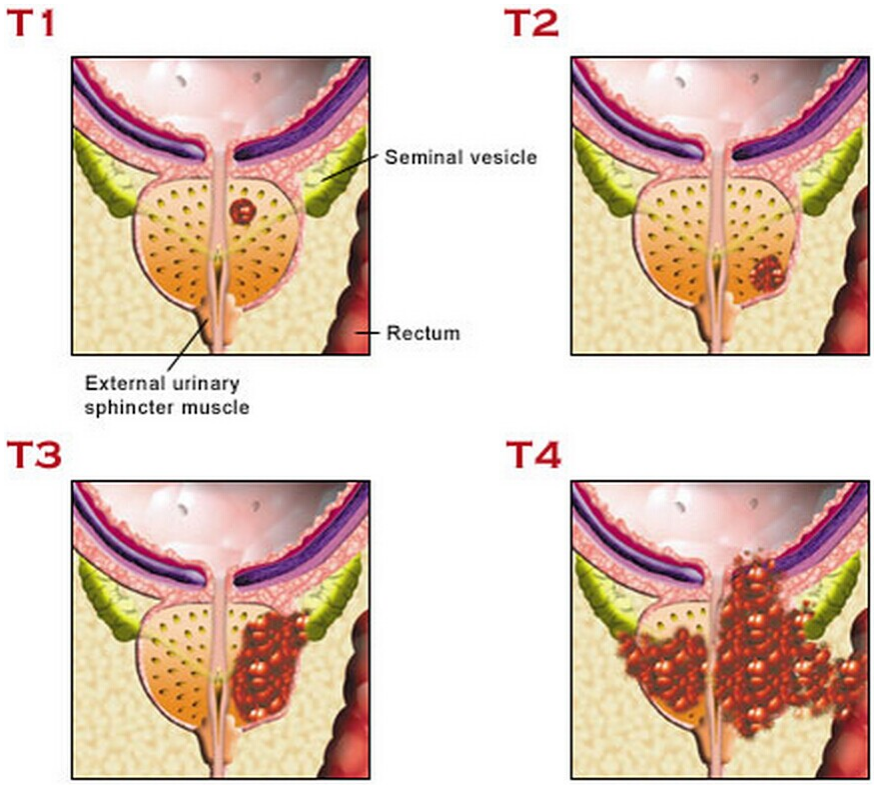

Figure 2.9: The stage of a prostate cancer refers to how far the cancer has spread. T1 is the earliest stage of prostate cancer (top left); from stage T2 (top right), the tumour is larger than T1, the prostate gland is harder and can be felt by rectal examination; T3 tumour starts to spread outside the prostate gland, invading to seminal vesicles; T4 tumour (bottom right) has invaded further to surrounding organs, rectum and bladder etc. [50].

common type of operation for a brain tumour. A small area of the skull is removed providing an opening where surgeons can operate.

Many prostate cancer patients suffer from difficulty in urinating caused by a tumour in the prostate pressing on the urethra. Trans-urethral resection (TUR) is carried out by passing a resectoscope through the urethra, and operating with a resecting loop until the blockage is removed.

It is likely that surgery will fail to remove all cancerous cells, therefore chemotherapy and radiotherapy may be used after surgery to further treat any remaining cancerous tissues.

Radiotherapy uses radiation to kill tumour cells by damaging their DNA. Radiotherapy is increasingly popular in cancer treatment due to advances in IMRT and IGRT, which make it possible to direct a highly concentrated dose to the tumour whilst sparing the surrounding healthy tissues. Since this thesis focuses on automatic contouring for radiotherapy, the proce-

dures of radiotherapy are introduced in detail in Section 2.5.

Chemotherapy uses a combination of drugs to kill cancer cells by damaging their DNA when they divide. Drugs in chemotherapy can be given either in tablet form or by direct injection into the blood stream. Chemotherapy only works for certain types of brain tumours because of the existence of the blood brain barrier. Chemotherapy is used to treat prostate cancer that has spread to other parts of the body and used mainly if hormone therapy is not controlling the cancer.

Hormone Therapy works by altering the production of particular hormones in the body. Cancer of the prostate gland depends on the male hormone testosterone, therefore lowering the amount of testosterone in the body can consequently reduce the chance of relapse after an early stage prostate cancer.

Biological therapy refers to enhancing the immune system of the body to eliminate cancer cells. For example, liquid containing weakened bacteria may be applied to the prostate weeks after TUR to aid the immune system in killing cancer cells.

2.5 External Beam Radiotherapy

Developments in imaging technology and improvements in computing power have significantly improved radiation treatment delivery in the past two decade. The delivery of radiation has moved from conventional radiotherapy using simple rectangular treatment fields to increasingly conformal radiotherapy techniques such as three dimensional conformal radiotherapy (3DCRT) and IMRT. The invention of the LINAC built the foundation of the modern external beam radiotherapy. The LINAC uses microwave technology to accelerate electrons to collide with a heavy metal target, producing high energy X-rays from the collisions. The high-energy X-rays are shaped by an exit collimator on the LINAC machine as shown in Figure 2.10a. The LINAC exit shape conforms to the tumour shape at any angle of view the focused high-energy X-rays are directed to the patient's tumour region, as shown in Figure 2.10b. External beam radiotherapy is the most widely applied radiotherapy treatment in modern hospitals and cancer centres, in the forms of IMRT, IGRT, stereotactic radiotherapy (SRT) and stereotactic body radiotherapy

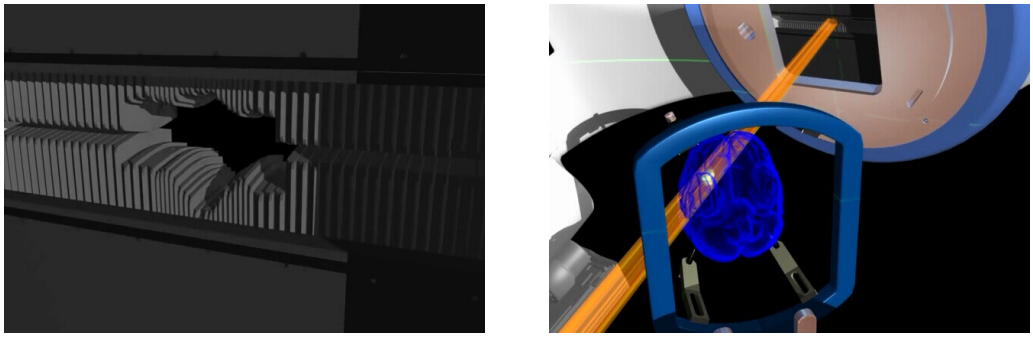

(a) (b)

Figure 2.10: (a): The multi-leaf collimator exit used in LINAC to conform high-energy X-rays to the shape of tumour definition. (b): Focused X-rays beams are directed to the patient's tumour region [51].

.

(SBRT). In this section, the main procedures used in modern external beam radiotherapy are discussed in 3 steps, including target localisation, dose calculation, and treatment delivery. The merits brought by IMRT, IGRT and SRT are also covered.

2.5.1 Target Localisation in Radiotherapy Planning

Target localisation or contouring refers to the definition of the tumour on medical images and includes the definition of radiation sensitive tissues close to the tumour region. Contouring of GTVs is carried out manually by experienced radiologists or oncologists. As mentioned in Section 1.2, the ICRU [11] defines important volumes to be defined in the planning of cancer radiotherapy as shown in Figure 1.2: GTV, PTV, CTV, and OAR which are described below for brain cancer and prostate cancer, based on ECC radiotherapy protocols.

GTV defines the growth of the malignant tumour, indicating extent and location, which is delineated manually by oncologists.

CTV contains both the GTV and sub-clinical microscopic malignant spread around the GTV. In brain cancer this microscopic growth may be difficult to identify on medical images, therefore the CTV is defined mainly on the tumour grade. For grade II glioma, a margin of 0.3-0.5 cm is usually added to the GTV, while for grade IV giloma, the margin increases to 2.0-2.5 cm, since grade IV lesions are more diffuse. The CTV margin for prostate cancer (Gleason score 7 and higher) is usually 1 cm all around expect posteriorly 0.6 cm, for a more focused dose in fewer

fraction, the margin reduces to 0.5 cm all around expect posteriorly 0.3 cm.

PTV takes account of all the geometrical motions and variabilities to ensure that the planned dose of radiation will cover the CTV volume. Patient movement such as breathing, rectal activity, and equipment setup errors are considered in the definition of PTV. The PTV to CTV margin for glioma is 0.3-0.5 cm. The PTV for prostate cancer is CTV plus a 1 cm margin everywhere except 0.6 cm posteriorly in treatment phase one, and 0.5 cm all around in treatment phase two, if needed.

OAR refers to organs, tissues which are sensitive to radiation, and spatially close to the GTV. When treating a brain tumour, cranial nerves need to be excluded from the GTV definition. Bladder and rectum are likely to be considered as OARs in prostate cancer. The definitions above describes the GTV and the margins added to the GTV to form the final PTV for radiotherapy treatment delivery. It is easy to understand that the accuracy of GTV contouring has a significant impact on the treatment performance. CT is the most widely used modality for tumour localisation as it provides undistorted spatial geometry. However, the key limitation of CT scans are the soft tissue contrast, which results in the homogeneity in tumours and OARs. A combination of MRI and CT modalities is recommended for brain tumour delineation for treatment planning to avoid inter- and intra- observer variability [52]. GTV delineation on the registered MRI and CT fusion is considered as a better solution than stand-alone CT [53].

2.5.2 Dose Calculation and IMRT

In radiotherapy, dose is the quantity of radiation received by the target volume and the OARs, and is measured in gray (Gy). Doses from 45 to 60 Gy are commonly used for curative radiotherapy of brain glioma and prostate cancer. The maximum dose received by OARs must be considered to prevent side effects. However in planning, the dose constraint for certain OARs might not be achievable. It is predictable that in the treatment of stage T3 and T4 prostate cancer the involvement of seminal vesicles will result in a significant amount of the rectum being covered by the PTV volume. In this case, IMRT will be needed to deliver the dose. Unlike conventional 3DCRT, IMRT directs multiple intensity modulated beams from different angles to the GTV. The radiation dose is elevated in the GTV while the radiation in the surrounding

tissue and OARs is reduced or avoided completely. Using IMRT, the prostate, seminal vesicles and the pelvic nodes can be irradiated with an acceptable level of dose received by the gastro-intestinal and genitor-urinary system, significantly reducing the rectal toxicity [54]. In the UK, the proportion of centres offering IMRT has increased from 46% to 81% between 2007 and 2012 [55]. Figure 2.11 shows a 3D radiotherapy planning application for IMRT.

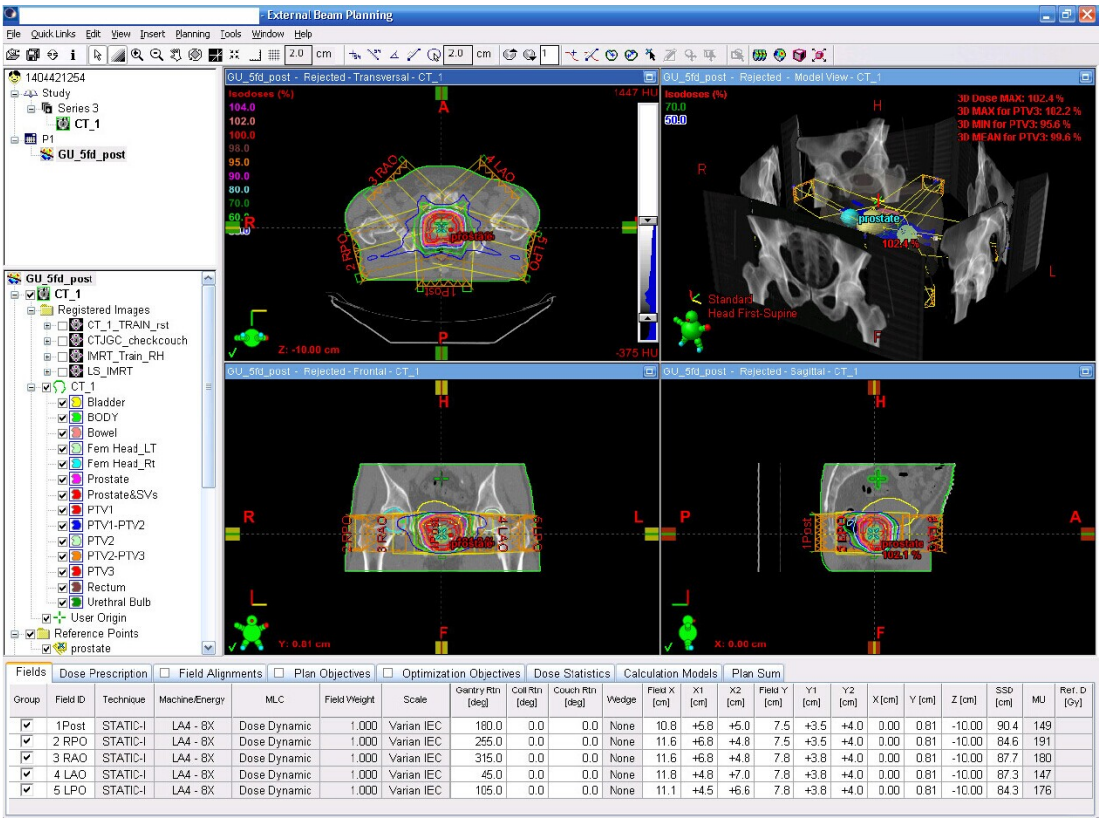

Group	Field ID	Technique	Machine/Energy	MLC	Field Weight	Scale	Gantry Rtn [deg]	Coll Rtn [deg]	Couch Rtn [deg]	Wedge	Field X [cm]	X1 [cm]	X2 [cm]	Field Y [cm]	Y1 [cm]	Y2 [cm]	X [cm]	Y [cm]	Z [cm]	SSD [cm]	MU	Ref. D [Gy]
☑	1Post	STATIC-I	LA4 - 8X	Dose Dynamic	1.000	Varian IEC	180.0	0.0	0.0	None	10.8	+5.8	+5.0	7.5	+3.5	+4.0	0.00	0.81	-10.00	90.4	149	
☑	2 RPO	STATIC-I	LA4 - 8X	Dose Dynamic	1.000	Varian IEC	255.0	0.0	0.0	None	11.6	+6.8	+4.8	7.5	+3.5	+4.0	0.00	0.81	-10.00	84.6	191	
☑	3 RAO	STATIC-I	LA4 - 8X	Dose Dynamic	1.000	Varian IEC	315.0	0.0	0.0	None	11.6	+6.8	+4.8	7.8	+3.8	+4.0	0.00	0.81	-10.00	87.7	180	
☑	4 LAO	STATIC-I	LA4 - 8X	Dose Dynamic	1.000	Varian IEC	45.0	0.0	0.0	None	11.8	+4.8	+7.0	7.8	+3.8	+4.0	0.00	0.81	-10.00	87.3	147	
☑	5 LPO	STATIC-I	LA4 - 8X	Dose Dynamic	1.000	Varian IEC	105.0	0.0	0.0	None	11.1	+4.5	+6.6	7.8	+3.8	+4.0	0.00	0.81	-10.00	84.3	176	

Figure 2.11: A 3D IMRT plan of prostate cancer. The contoured CT pelvic images in three planes: axial (upper left), coronal (lower left) and sagittal (lower right) as well as a 3D visualization (upper right) of the IMRT beams from different angles focus on the PTV while sparing the OAR. For traditional 3DCRT the intensity of each beam is uniform and as a result, the accuracy is limited. IMRT uses non-uniform, modulated fluencies of rays (photon, electron or proton) to irradiate the target volume, the resolution of dose delivery is significantly increased.

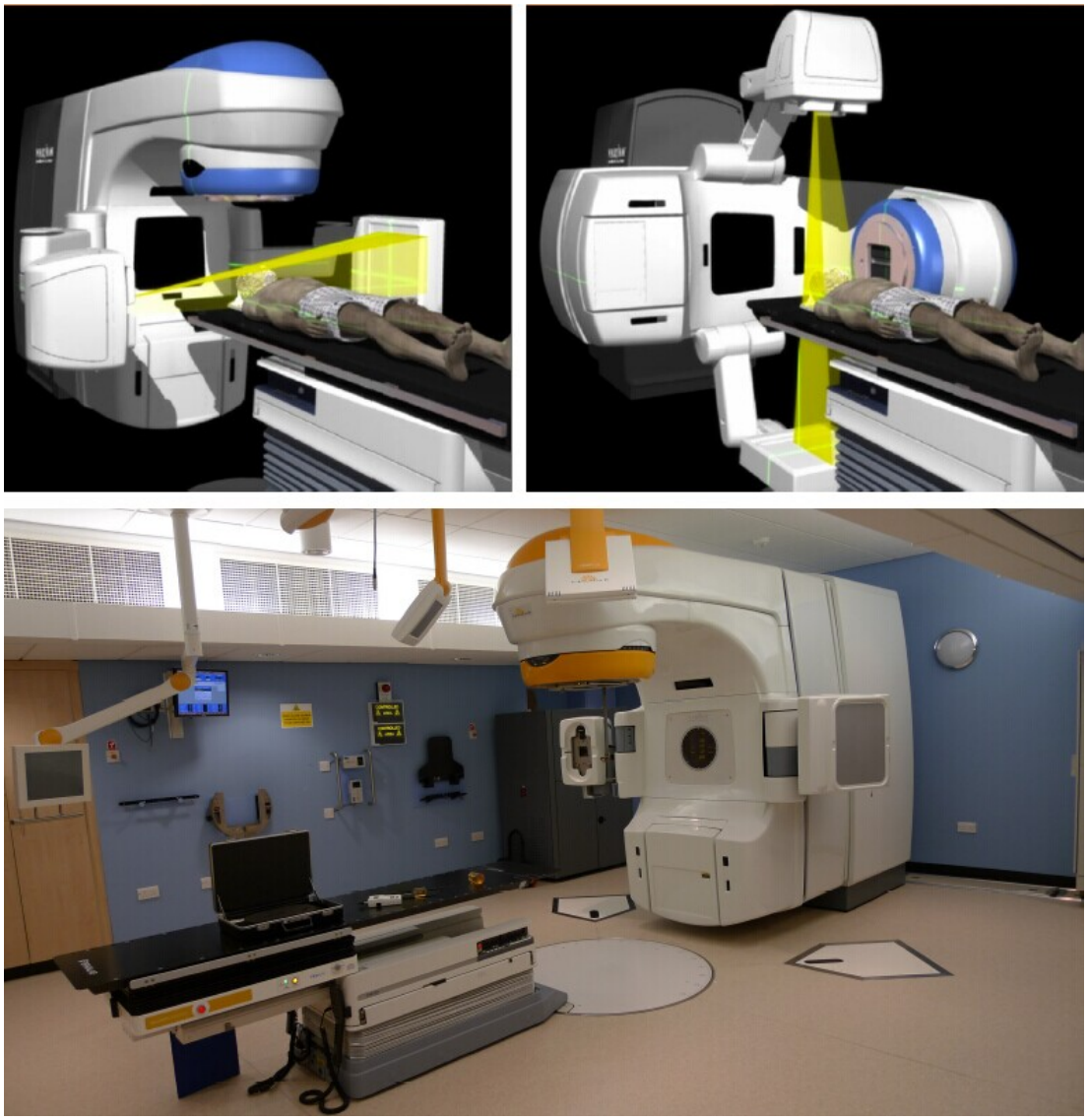

Figure 2.12: IGRT facility in ECC. Upper: acquisition of CBCT. Bottom: Novalis TX^{TM} linear accelerator equiped with CBCT and floor/ceiling mounted X-ray imaging units for 2D image acquisition. By using imaging as a guidance during the treatment time, the GTV and CTV can be defined instantly and as a result, the accuracy of PTV definition is increased [51].

2.5.3 Verification, Treatment Delivery and IGRT

Before treatment delivery, treatment verification will be carried out to ensure radiation delivery is as expected. In Section 2.5.1, it was shown that PTV definition accounts for the uncertainty from organ movement, patient motion and equipment set up errors. Conventional radiotherapy uses a larger than necessary PTV to make sure that the tumour volume is irradiated, causing unnecessary damage to healthy tissues. In certain highly aggressive tumours there may be growth during the treatment planning stage, which means that the planning CT scans are likely to be sub-optimal. IGRT can be used to resolve these issues, by acquiring images shortly before or during the radiation delivery from the OBI device. IGRT information offers the potential to update the PTV, thereby resolving the uncertainty and improving the quality of treatment plan. IGRT is often crucial to the use of IMRT because the non-uniform dose across the field carries a risk of overdose to the normal tissues. Most centres delivery IMRT under the guidance of IGRT [56].

2.5.4 The Future Advance of Radiotherapy: Computer-guided Real-time Radiotherapy

With the establishment and continued development of IMRT and IGRT, higher doses can now be delivered accurately to a smaller PTV even when the target volume is close to radiation sensitive tissues. SRT and SBRT delivers precisely-targeted radiation at much higher doses, in only a single or few treatment fractions, compared to traditional radiation therapy. However, these advanced radiation delivery techniques call for more reliable and accurate GTV contouring than ever, otherwise, the treatment will be significantly compromised or even lead to the failure of the treatment. GTV delineation is now one of the most important tasks in radiotherapy and is challenging because the images used for contouring, usually CT, suffer from low image resolution and poor soft tissue contrast. In modern radiotherapy, GTV contouring is still carried out manually by experienced oncologists. This can lead to a highly subjective definition of the GTV with high inter- and intra- clinician variability reported in prostate [15] and brain cancer [14]. Image enhancement techniques might be helpful in reducing the variability in tumour contouring. A machine standard definition of the GTV is more likely to be a straight-forward

solution, by providing reliable and reproducible contours. The availability of a large contoured archive for a specific tumour type may help in defining an inter-patient GTV standard. This could be used to supervise the machine outlining, and has the potential to produce more objective contours. Additionally, manual contouring is still one of the most time consuming processes in the cancer treatment cycle. Recall the concept of IGRT, when a live visualisation of the patient tumour region is obtained, however, it is not feasible to have an oncologist present to contour the new images at the time of treatment. Consequently, the volume and shape changes of GTV between the treatment planning scan and the treatment delivery, or even between fractions are ignored. A sub-optimal treatment plan will no doubt compromise any advantage of IGRT and degrade the quality of the treatment. Hence, a real time computerised modification of the treatment plan based on IGRT images at the time of irradiation has a meaningful value in improving the treatment performance. In order to fully utilise IMRT, IGRT and SRT technologies, a new approach to radiotherapy treatment, brought about by an automatic contouring system, is required. The flow chart in Figure 2.13 demonstrates the pipeline of the computer-guided real-time radiotherapy (CGRRT) presented in this thesis. It is based on an automatic delineation system using computerised deformable models, which could be the future of modern radiotherapy.

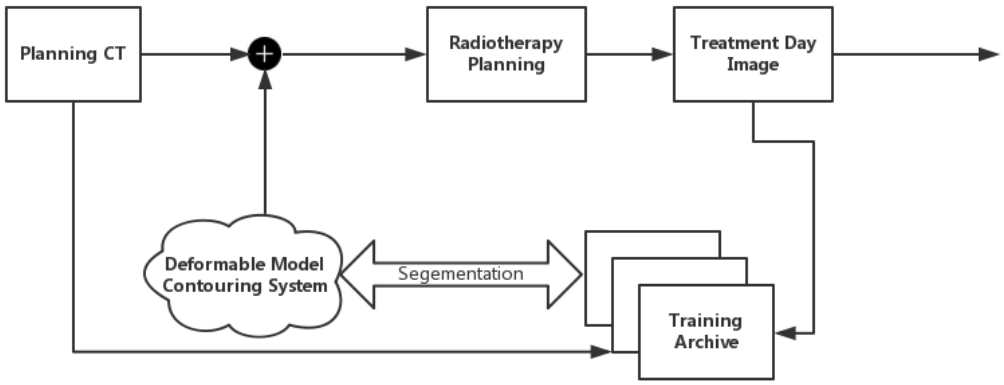

Figure 2.13: The CGRRT work flow, an automatic contouring system is constructed based on the pre-contoured planning CT scans. This model can be used to segment new patient's CT for radiotherapy planning and update treatment plan after fractions based on treatment day image. Once the updated plan is approved by doctors, treatment day image is stored into the training archive of the contouring system and revise the contouring systems parameters.

2.5.5 Summary

In this chapter, the necessary background was introduced to demonstrate the development and challenges in modern radiotherapy. The advantage and disadvantages of image CT and MRI modalities have been described. Basic anatomical information on human brain and pelvic region is illustrated, with an emphasis on the OARs at each site. The treatment choice for brain and prostate cancer are listed, together with the detail of external beam radiotherapy. IMRT and IGRT are emphasised to explain why an automatic contouring system is highly desired in modern radiotherapy.

Chapter 3

Review of Medical Image Processing Methods

3.1 Introduction

In Chapter 2 the importance and benefits of developing computerised automatic GTV contouring systems for radiotherapy planning was addressed. In parallel with the advances in IMRT, IGRT and SRT, this has the potential to significantly improve the performance of radiotherapy. GTV contouring can be defined as the segmentation or partitioning of a medical image into non-overlapping regions defined as GTV, OAR and other normal tissues. In this chapter major medical image segmentation techniques are reviewed, together with low level feature extraction methods, which may be helpful in building a contouring system.

Deformable models have been established as one of the most successful segmentation methods in the interpretation of medical images and other applications [1]. In this thesis, deformable models are divided into FDMs and SCDMs, depending on the freedom of the deformation process as introduced in Section 1.3.3. FDM can be classified as unsupervised segmentation, because it segments an image based on the natural statistics of the pixels. FDM deformation is normally driven by certain energy forces, including an external force pushing the parametric contour towards the object boundary and an internal energy to control the elasticity and rigidity of the contour. The key limitation of edge based FDM methods is boundary leakage when the propagation encounters weak or missing boundary. FDM includes the well known active contours method (snake) [21], level set methods [25] and other improved versions of these [57, 58]. SCDM segmentation is constrained by a statistical model of shape variations learnt from image stacks with contoured target volume. This makes the SCDM a supervised segmentation method,

where the contour or volume is represented by a set of landmarks. Segmentation of a new image is achieved by matching the position of landmarks to a new image (active shape model (ASM) [26]) and both the position of landmarks and a representation of object appearance to an image (active appearance model (AAM) [59]). ASM and AAM have been shown to be efficient in many application areas, including face recognition [60], industrial inspection [26] and medical image interpretation [61].

This chapter is organized as follows: Section 3.2 covers the fundamentals of image analysis and introduces the representation of digital image segmentation. In Section 3.3, low level segmentation methods including thresholding, edge indicators and morphological operations are addressed. The potential of these methods for segmentation of high grade gliomas is presented in Section 4.4. Standalone image gray levels, especially CT images, provide limited information for the delineation of the GTV. Image texture analysis is reviewed in Section 3.4, which was introduced to increase the robustness of GTV boundary definition in the construction of ASM for prostate GTV. Registration based methods have been shown to be successful in many medical image processing applications. Point set registration and image registration methods are reviewed in Section 3.5. These play important roles in the accurate construction of deformable models. A B-spline based free form deformation (FFD) method and coherent point drift (CPD) non-rigid point set registration method are reviewed. In section 3.5 and Section 3.6, FDMs and SCDMs are reviewed with expansions, including applications to medical cases.

3.2 The Fundamentals of Digital Medical Image Segmentation

A two-dimensional (2D) digital image can be thought of as a sampled and quantized traditional film-based image defined as an array function $I(x;y)$, with respect to the spatial index x and y. A stack of 2D images forms a three-dimensional (3D) or volume image, represented as a function $I(x;y;z)$ of three variables. Computers are able to reveal 'invisible' statistical features of these discreet digital arrays, and interpret them as desired. In a 2D digital medical image, each sampled element of the image array is called a pixel (voxel for 3D image), the word pixel is based on a contraction of pix ('pictures'). The size of a pixel in the real physical world is called the resolution, the spatial indexes of pixels are called the co-ordinate system

and the functional value of the pixel is called the intensity, or gray level, which are used interchangeably. Computers are able to read digital images as matrices, interpret the image using various mathematical operations, and provide useful information on the image. With the information provided, individual pixels can be grouped based on their similarities, each group forms a subset of the image $S \subseteq I$ representing one semantic entity, where I represents the whole image matrix. This process of generating semantic entities is called segmentation/classification. In medical image analysis, segmentation often targets to organs, GTV, or any other region of interest (ROI).

3.2.1 Segmentation Representation

The border of two segmented semantic regions is known as the boundary, which defines the extent of the semantic regions. In 2D medical image processing, the boundary of an ROI is usually called a contour in the form of a simple closed curve (Figure 3.1a) by connecting points $C(x_i, y_i)$ (Figure3.2), considering the discrete nature of a digital image [21]. A simple closed curve is a curve that does not cross itself and ends at where it starts, $C(1) = C(end)$ as shown in Figure 3.1a. A closed curve might cross itself as shown in Figure 3.1b. While an open curve have end points which do not join up $C(1) \neq C(end)$ as shown in Figure 3.1c. In the case of 3D image processing, a close surface of points $S(x_i, y_i, z_i)$ can be used to describe a volume of interest. The key problem of medical image analysis and in particular image segmentation is to move these points to the desired position where the edge lies, usually corresponding to an intensity change or other high level statistical change. The movement is driven by certain forces, curvature and gradient flow are widely used forces. An example of contour evolution driven by curvature is demonstrated in Figure 3.2, where points are moved normal to the contour, at a speed depending on the local curvatures. Grayson et al. [62] proved that no matter how convoluted a curve might be, local curvatures can quickly relax the curve into a circular object without crossing over itself (Figure3.3). It is essential that the points on a boundary $C(x_i, y_i)$ or surface $S(x_i, y_i, z_i)$ move in profiles perpendicular to the contour or surface. Only in this case does the contour or surface representation maintain its own point correspondence and a constant position with respect to surrounding structures. This is particularly important in the

segmentation of medical images because local image features are not sufficient to distinguish the ROI interior and exterior.

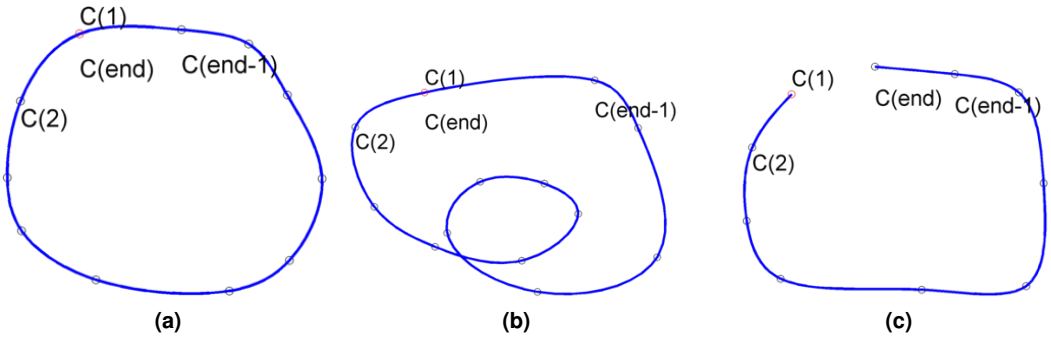

Figure 3.1: (a) A simple closed curve is a curve that does not cross itself and ends at where it starts. (b) A closed curve might cross itself, and (c) an open curve have end points which do not join up [62].

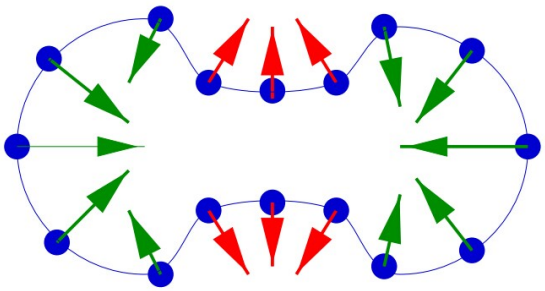

Figure 3.2: Contour points movement represented by arrows, the direction and length of the arrow is determined by local curvatures. Curvature is related to the amount by which a curve deviates from being flat, and the direction or sign of the local curvature is depending on the whether the curve is locally going clockwise or anti-clockwise as shown above [63].

3.3 Low Level Segmentation Methods

Low level segmentation methods are methods which may not be successful in the definition of GTV if applied in isolation, however, they may be helpful with deformable models. In this section the principles of low level segmentation methods including thresholding, edge detection operator and morphological operations are briefly addressed.

Figure 3.3: Motions under curvatures: the complicated object in the very left shrinks to a circular object and it is believed that it will collapse to a point and disappear finally under the motion driven by local curvatures [63].

3.3.1 Thresholding

Thresholding approaches segment scalar images by creating a binary partitioning of the image intensities based on an certain intensity value called a threshold. More than one threshold can also be used, which is called multi-thresholding. Thresholding is a simple yet often effective method for segmenting images where different structures have contrasting intensities or other quantitative features. When an image histogram shows clear intensity classes, 'valley' points indicate a threshold that is likely to separate the image into two classes. Otsu's method [64] is designed to automatically perform clustering-based image thresholding. In an example of using thresholding to segment rice on an image, $T1$, $T2$ and $T3$ are thresholds provided using Otsu's method from the image histogram in Figure 3.4c. The three thresholds partitioned the original image in Figure 3.4a into four classes in the different colours shown in Figure 3.4b. Thresholding is not capable of segmenting complex structures when the image histogram does not contain a significant threshold, which is very likely to happen when dealing with noisy images. Additionally, thresholding takes no account of spatial information in an image. Due to the illumination condition, rice grains at the bottom of Figure 3.4b, are misclassified as a fourth structure. Although thresholding has many drawbacks, it is often used as an initial step in an image processing approach by providing an estimated location of interested structure.

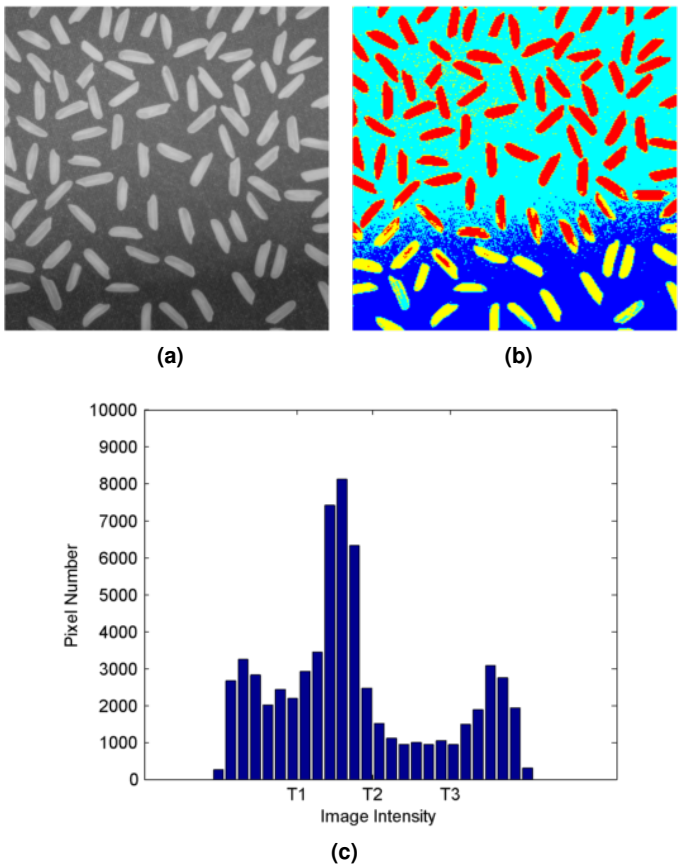

Figure 3.4: Simple segmentation using Otsu's thresholding. (a) Original image of rice being segmented; (b) Segmented structures in 4 different colours, bright background, dark background, rice on bright background and rice on dark back background; (c) Histogram of original image and thresholds used in segmentation.

3.3.2 Morphological Operations

Morphological operations are a collection of non-linear operations related to the structure shape or morphology of features in an image. Basic morphological operations includes erosion, dilation, closing and opening, which are especially well suited to the processing of binary images because the operations rely only on the relative ordering of pixel values rather than their numerical values. Morphological operations can also be applied to grey and colour images for interpolation purposes, which is beneficial in medical image volume reconstruction [65]. In this thesis the focus is on applying morphological operations to binary images.

A morphological operation on a binary image creates a new binary image in which the pixel has a true value only if the neighbouring pixels fit the shape or template called a structuring

element. The structuring element is a small binary image, i.e. a small matrix of pixels typically $3*3$ or $5*5$, each with a value of zero or one. The structuring element is applied at all possible locations in the image where it is compared with the corresponding neighbouring pixels with the same size as the structuring element. For a binary image $I(x,y)$, the **erosion** of I by a structuring element s is denoted as $I \ominus s$, producing a new binary image $I_{erosion} = I \ominus s$ with ones in all locations (x,y) of a structuring element's origin at which that structuring element s matches all the neighbouring pixels from the input image. The **dilation** of an image $I(x,y)$ by structuring element s denoted as $I \oplus s$, producing a new binary image $I_{dilation} = I \ominus s$ with ones in all location (x,y) of the origin of the structuring element at which at least one neighbour pixel matches the corresponding pixel in the structuring element. Erosion with small square structuring elements shrinks an image by stripping away a layer of pixels from both the inner and outer boundaries of regions, producing a smoothed shape by eliminating small details. Dilation and erosion are dual operations and have opposite effects. Dilation adds a layer of pixels to both the inner and outer boundaries of regions, and might merge small objects into a larger one.

Erosion and dilation can be cascaded to form compound operations such as **closing** and **opening**. The opening of an image I by a structuring element S(denoted by $I \circ s$) is an erosion followed by a dilation,

$$I \circ s = (I \ominus s) \oplus s \tag{3.1}$$

Closing denoted as $I \bullet s$ on the other hand is a dilation followed by an erosion,

$$I \bullet s = (I \oplus s) \ominus s \tag{3.2}$$

Morphological operations are suitable for processing binary images generated by thresholding during a segmentation task. Opening is so called because it can be used open up a gap between two large objects and restore the pixels at the boundary of large objects by the dilation. Similarly, the closing operation is so called because it can fill in holes inside an object and remove the added layer afterwards. Morphological operations act as shape filters by filtering out undesired details that are smaller in size than the structuring element such as small elements

from noise. The size of the structuring element needs to be carefully defined, in order to eliminate noisy details and spare objects of interest, for example the GTV from a medical image. In Figure 3.5, an MRI scan of the brain of a patient with a grade III glioma is used for the demonstration of morphological operations. The original MRI scan was firstly thresholded to produce the binary image shown in Figure 3.5b. The closing operation fills holes in Figure 3.5b to create the binary mask in Figure 3.5c, which may be considered as the binary mask for the whole skull. While the opening operation eliminates small elements depending on the operation kernel size, smaller regions are removed leaving the true region of interest, which in this case is the estimated position of the glioma, as shown in Figure 3.5d.

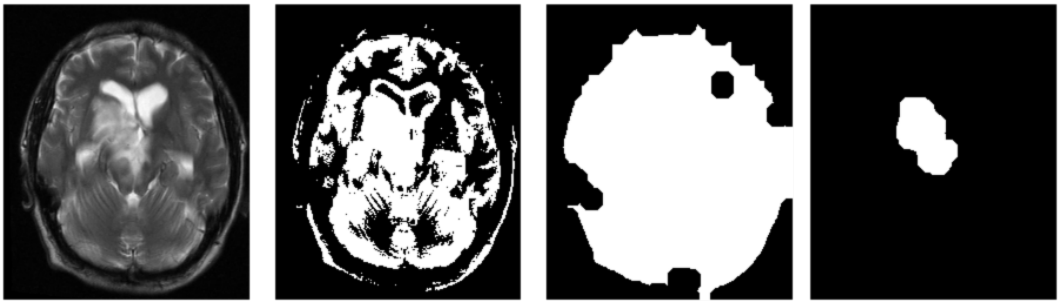

Figure 3.5: (a) A sub-image of size $259 * 209$ extracted from brain MRI scan. (b) Binary image mask generated using thresholding of (a). (c) Binary mask constructed from (b) using morphological closing (kernel size $10 * 10$). A larger kernel size may be able to fill the hole at the top right of the mask and smooth the boundary of the mask. (d) Binary mask constructed from (b) using morphological opening (kernel size $10 * 10$). A larger the kernel size leads to a smaller volume of the mask.

3.3.3 Edge Detection Operators

In an image an edge follows a path of change in image intensity. Edges are often associated with the boundaries of objects in an image. Edge detection operators are actually a series of high pass filters which capture significant change in intensity or other specific features. The Canny edge detector introduces the notion of non-maximum suppression, in which edge points are defined as points where the magnitude of the gradient assumes a local maximum in the gradient direction [19]. The Canny edge operator is widely used in image analysis as a state-of-art edge detection operator. However, it is tricky to apply in isolation to segment the GTV

volume in medical images. As shown in Figure 3.6, Canny edge operator successfully detected high gradient edges (red) including while matter, glioma and the skull, while the disconnected edges can not produce a closed contour of the glioma (blue). In this thesis, edge detection operators, including a Canny edge detector, were used in the pre-processing of T2-weighted brain MRI.

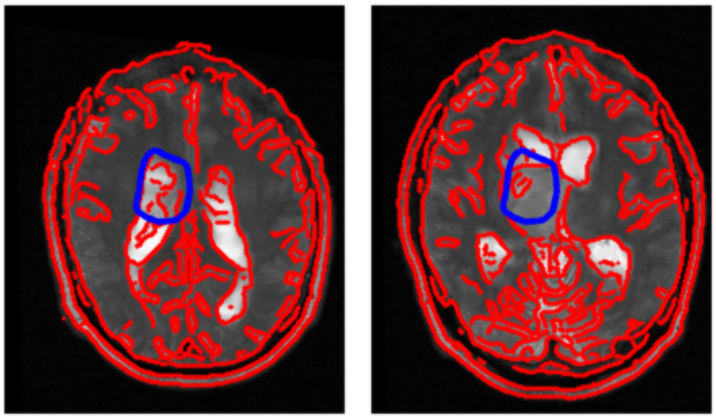

(a) (b)

Figure 3.6: Two sub-images of size $259 * 209$ extracted from an brain MRI scan processed by a canny edge detector. The red contour denotes the detected boundary, blue contours are clinical contours. The canny detector is able to detect some segments of true GTV contour, while it is embedded within other high gradient edges.

3.4 Image Features in Deformable Models

In addition to the edge features captured by edge detection operators, statistical image features are also heavily used in medical image analysis. The texture of an image is determined by the gray level distribution over the image. In this section statistical features based on texture are reviewed as a way of enhancing the saliency at GTV boundary regions.

Statistical methods firstly describe the spatial distribution of image gray levels by computing local features at each pixel in the image and deriving a set of statistics from the distributions of the local features. Depending on the number of pixels involved in defining the local feature, features can be further classified into first-order, second-order and higher-order features. First-order statistics estimate properties of individual pixel values, ignoring the spatial interaction

between image pixels. The image features based on first order distribution are by definition invariant to any permutation of the pixels, in other words, they are rotation and scale invariant [66]. Second- and higher- order features estimate properties of two or more pixels occurring at specified locations relative to the centre pixel, for example co-occurrence matrices and run-length matrices. The key limitation of texture analysis is the computational complexity of the algorithms and the requirement for building a classifier, particularly in the cases of higher order features. Texture classification is an important part of texture analysis and is used to assign an unknown region from a sample image to one of a known texture class. Texture classification is not however the main focus of this thesis, only first-order features will be reviewed in this section and interested reader should refer to [23] and [67] for more information about higher-order features.

3.4.1 First Order Distribution

First order distribution involves only consideration of one single pixel. For gray level $i(x,y)$ on an image region I_{local}, the distribution of intensity $p(i)$ is defined as:

$$p(i) = \frac{N_i}{N_I} \tag{3.3}$$

Here N_i refers to the number of pixels with gray level i, and N_I refers to the total number of pixels of local image region I_{local}. Equation (3.3) calculates the normalised image histogram. The first-order distribution is widely used in low-level feature extraction because it is simple to compute. By neglecting spatial relations, features based on the first order distribution are rotation and scale invariant, which makes them inherently suitable for a multi-scale modelling.

3.4.2 Low Level Image Features Based on First Order Distribution

Moments and entropy are often extracted from a distribution as statistical features and used for the segmentation of medical image data. Based on the definition of $p(i)$ in Equation (3.3), the mean μ and central moments σ_k of image I are given by,

$$\mu = E[i] = \sum_{i=1}^{N} ip(i) \tag{3.4}$$

and,

$$\sigma_k = E[i - E(i)^k] = \sum_{i=1}^{N} (i-\mu)^k p(i) \tag{3.5}$$

where N is the number of possible gray levels. The most commonly used central moments are variance, skewness and kurtosis given by σ_2, σ_3, and σ_4 respectively. Central moments measure the bias of the distribution from the centre mean. The variance is a measure of the histogram width that measures how far the local gray level is spread out. Skewness measures the degree of histogram asymmetry around the mean. Kurtosis is a measure of whether the distribution is peaked or flat relative to a normal distribution. Coarseness, also known as edge density, measures the number of edges present in the local image region. Energy is a term that measures the homogeneity of an image, also called uniformity, a large energy value is expected when local region gray levels are uniform distributed. The energy is calculated based on $p(i)$ as,

$$Energy = \sum_{i=1}^{N} p(i)^2 \tag{3.6}$$

Entropy was introduced in information theory by Shannon [68] to quantify the degree of randomness (information) in a communication. Similarly, given the image histogram $p(i)$, the entropy is calculated as,

$$Entropy = -\sum_{i=1}^{N} p(i) log_2(p(i)) \tag{3.7}$$

Textures have been shown to be helpful in improving the original ASM method by investigating local image texture instead of conventional image gray levels or gradients [69, 70]. On a $5*5*5$ volume box shifted within the patient's pelvic region that included the prostate, bladder and rectum, 3D textural features were calculated. Figure 3.7 visualises the texture images in 2D, from the top left to bottom right, original CT gray levels, mean, variance, coarseness, skew, kurtosis, energy and entropy images are listed. A large intensity variation is observed on the images at the true GTV boundary. An optimisation scheme can be applied to extract the most distinct features from these textural images to construct an ASM model driven by optimised texture, this is presented in Section 5.6.

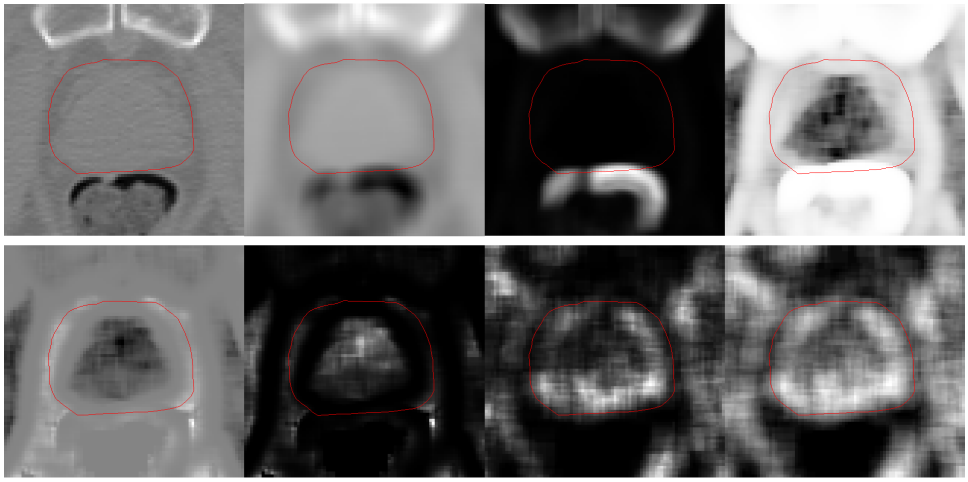

Figure 3.7: Prostate GTVs (red contour) on first order texture images. Top: Original CT, mean, variance, coarseness. Bottom: Skew, kurtosis, energy, entropy.

3.4.3 Image Features in Deformable Model Segmentation

Recall that in Section 1.3.2, the segmentation process using deformable models moves the contour points normal to the model boundary. Deformable models build a model of statistics and an error function that measures the residuals of the segmented data from the modelled data [66]. The interpreted image features modelled by deformable models are high level features.

Gradient Vector Flow Field

Gradient vector flow (GVF) proposed by Xu et al. [71] is considered to be a typical high level image feature widely used in active contour and LSM as shown in Figure 3.8. The GVF field $V(u(x,y),v(x,y))$ is a high level image feature derived from minimising the term as,

$$\varepsilon = \int\int \lambda(u_x^2+u_y^2+v_x^2+v_y^2)+|\nabla f|^2|V(u,v)-\nabla f|dxdy \tag{3.8}$$

where λ is a regularisation constant to balance the first and second term in Equation(3.8), $[u(x,y),v(x,y)]$ is the vector that describes the GVF direction and magnitude at image location $[x,y]$. ∇ is the gradient operator and f is the edge indicator as [72],

$$f = |\nabla G_\sigma * I|^2 \tag{3.9}$$

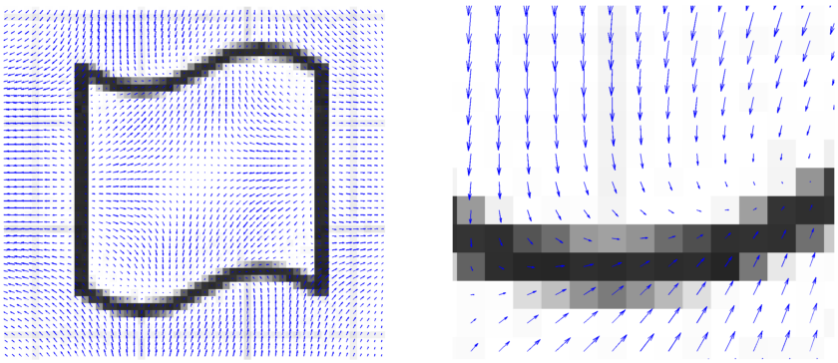

(a) (b)

Figure 3.8: GVF field calculated based on the local image gradient generates an external that drives contours towards edges with high gradient in the image.

or

$$f = -\frac{1}{1+|\nabla G_\sigma * I|^2} \tag{3.10}$$

where G_σ is a two dimensional Gaussian function, $*$ is the convolution operator. A high gradient leads to a strong edge f value. When the image edge f is weak, the first term in Equation(3.8) dominates and gives an smooth GVF. In the case when the image edge f is strong, Equation(3.8) is minimised by setting $V = \nabla f$. The GVF field in Figure 3.8b works as an external force used in FDMs, driving the contours towards an high gradient edges.

Image Feature in Active Shape Model

In the modelling of ASM, a vector of image gray levels normal to the boundary at a contour point is extracted from the image known as a profile, as shown in Figure 3.9a. The profile vector helps to locate the strongest edge along the profile, which is considered as the next movement for the model point, as shown in Figure 3.9b. In practice, the object boundaries do not always correspond to the strongest edge. The training archive used in building an SCDM provides the profile statistics for each contour points, which gives instruction about what to look for in the target image. The Mahalanobis distance (MD) between target image profile and modelled profile is used in the conventional segmentation of ASM to find the optimal displacement of model points [26]. Figure 3.10 gives an example of model points movement using a profile of length 5 pixels (2 pixels both sides of the model point). Given a model point, an image intensity

profile of length 14 pixels (10 possible displacement) is sampled from the target image normal to model boundary (top bar chart). The cost of fitting is calculated using the MD with respect to the 10 possible displacement along the sample. The model point chooses the one that gives the best match (lowest in the bottom bar chart). In this iteration, the model point will move 1 pixel to the left [73]. The MD takes into account the correlation and measures the distance between two vectors x and y, which has the same distribution with a set of observations $(x_1, x_2, \cdots, x_N)$ with means $(\mu_1, \mu_2, \mu_3, \cdots, \mu_N)^T$. Firstly the covariance matrix Σ is calculated as,

$$\Sigma = \begin{pmatrix} E[(x_1-\mu_1)(x_1-\mu_1)] & E[(x_1-\mu_1)(x_2-\mu_2)] & \cdots & E[(x_1-\mu_1)(x_N-\mu_N)] \\ E[(x_2-\mu_2)(x_1-\mu_1)] & E[(x_2-\mu_2)(x_2-\mu_2)] & \cdots & E[(x_2-\mu_2)(x_N-\mu_N)] \\ \vdots & \vdots & \ddots & \vdots \\ E[(x_N-\mu_1)(x_1-\mu_1)] & E[(x_N-\mu_N)(x_2-\mu_2)] & \cdots & E[(x_N-\mu_N)(x_N-\mu_N)] \end{pmatrix} \tag{3.11}$$

The MD between x and y is defined as [74],

$$D_m(x,y) = \sqrt{(x-y)\Sigma^{-1}(x-y)} \tag{3.12}$$

where Σ^{-1} is the inverse covariance matrix, also known as the concentration matrix.

There is a trade off between the length of the vector (profile length) and the statistical consistency, a longer profile length may reduce the consistency. As mentioned in Section.3.4.2, low level image statistics can be used in the profile instead of regular image gray levels to increase the accuracy of the segmentation. More detail about how this is done for an ASM from training images is addressed later in Section 3.7.1.

3.5 Registration Base Method

The term 'registration' refers to the determination of spatial alignment between two objects in the same or different coordinate systems. The registration transformation is referred to as a spatial mapping in geometry as T, which transforms a point X_A in an image I_A to another point as X_B in image I_B,

$$X_B = T(X_A) \tag{3.13}$$

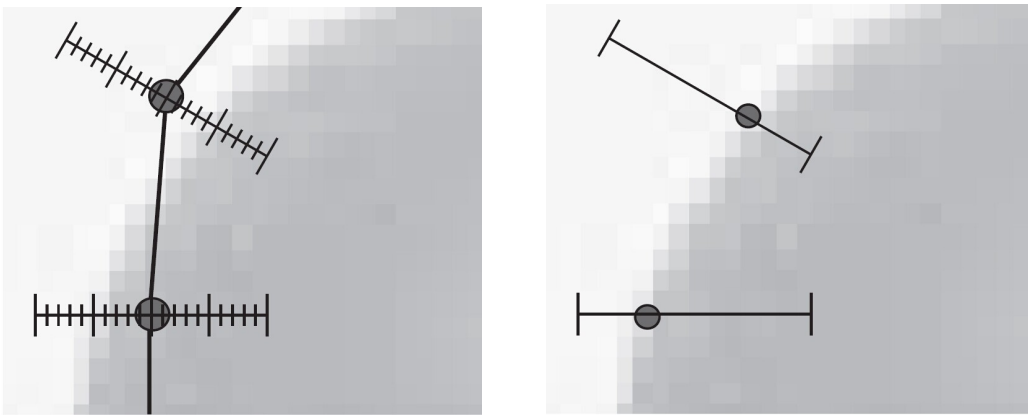

Figure 3.9: A vector containing image gray levels normal to the boundary at a model point is extracted from the image. This is called a profile. The profile vector helps to located the strongest edge along the profile, at which is considered as the next movement for the model point [73].

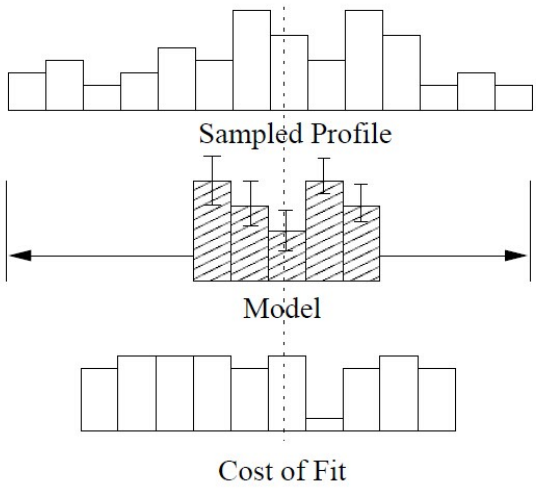

Figure 3.10: An example of ASM landmark movement using a model profile of length 5 pixels.

Here the image I_B is called the reference image (static image), and image A is called the target image (moving image). In the registration of two objects represented by the points, the spatial mapping T also provides the alignment and correspondence between two point sets. This is known as the point set registration. In order to merge the training archive into a model in building SCDMs, it is very important to accurately align the multiple contours/surfaces. A more complete mapping Γ maps both the position as well as the image intensity from image I_A to image I_B, taking account of the image re-sampling and resolution. The mapping Γ is

commonly known as image registration and aims to register different image modalities together for an integrated visualisation and combined analysis. In terms of medical image registration, MRI and CT are commonly registered because they contain complementary information, and when combined provide better soft tissue contrast and spatial consistency.

Image registration is highly related to correspondence, if correspondence is known, registration can be easily performed by computing the best rigid or non-rigid transformation between two points sets of object. Otherwise, the registration algorithm needs to determine the best transformation and correspondence simultaneously. This section firstly explains the differences between rigid, affine and non-rigid registration in Section 3.5.1. In Section 3.5.2 point set registration methods including ICP and CPD which solve the correspondence between two or more point sets are presented. Image registration is also covered with an emphasis on the B-spline based FFD which is presented in Section 3.5.4.

Table 3.1: Summary of Section 3.5

Criteria	Classification
Dimensionality	2D/3D
Nature of deformation	Rigid, affine and non-rigid
Point set registration	ICP, RPM and CPD
Image warping	Piece-wise linear, B-spline based FFD

3.5.1 Rigid, Affine and Non-rigid Deformation

The term 'rigid' means there is no warping allowed in the transformation T only rotation, translation and reflection. After a rigid transformation the points used to represent objects retain their relative distance to each other. Rigid registration allows only shape invariant transformation, hence rigid registration are expected to work very well with rigid objects such as bones [75]. An affine transformation allows more kinds deformation than rigid transformation such as scaling and shearing. Affine transform preserves colinearity and distance ratios, which means that points on the same line remain on the same line and the mid point of a line remains as the mid point after an affine transformation. Non-rigid deformation allows shape warping and all the other rigid and affine deformation. The typical requirements of non-rigid deformation are

smooth and invertible, which means topological change is not allowed [76]. In the segmentation of organs, non-rigid deformation is more widely used than rigid and affine deformation because topological change is very rare and change in size and shape are common. The shape alignment deformation based on rigid, affine and non-rigid deformation is demonstrated, Figure 3.11a shows the two point sets to be aligned, blue point set is the reference set and the green point set is the target set, the pixel distance between the two point sets are 206 pixels before alignment. Figure 3.11b shows the deformation using ICP rigid registration, resulting in the pixel distance of 105 pixels. Figure 3.11c applied an affine transformation and reduced the distance to 52 pixels. Figure 3.11d shows the non-rigid deformation and the distance reduced to 13 pixels.

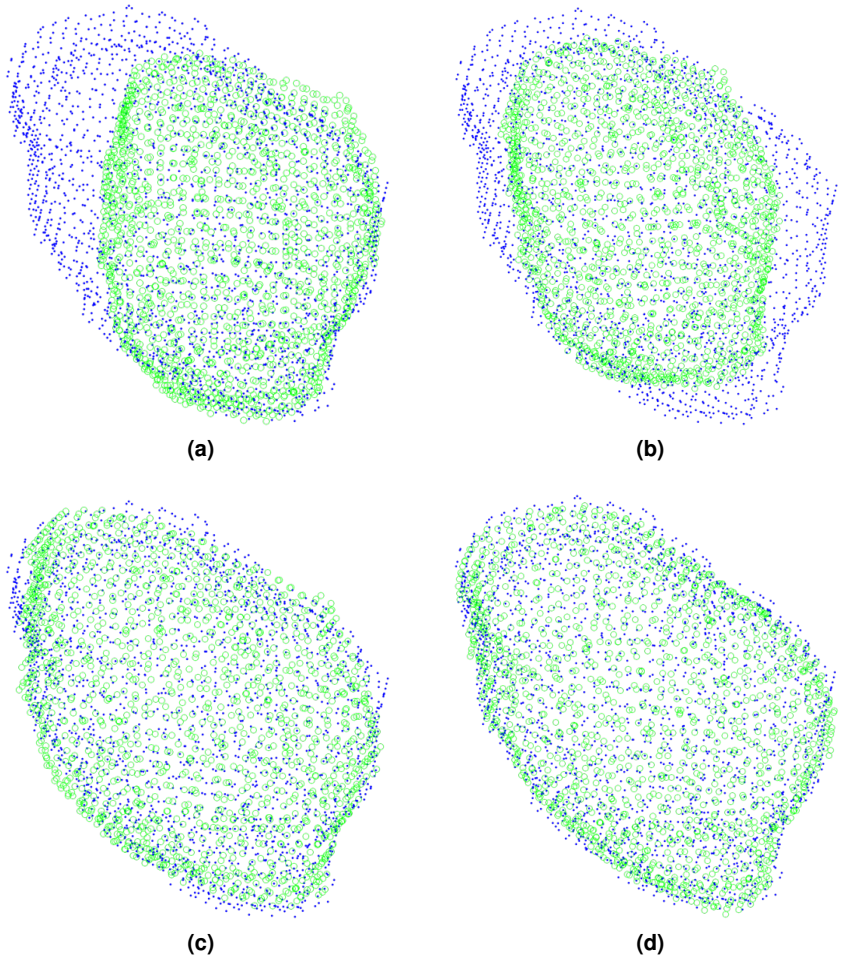

Figure 3.11: Shape alignment deformation between two point sets based on rigid, affine and non-rigid deformation.

3.5.2 Point Set Registration

Point set registration, also known as point matching, is an important process in the construction of SCDMs, by defining alignment and correspondence between training contours/surfaces, as shown in Figure 3.12. Despite differences in pixel gray levels, the vertices of points in

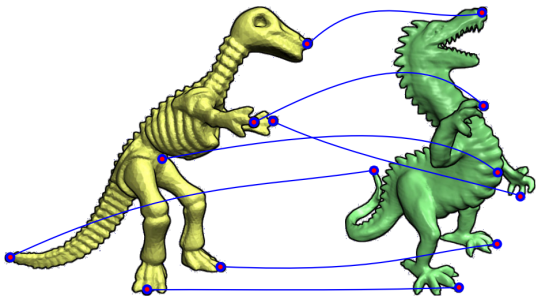

Figure 3.12: The correspondence (blue lines) between a set of feature points of each dino-skeleton (red marker). The large amount of geometric variations between the shapes usually make the computation of such a correspondence difficult [77].

the image where points are extracted (manually or automatically) are meaningful geometric features, which need to be accurately preserved before the analysis of object shape variation. This section presents several popular point set registration methods and a proposed group-wise registration algorithm for the merge of population data.

Iterative Closest Points (ICP)

The ICP algorithm is a conceptually simple method which performs a rigid alignment between surfaces represented by points [78]. The algorithm iteratively finds the point-to-point match that minimises the mean square distance between two point sets, where the cost function is,

$$MSE = \frac{1}{n}\sum_{i=1}^{n}(\hat{P}_i(\hat{x},\hat{y}) - P_i(x,y))^2 \tag{3.14}$$

Here $\hat{P}_i(\hat{x},\hat{y}$ and $P_i(x,y)$ are two matched points. Zhang *et al*. [79] proposed a modified K-D tree algorithm for efficient closest point computation to get points match efficiently. The rotation and translation matrix is acquired using singular value decomposition (SVD) to transform the target surface and obtain new $\hat{P}_i(\hat{x},\hat{y})$ [80]. The covariance matrix Σ is firstly obtained

to interpret the variance between two point sets as below,

$$\Sigma = \frac{1}{n-1}\sum_{i=1}^{n}(\hat{P}_i - \hat{\mu})(P_i - \mu)^T \tag{3.15}$$

where n is the total points number, μ is the mean of the point set and T represents the transpose. The SVD of Σ in Equation (3.15) is given by,

$$\Sigma = uSv^T \tag{3.16}$$

where u and v are orthogonal matrices containing eigenvector of σ, S is a diagonal matrix containing eigenvectors of Σ. The rotation matrix are computed from [80],

$$R = udiag(1,1,det(uv^T))v^T \tag{3.17}$$

followed by the translation vector,

$$d = \hat{\mu} - R\mu \tag{3.18}$$

Here, R is an orthogonal rotation matrix which contains rotation angles of the point set, and d is a vector that measures the translation. The new $\hat{P}_i$ is updated by,

$$\hat{P}_i = R * \hat{P}_i + d \tag{3.19}$$

These two steps are repeated until the MSE is minimised.

Robust Point Matching (RPM)

Robust Point Matching (RPM) first introduced by Gold et al. [81] and later well established by Chui et al. [82], which allows local to global search using deterministic annealing and soft assignment of correspondences between two point sets. The correspondence definition of RPM between any two points is firstly assigned within $[0,1]$ and ultimately converges to binary. The key advance in RPM than ICP is the correspondences found in RPM is always one-to-one, which is not always possible the case in ICP. The thin plate spline robust point matching (TPS-RPM) [82] parametrised the non-rigid transformation as a thin plate spine (TPS), which is a

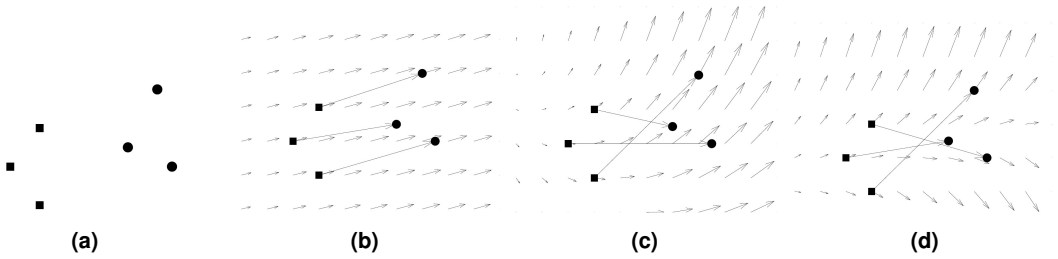

Figure 3.13: (a)Two points sets (3 points each, left and right). (b) A smooth coherent velocity field of the correspondences. (c) and (d) Velocity fields that are less coherent for the given correspondences.

solution of the interpolation problem in 2D that penalises the second order derivatives. The method cannot be extended to problems involving four or more dimensions, because the thin plate spline parametrisation only exists in 3D [83].

Coherent Point Drift

CPD method [84] introduces a new constraint to penalise the derivatives of all orders. This is called motion coherence, which was proposed in motion coherence theory [85]. It is natural that points close to each other of a surface should move coherently, resulting in a smooth transformation, as shown in Figure 3.13. Given two $2D$ dimensional point sets,

$$P_A(x_n, y_n),\ n = 1, 2, ..., N \tag{3.20}$$

and

$$P_B(x_m, y_m),\ m = 1, 2, ..., M \tag{3.21}$$

to be registered, $P_B(x_m, y_m)$ is considered as the centroids of a Gaussian mixture model (GMM), representing point set $P_A(x_i, y_i)$. The alignment of CPD can be understood as a probability density estimation problem, the correspondence is obtained using the maximum of the GMM posterior probability. The GMM probability density function for a point $a_n(x_n, y_n)$ within point set P_A is as follows,

$$p(a_n) = \sum_{m=1}^{M} P_B(m) p(a_n | b_m) \tag{3.22}$$

where $p(a|m)$ in 2D is the Gaussian distribution centred on point b_m within point set P_B as,

$$p(a_n|b_m) = \frac{1}{2\pi\sigma^2} exp^{-\frac{\|a_n - b_m\|^2}{2\sigma^2}} \tag{3.23}$$

As mentioned earlier, the transformation of CPD is defined as the initial pose plus a displacement $V(P_B)$ constraint by coherent velocity as,

$$T(P_B) = P_B + V(P_B) \tag{3.24}$$

A regularisation term of V as is used to regularize the smoothness of V,

$$\phi(V) = \int_{R^D} \frac{\tilde{V}(s)^2}{\tilde{G}(s)} ds \tag{3.25}$$

where $\tilde{V}$ is the Fourier transform of the velocity field and $\tilde{G}$ is the Fourier transform of Gaussian function G that approaches zero as scaling parameter $\|s\|$ is large. In addition to the negative log-likelihood of Equation (3.23), the following energy function is obtained,

$$E(V) = -\sum_{n=1}^{N} log \sum_{m=1}^{M} e^{-\frac{1}{2}\|\frac{a_n - b_m}{\sigma}\|^2} + \frac{\lambda}{2} \int_{R^2} \frac{\tilde{V}(s)^2}{\tilde{G}(s)} ds \tag{3.26}$$

where λ is a constant weight. The velocity field displacement V for non-rigid registration, which minimise the energy function (Equation (3.26)) is [84],

$$V(c) = \sum_{m=1}^{M} w_m G(c - b_m) \tag{3.27}$$

which has the form of basis function, where c indicates the points propagation. For more details about rigid and affine registration using CPD see [84].

3.5.3 Image Registration

An important branch of medical image analysis is medical image registration or image fusion, which is a process that combines complementary information of the same or different medical imaging modality. In clinical practice, radiotherapy planning CT images and diagnostic T2-weighted MR images are commonly registered to gain the soft tissue contrast and bony structures [86]. This section skips the image similarity and extraction of feature points in image registration because the given contour points are used as the feature points of registration in the study. Readers interested in a more comprehensive discussion of medical image registration are referred to [87, 88, 89] for more information.

Similar to point set registration, image registration can be categorised into rigid, affine and non-rigid registration based on the deformation used to register the image. The process that applies the calculated deformation to the moving image is called the image warping. This section focuses on a non-rigid image warping method using B-splines based FFD [76], which can be used to warp images into shape free patches for the analysis of the image appearance. In Figure 3.14 three image of labelled human faces from labelled faces (blue markers) in the wild (LFW) data is presented [90]. It is difficult to investigate the facial appearance in Figure 3.14 directly since they have different shapes. These labelled faces are warped into a standard shape (red markers) as shown in Figure 3.15. These marker performs as the feature points in image registration and the displacements between them generate a deformation filed based on FFD. Shape free patches in Figure 3.15 can be conveniently used in the investigation of appearance analysis of facial recognition [27].

3.5.4 FFD Based on B-spline

B-spline is short for basis spline, which is a function represented as a linear combination of basis functions. The most commonly used spline is cubic B-spline. Cubic B-splines can be used to create a smooth deformation of C^2 continuous of the images, which means first and second derivatives of the deformation are continuous. To defined a B-spline based FFD, the domain of the image volume is defined as $\Omega = \{(x,y,z)|0 \leq x \geq X, 0 \leq y \geq Y, 0 \leq z \geq Z\}$. Let Φ denote a n_x, n_y, n_z mesh of control points $\psi_{i,j,k}$ with uniform spacing d_x,d_y and d_z. The FFD

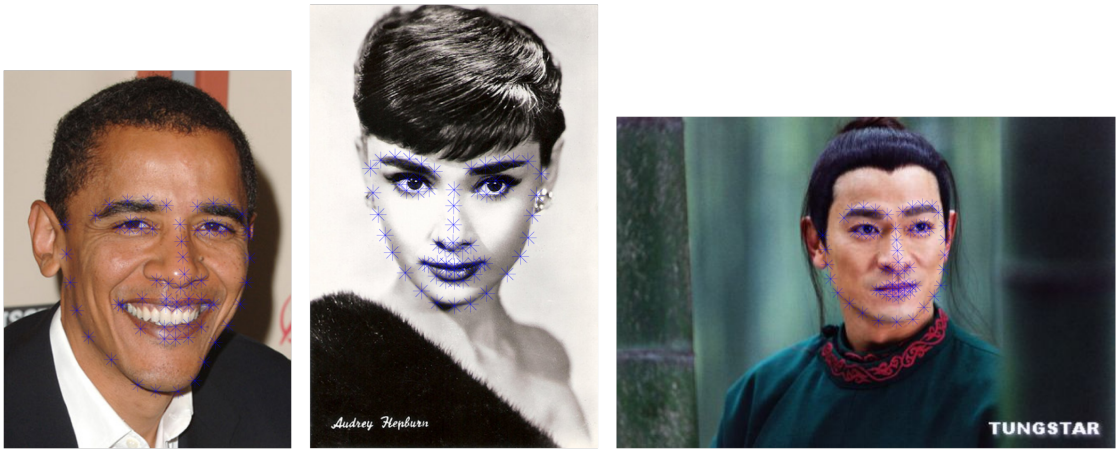

(a) (b) (c)

Figure 3.14: Three labelled human faces from LFW data.

(a) (b) (c)

Figure 3.15: The non-rigidly warped shape free patches of Figure 3.14.

with transformation Γ can be written as the 3D tensor product of one dimensional (1D) cubic B-splines,

$$\Gamma(x,y,z) = \sum_{l=0}^{3}\sum_{m=0}^{3}\sum_{n=0}^{3} B_l(u)B_m(v)B_n(w)\psi_{i+l,j+m,k+n} \tag{3.28}$$

$$\begin{aligned} i &= \lfloor x/n_x \rfloor - 1 & u &= x/d_x - \lfloor x/d_x \rfloor \\ j &= \lfloor y/n_y \rfloor - 1 & v &= y/d_y - \lfloor y/d_y \rfloor \\ k &= \lfloor z/n_z \rfloor - 1 & w &= z/d_z - \lfloor z/d_z \rfloor \end{aligned} \tag{3.29}$$

where B_l represent the lth basis function of the B-splines.

$$
\begin{aligned}
B_0(u) &= (1-u)^3/6 \\
B_1(u) &= (3u^3 - 6u^2 + 4)/6 \\
B_2(u) &= (-3u^3 + 3u^2 + 3u + 1)/6 \\
B_3(u) &= u^3/6
\end{aligned}
\tag{3.30}
$$

A least-squares fit of a B-spline deformation grid to this transformation is derived by multilevel B-spline approximation (MBA) [91]. This deformation can also be achieved by piece-wise linear warping, leading to a less smooth patch result than B-spline based FFD. Figure 3.16 compares the prostate GTV warped using piece-wise linear image warping and B-spline based FFD. Discontinuities are observed on the surface warped by linear warping (Figure 3.16a), while the FFD based warping give a much smoother surface (Figure 3.16b).

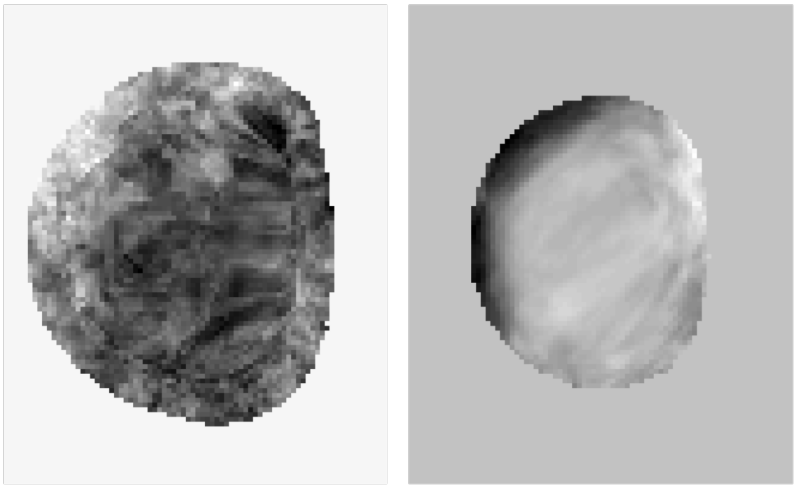

(a) (b)

Figure 3.16: (a) An AAM model constructed for prostate GTV based on piece-wise linear image warping. (b) An AAM model constructed for prostate GTV based on MBA image warping.

3.5.5 Registration Based Segmentation Applications

Registration can also be applied to fulfil segmentation based on an atlas. An anatomical atlas of the brain was first established in 1988 [92]. This is useful for distinguishing regions near landmarks and structures which have small variability. Atlas based registration methods have been successful in segmenting healthy structures by using affine or non-rigid registration to register to corresponding anatomical atlases [93, 94, 95].

There has also been work on implementing the registration methods in the segmentation of prostate [96] and bladder [97] on CT images. Promising results also have been obtained on a intra-patient segmentation of prostate cancer [96]. Costa et al. [98] claims that significant shape, size and intensity variations of GTV are difficult to capture by registration methods, but remain useful for initialisation purposes. For example pelvic bone registration provides a good initialisation point for a prostate shape model [75]. Atlas-based approaches have also been used as a pre-processing step to establish spatial constraints for more locally applied image segmentation. Prastawa et al. adopted this approach by first registering to an atlas of healthy brains in their framework for automatically segmenting brain tumours on MR image volumes [99].

3.6 Freely Deformable Models

This section covers commonly used FDMs with an emphasis on active contour, LSM, and two expansion of LSM, region based LSM and edge based LSM.

3.6.1 Active Contour

Kass et al. [21] introduced a freely deformed model called 'snake', in which the contour evolution is driven by energy forces, an internal energy to impose a smoothness constraint and an external energy to push the contour to desired features.

Let Ω be a bounded subset of R^2, the boundary is defined as $\partial\Omega$, I_0 is a given image and $C(s) = (x(s), y(s)), s \in [0,1]$ is the parameterised curve. An edge indicator (Equation (3.9)) is

used, depending on the gradient of image I_0, as a stopping criteria in the evolving of the curve $C(s)$. The energy function of a conventional snake is written as,

$$E_{snake} = \alpha \int_0^1 |C'(s)|^2 ds + \beta \int_0^1 |C''(s)| ds - \lambda \int_0^1 E_{external}(C(s)) ds \tag{3.31}$$

Here α β and λ are positive weight parameters. The first two terms in Equation 3.31 represent the internal energy of the curve spline, controlling the smoothness of the curve, while the third term is an edge indicator function (Equation (3.9)) as an external energy term that drives the curve towards the object boundary. By minimising E_{snake} in Equation (3.31), the curve $C(s)$ is located at points of the image gradient maxima $|\delta\Omega|$, which is considered as a boundary. It is easy to understand from the definition of this energy function that it has certain disadvantages, it can get stuck in a local minimum. It can however be used in semi-automatic image segmentation tasks by placing the initial contour near the object of interest. Xu et al. [71] improves this snake model by replacing external energy with GVF, resulting in a GVF snake with larger capture range.

3.6.2 Level Set Methods

Level set methods were proposed by Sethian et al. [100], in which the deformation of the 2D contour $C(t)$, with respect to time t, is embedded as the zero level set contour of a 3D Lipschitz function ϕ by $C(t) = \{(x,y) \mid \phi(x,y,z,t) = 0\}$, which is called the level set function (LSF). This implicit contour representation entitles the level set framework to be capable of solving topological changes in the contour deformation (Figure 3.18). The LSF ϕ is usually initialised ($t = 0$) as a signed distance function (SDF) as,

$$\begin{cases} \phi(x,y,z\,t=0) = -d(x,y,\,C_{Initial}),\ (x,y)\ inside\ C_{Initial} \\ \phi(x,y,z\,t=0) = \quad 0 \quad\quad\quad\quad (x,y)\ on\ C_{Initial} \\ \phi(x,y,z\,t=0) = d(x,y,\,C_{Initial}), \quad (x,y)\ outside\ C_{Initial} \end{cases} \tag{3.32}$$

where $C_{Initial}$ corresponds to the contour at time $t = 0$ and contour $C(t)$ can be obtained any time as the intersection of the $\phi(x,y,z,\,t)$ at time t and plane $z = 0$, as shown in Figure 3.17. The

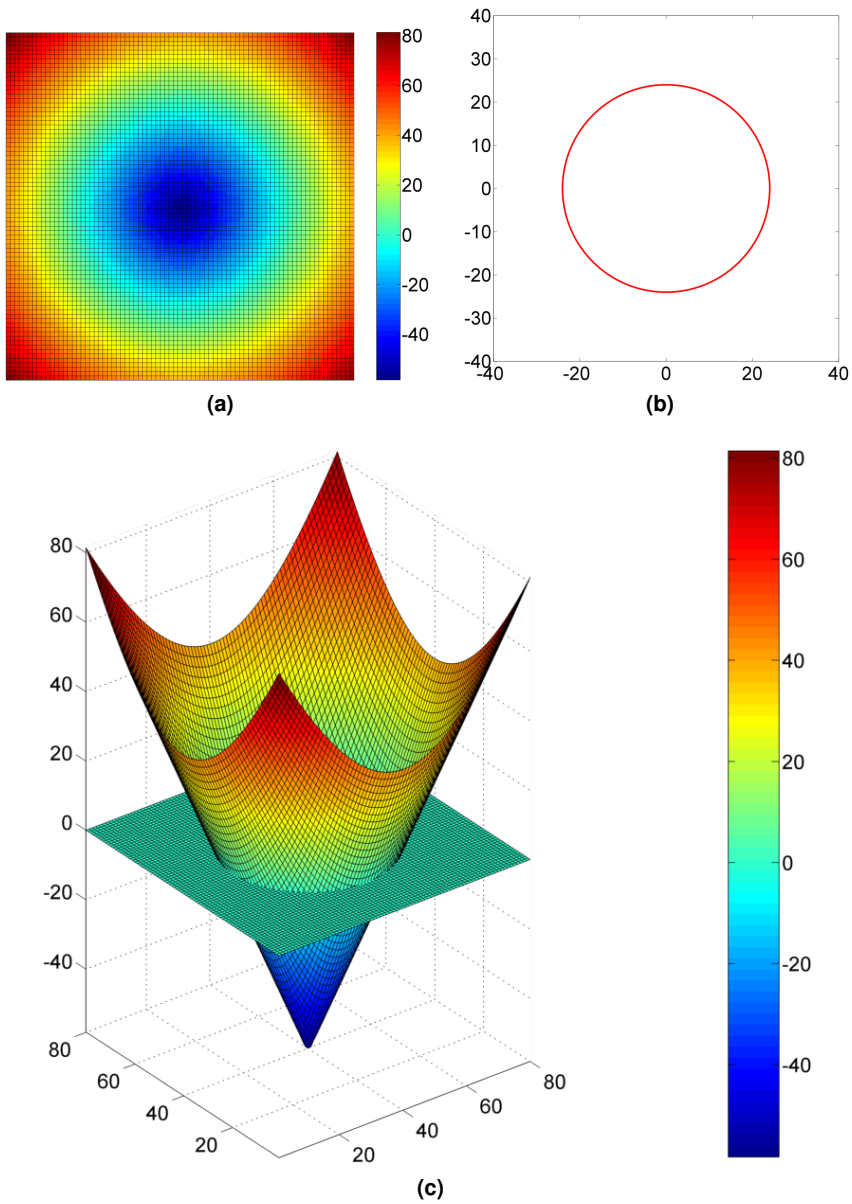

Figure 3.17: (a) The LSF initialised as a SDF. (b) The corresponding contour of (a). (c) The SDF in 3D view.

deformation of contour $C(t)$ is now interpreted as the evolution of the LSF ϕ, which amounts to solving the following partial differential equation (PDE), which derived by differentiate ϕ with respect to t,

$$\frac{d\phi}{dt} = \frac{\partial \phi}{\partial t} + F|\nabla \phi| = 0 \tag{3.33}$$

this is a general form of the level set equation, F is the speed function which evolves the contour in normal direction. It is important to note that, during the evolution, that ϕ might develop very sharp or flat shapes, which makes any further computation of the LSF highly inaccurate. A process called re-initialisation is commonly applied periodically to ensure ϕ maintain the property of a SDF whose gradient satisfies the Eikonal equation [101],

$$|\nabla\phi| = 1 \tag{3.34}$$

In Sethian's method, the motion of LSF is driven by local curvature, the stopping criteria does not depend on the gradient of the image, as in the classical active contour models. As an

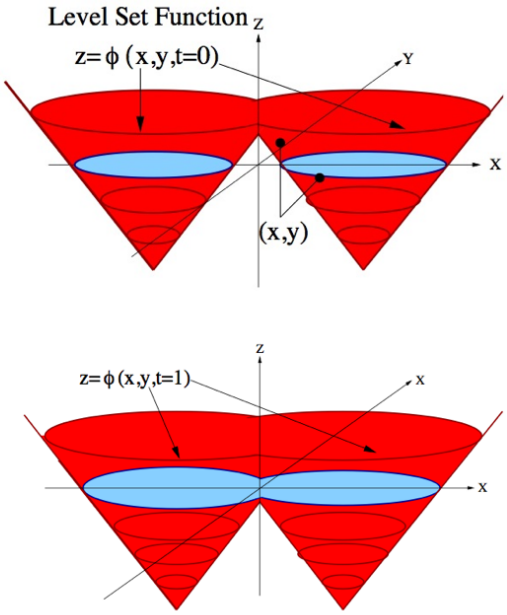

Figure 3.18: Top: red cone is the LSF at time $t = 0$, and the blue circle area is the intersection with the Z level set. Bottom: The evolving LSF at time $t = L$, the curve on the Z level set have merged together [63].

alternative, the evolution PDE of the LSF can be derived by minimising an energy function defined on the LSF. This is known as variational level set methods, which is more convenient and natural for incorporating information, when looking for a certain type of edge or contours [102]. The Chan and Vese [58] region-based model and the Chunming Li [20] edge-based model have obtained promising results in the segmentation of multi-modality medical image

data [103, 104, 105, 106].

3.7.2.1 Chan Vese model

The Chan Vese (CV) model is a classic region based active contour segmentation algorithm within the framework of the level set method. The evolution PDE of the CV model is derived by minimising an energy function based on the regional image intensity. Assuming an image I is formed by two regions of approximately constant intensity, u_0^i (inside the object) and u_0^o (outside the object). If the object being detected has an intensity of $u_0(x,y)$ and the corresponding contour is denoted as C_0. According to Chan Vese's theory, $u_0(x,y) \approx u_o^i$ within the C_0 and $u_0(x,y) \approx u_0^o$ outside the C_0, the following fitting energy function is used to drive the level set contour C ,

$$F_1(C) + F_2(C) = \int_{inside(C)} |u_0(x,y) - c_1|^2 dxdy + \int_{outside(C)} |u_0(x,y) - c_2|^2 dxdy \tag{3.35}$$

Where C is the level set contour, constants c_1 and c_2 depend on C_0 and are the average of u_0 inside and outside C respectively. It is easy to understand that this energy function is minimised if $C = C_0$, where evolution of the level set contour stops at the object boundary. Figure 3.19 illustrates all the possible cases in the position of the level set contour. In Figure 3.19a C is placed outside C_0, resulting in $F1(C) > 0$ and $F_2(C) \approx 0$. Figure 3.19b shows the case C inside C_0, resulting in $F_1(C) \approx 0$ and $F_2(C) > 0$. Figure 3.19c shows the case C is partial inside C_0, resulting in $F_1(C) > 0$ and $F_2(C) > 0$. Figure 3.19d shows the optimum case in which $C = C_0$, $F_1(C) \approx 0$ and $F_2(C) \approx 0$, the fitting energy is minimised in this case. A regularising term is added to Equation (3.35) to complete the final energy function of the CV model. The energy function of CV level set is not based on the image gradient as used in the classic snakes and active contour approaches. Kass et al. [21] claimed that the discrete gradients are bounded and then the stopping function will never hit zero, consequently, the curve might pass through weak boundaries easily. The CV model energy function is designed for the minimal partition problem based on the Mumford Shah function [107], which requires a piece-wise constant c_i. There is no doubt that, this regional based energy function has advantages as it can detect objects whose boundaries not necessarily defined by gradient. While in many practical medical segmentation

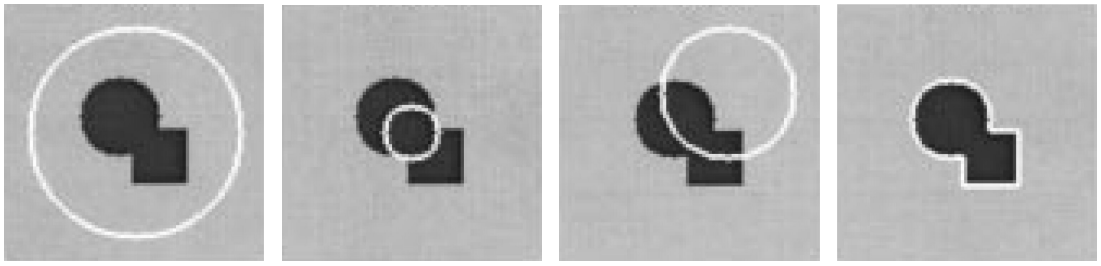

(a) (b) (c) (d)

Figure 3.19: All the possible positions of the level set contour during evolution.(a) C outside C_0, $F1(C) > 0$ and $F_2(C) \approx 0$.(b) C inside C_0, $F_1(C) \approx 0$ and $F_2(C) > 0$. (c)C is partial inside C_0, $F_1(C) > 0$ and $F_2(C) > 0$. (d) C = C_0, $F_1(C) \approx 0$ and $F_2(C) \approx 0$, the fitting energy is minimised in this case [102].

cases it is not possible to find a reliable constant c_2 for the object outside (surrounded by multiple organs), and sometimes a large variation within the ROI (high grade glioma). The CV model is therefore not used for the segmentation of glioma in this thesis, interested readers are referred to [102] for more detail.

3.7.2.2 Chunming Li Model

The Chunming Li (CL) LSM model is a typical edge/gradient based snake under the level set framework. As mentioned earlier, in traditional level set methods periodic re-initialisation of the LSF to a SDF is required to avoid sharp corners or flat shapes during evolution. In the CL model, this process can be eliminated by incorporating a penalty term that characterises the difference between the LSF and Equation (3.34) defined by [20],

$$E_{SDF}(\phi) = \int_{\Omega} \frac{1}{2}(|\nabla\phi| - 1)^2 dxdy \tag{3.36}$$

Since a SDF must satisfy the desirable property of Equation (3.34) then when minimising the energy function above, the term Equation (3.36) keeps the LSF ϕ close to a SDF. In addition to the term in Equation (3.36) the energy function of the CL model consists of other terms pushing the contour to a place with specific features similar to the region information used in the CV LSM model or contour shape-prior information used by Vemuri et al. [108]. Internal energy drives the zero level set to a target contour for a LSF $\phi(x,y)$ which is calculated in the

CL model as [20],

$$E_{Internal}(\phi) = \lambda L_g(\phi) + \nu A_g(\phi) \tag{3.37}$$

$$L_g(\phi) = -\int_\Omega f\delta(\phi)|\nabla\phi|dxdy \tag{3.38}$$

$$A_g(\phi) = -\int_\Omega fH(-\phi)|\nabla\phi|dxdy \tag{3.39}$$

where f is edge indicator function in Equation 3.10, δ is the Dirac function and H is the Heaviside function. The term $L_g(\phi)$ and its constant weight λ perform as the regularising term to keep the contour tight, and the term $A_g(\phi)$ is proposed to expand or shrink the contour depending on the sign of constant ν. Substituting Equation (3.38) and Equation (3.39) into Equation (3.37) and add in Equation 3.36, we obtain the total energy function for the level set evolution as,

$$\begin{aligned} E(\phi) = \mu\int_\Omega \frac{1}{2}(|\nabla\phi|-1)^2 dxdy - \lambda\int_\Omega f\delta(\phi)|\nabla\phi|dxdy \\ -\nu\int_\Omega fH(-\phi)|\nabla\phi|dxdy \end{aligned} \tag{3.40}$$

A gradient flow can be derived from equation 3.40 by taking the Gateaux derivative [101] as follows,

$$\frac{\partial\phi}{\partial t} = \mu[\triangle\phi - div(\frac{\nabla\phi}{|\nabla\phi|})] - \lambda\delta(\phi)div(f\frac{\nabla\phi}{|\nabla\phi|}) - \nu f\delta(\phi) \tag{3.41}$$

This gradient flow is the evolution equation of the level set function in the proposed method [20].

3.6.3 Summary

In this section, freely deformable models including snake, active contours, and level set methods have been discussed. These algorithms have drawn intensive interest in the semi-automatic and automatic segmentation of medical images [57, 109]. Level set and active contour based approaches both have significant advantages and potential for automatic brain tumour segmentation [110, 111]. Without shape prior information incorporated they look for edges/boundaries based on gradient or regional information, driven by certain energy function. On one hand, it is easy to understand that they require good soft tissue contrast and resolution level from the

modality processed to avoid propagation across weak or missing boundaries. On the other hand shape free deformation granted the model being able to segment target volume with large shape variation, for example brain tumours. In Chapter 4, a case-wise automatic delineation algorithm for brain glioma on MRI based on CL model level set method is proposed and implemented to patient data as a pilot study.

3.7 Shape Constrained Deformable Model

Shape constrained deformable models refer here to statistical shape models (SSM) that contain shape information about the expected shape and corresponding appearance of the structure of interest. The key difference from FDMs is, SCDMs gather shape information as a prior from a sufficiently large shape set, which is called a training archive. With inherent shape prior information incorporated, SSMs are more stable than FDMs against local image artefacts and missing boundaries in low signal to noise ratio (SNR) image modalities, and have achieved promising results in segmentation application of industrial objects and human healthy organs in medical imaging. However, SSM is prone to fail in cases where the GTVs is irregular [98]. The following sections briefly review SSMs, focusing on the training and employing the ASM and AAM methods.

3.7.1 Active Shape Models

The straight-forward way to gather shape information is to summarise the training shapes by a statistical mean and shape variations [26]. Shape invariant features can be eliminated from the training archive by registering all of the shapes. 2D SSM have been in use since the early 1990s, when Cootes et al. introduced ASM [26] and AAM [59] for face recognition.The point distribution model (PDM) [73] uses a set of landmarks to represent shapes, which is a standard practice in computer vision, as shown in Figure 3.20. The term 'landmark' refers to a significant point between several medical images which are identifiable and useful in the analysis of shape changes [113]. Cootes et al. manually selects a range of points around object boundaries as landmarks. The red landmarks in Figure 3.20 includes anatomical landmarks (tip of fingers) and

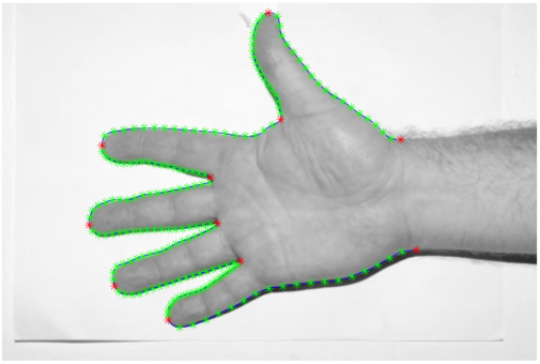

Figure 3.20: The PDM of 191 landmarks for hands representation, the image and contour data is extracted from [112].

mathematical landmarks (curvature maxima), the green landmarks are pseudo landmarks which evenly interpolated between the first two types of landmarks. However, this manual approach is considerably more difficult in 3D or higher dimensional cases. 3D model applications have increased in recent years because of breakthroughs in the automatic definition of surface shape correspondence (reviewed in Section 3.5.2). After alignment and correspondence definition, an orthogonal linear transformation called principal component analysis (PCA) [114] is applied to capture useful shape variation of the training shapes with finite feature dimensions. For a surface matrix X of size m by n, whose rows are shape vectors stacked by landmark vertices and n columns are the number of training shapes, PCA fits an N dimensional ellipsoid to the matrix X, where each axis of the ellipsoid represents a principal component. Each principal component corresponds to a certain shape deformation and the length of each axis depends on the contribution of the corresponding deformation within the shape archive. Firstly, the statistical mean $\bar{X}$ is subtracted from matrix X. The covariance matrix Σ of the data is then computed, from which the eigenvalues and corresponding eigenvectors are derived using SVD. From this point, any shapes from the training archive can then be approximated using the eigenvalues and eigenvectors as [26],

$$X = \bar{X} + P_s b_s \tag{3.42}$$

where P_s is the matrix of principal components, also known as shape variation vectors and b_s is the matrix of the corresponding contributions, also known as shape model parameters. The

number of principal components t required to fully capture the shape variation of the training archive is chosen to describe a certain percentage f_v of variance of the whole training set, usually in the range from 95% to 98% [27, 1]. The desired number of principal components is given by the smallest t for which,

$$\sum_{i=1}^{t} \lambda_i \geq f_v \sum_{i=1}^{n} \lambda_i \tag{3.43}$$

Figure 3.21 shows the deformation by varying the largest principal component up to three standard deviations. As introduced in Section 3.4.3, local appearance information is gathered

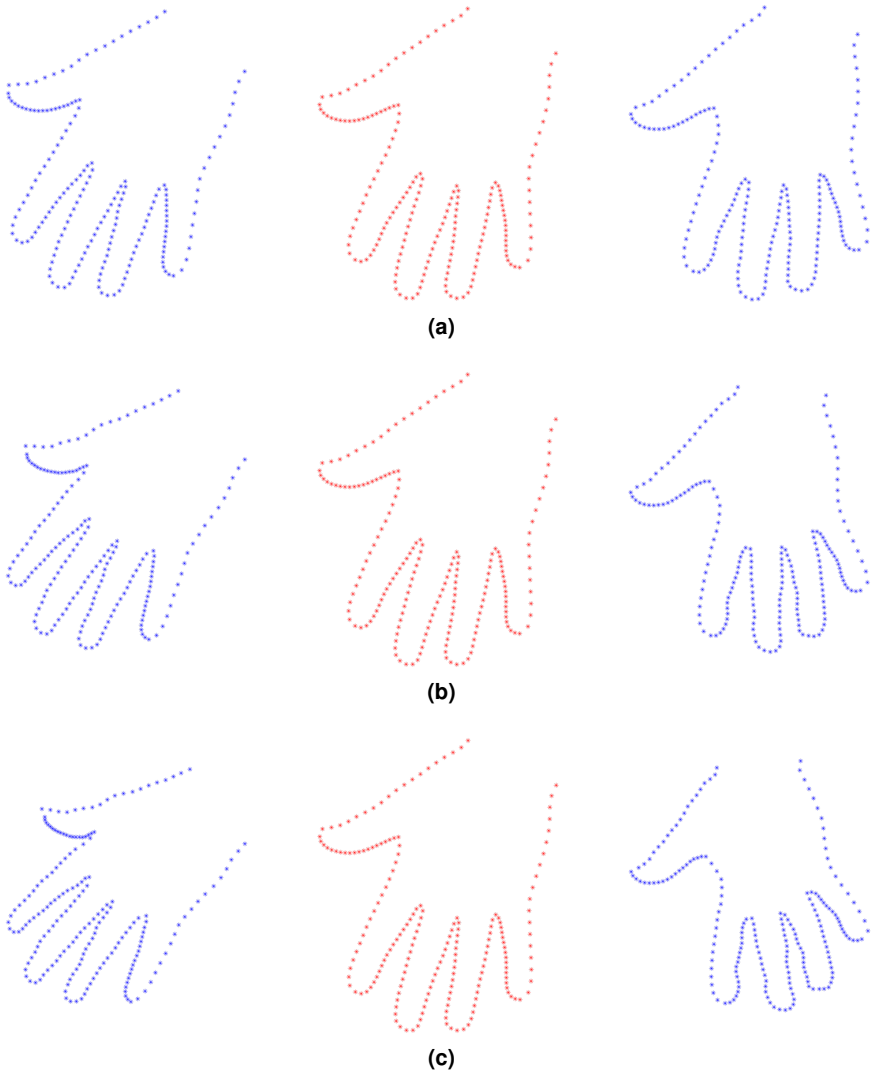

Figure 3.21: Shape variation of the hand ASM. Red: the mean shape of the hand ASM, blue: the deformed hand shape using Equation (3.42). (a) One standard deviation, (b) two standard deviations, (c) three standard deviations.

as the profiles perpendicular to the contour/surface through inside and outside of the object with predefined length (normally 3-5 pixel both sides), resulting in an appearance profile g. From Equation (3.12), the MD between the profile of a potential displacement of L_i as an observation g_i and the distribution from trained model for L_i is calculated by,

$$f_i = \sqrt{(g_i - \bar{g}_i)\Sigma^{-1}(g_i - \bar{g}_i)} \tag{3.44}$$

where Σ_i^{-1} is the inverse covariance matrix of the modelled appearance profiles for landmark L_i, and $\bar{g}_i$ is the mean vector of the modelled appearance profiles for landmark L_i. Shapes are fitted in an iterative manner, landmark movement starts from the mean shape during the optimisation process. The landmarks move along the direction perpendicular to the contour/surface to the location that matches best with the model profiles (see Section 3.4.3). One iteration of the conventional ASM shape fitting is shown in Figure 3.22. The shaded object represents the true position and the dotted contour represents the shape model; At the start, the shape model is initialised at the lower left of the true position. Local texture information of all landmarks are evaluated along the direction perpendicular to the contour. The best location for each landmark is the position with the smallest MD shown as a small circle in the middle. Finally, landmarks are moved to the new best location reducing the cost function and bringing the contour closer to the true position [1]. From Equation (3.42) the shape model parameters b_s can calculated

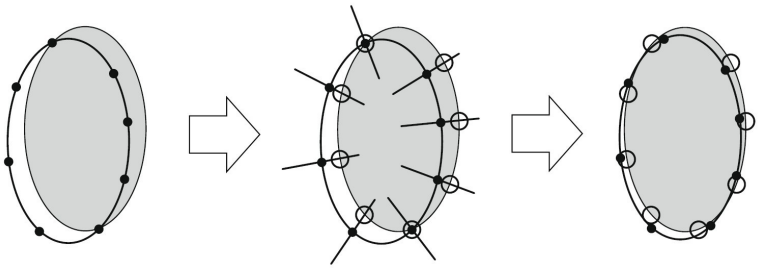

Figure 3.22: One iteration of ASM searching [1].

after each iteration by,

$$b = P_s^T(X - \bar{X}) \tag{3.45}$$

The shape model parameters control the GTV shape within an expected space region, normally up to three deviations [26]. These shape variation vectors and shape model parameters are applied periodically during the ASM segmentation evolution, to restrain the shape deformed with three standard deviations of b_s from the training archive.

3.7.2 Active Appearance Models

AAM is another powerful approach related to the ASM algorithm. They are both statistical models containing the range of shape variations of an object learnt from a training archive of ground truth shapes, usually represented by landmarks. In addition to the ASM training the image appearance is combined with the shape model to generate the appearance model in AAM. Namely, the AAM approach manipulates a combined model of shape and appearance, which basically represents both shape variation and texture of the object interior. In summary, ASM seeks to match the model of landmarks to a new image, constrained by the valid range of shape variation. While AAM match both the position of model landmarks and the appearance of the object defined by the landmarks.

An important process called appearance alignment is required to build an AAM. Training shapes including the interior appearance are warped to the mean shape of the AAM bringing in voxel-wise correspondence to remove the spurious appearance variation brought by shape difference [59]. This process is also known as appearance normalisation and is normally done by a piece-wise linear warping or B-spline based FFD warping, which creates a shape free appearance patch as shown in Figure 3.14 and Figure 3.15. Similar to the ASM approach, PCA can be used to capture the shape and the appearance variation and the AAM can have appearance model parameters c controlling the shape and also appearance as,

$$X = \bar{X} + P_s c \tag{3.46}$$

and,

$$g = \bar{g} + P_g c \tag{3.47}$$

where g is the synthesised appearance of the AAM, $\bar{g}$ is the mean appearance of AAM, P_s and P_g are matrices describing the model shape and appearance variation respectively. Figure 3.23 shows the effect by varying the shape and appearance model parameters of the largest principal component up to three standard deviations. In addition to these modes we need to account for basic operations as translation, scaling and rotation etc. Additional parameter vectors t and u, resulting in a combined parameter vector U as,

$$U = [c^T, t^T, s^T] \tag{3.48}$$

where t is the translation parameters, s is scaling parameters.

This differs from ASM model in that instead of searching for an update of each landmark, AAM seeks to minimise the appearance difference between a new image and the synthesised appearance by AAM, as demonstrated in Figure 3.24. Initially, the model (contour with landmarks) is located at the lower left of the true position (solid gray object). The texture beneath the model is sampled and compared to the region-based appearance model. The corresponding residuals are shown in the center image and suggest a move of the model to the upper right, this information is learned during training and encoded in matrix R. The resulting parameter update will drive the model closer to the correct location [1]. The synthesised image appearance is acquired from Equation (3.47) as g_m and the appearance beneath the model fit is sampled and normalised, resulting in g_s. The residual r of current AAM fit is calculated as,

$$r(U) = g_s - g_m \tag{3.49}$$

and hence, the error of appearance difference can be obtained,

$$E = r^T r \tag{3.50}$$

where T denotes the transpose. The fundamental of the AAM fitting algorithm is to find the relationship between appearance residual $r(U)$ and the model parameter update δU, which here in the theory of AAM, is considered as constant over the entire fitting process. Suppose the current error is $E(U)$, the desired model parameter update δU minimises the error $E(U + \delta U)$

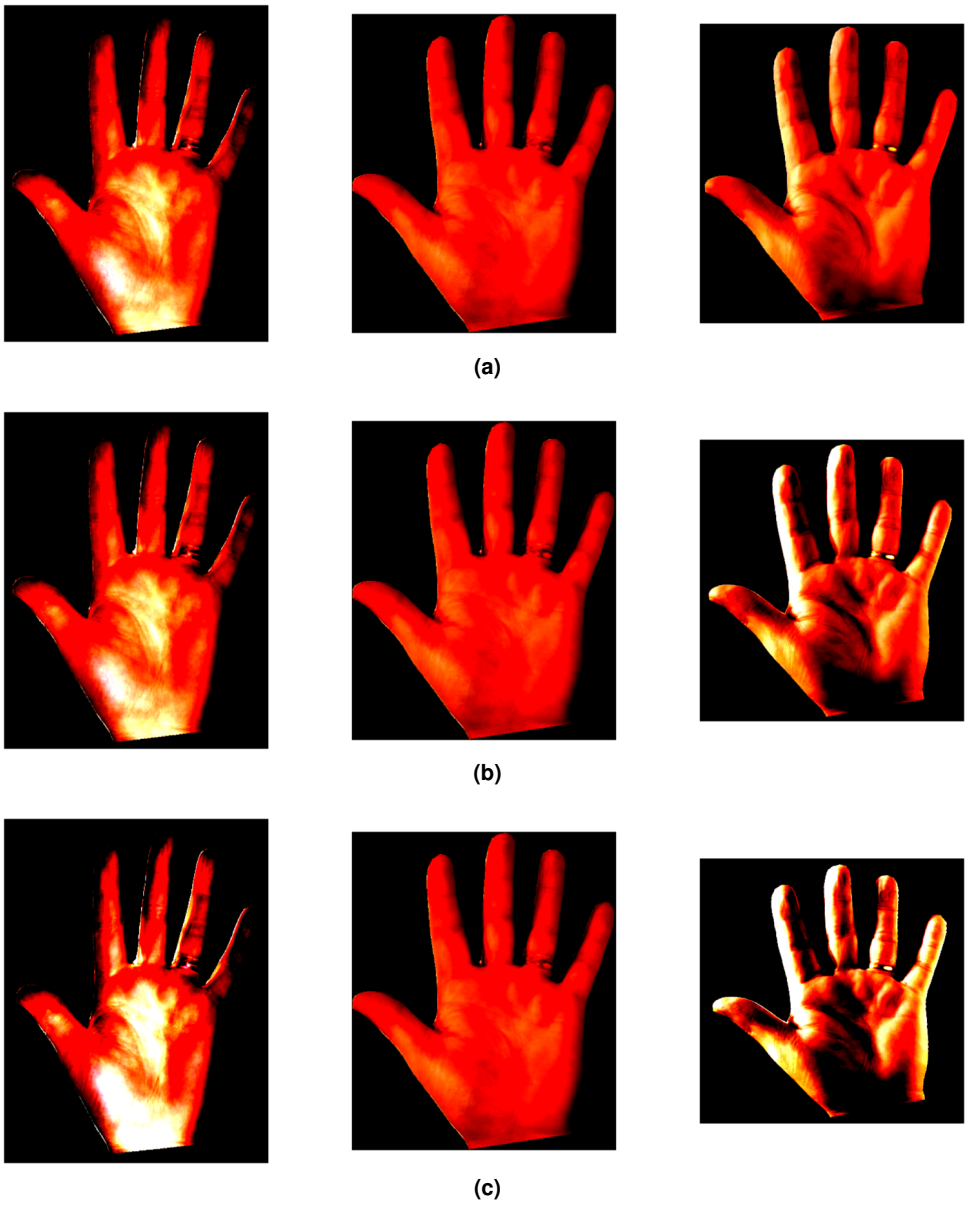

Figure 3.23: Shape and appearance variation of the hand AAM. Mid: the mean shape and appearance of the hand AAM, left and right: the deformed hand AAM using Equation (3.46) and Equation (3.47). (a) One standard deviation, (b) two standard deviations, (c) three standard deviations.

after the current iteration. Using a first order Taylor expansion to update residual $r(U+\delta U)$ and set it to zero,

$$r(U+\delta U) = r(U) + \frac{\partial r}{\partial U}\delta U = 0 \tag{3.51}$$

The RMS solution is therefore obtained as,

$$\delta U = -Rr(U), \tag{3.52}$$

where

$$R = (\frac{\delta r^T}{\delta U}\frac{\delta r}{\delta U})^{-1}\frac{\delta r^T}{\delta U} \tag{3.53}$$

which is the pseudo-inverse of $\frac{\delta r}{\delta U}$. In the first paper by Cootes et al. in 1998 [59], R was

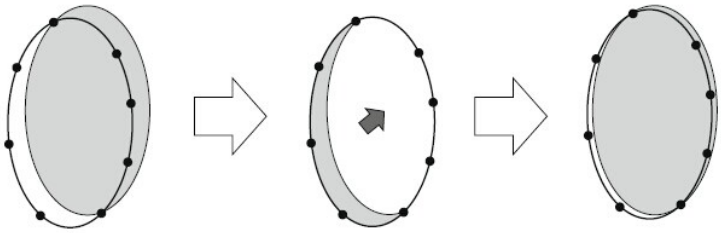

Figure 3.24: One iteration of an AAM search [1].

computed using multivariate linear regression on all the training data, and in 2001 [27], linear regression was replaced by numerical differentiation, which does not require all the training data loaded at once in model training. This makes it very useful for confronting a considerably large image archive.

3.7.3 Comparing Active Shape and Active Appearance Model

In this section, two highly related algorithms were reviewed. ASM and AAM both represent shape using a set of landmarks, learning the valid ranges of shape variation (ASM) and appearance variation (AAM) from a training set of labelled images. ASM searches along profiles at current location so that a larger capture range than the AAM is expected [115]. However ASMs only use data around the model points and the grey-level information available within an object is discarded. Thus ASMs may be less reliable than AAMs which take advantage of the whole

image appearance under current location [115].

3.7.4 Summary

SCDMs including ASM and AAM were addressed in earlier sections [115]. In this section, relative applications based on SCDMs were investigated for the segmentation of prostate and prostate GTV. Applications of SCDMs varies in many ways, throughout the training and segmentation scheme.

A SCDM trained on an archive containing images of multiple scans from a single patient is called an intra-patient SCDM [116]; based on scans from multiple patients is an inter-patient SCDM [117]; Jeong et al. [118] used a training archive of multiple scans of multiple patients, which is known as a combined SCDM. An inter-patient scheme is clinically more useful and more challenging because it manipulates an archive containing much larger variation both in the GTV shape and appearance. A SCDM expected to automatically delineate the GTV for radiotherapy planning must be based on an inter-patient study, while the intra-patient SCDM is more likely to be applied in RT for a treatment planning update. In this thesis, the emphasis is on the inter-patient SCDM, because an inter-patient SCDM can be easily implemented to the intra-patient data but not vice versa.

AAM are mainly built on MRI images which provides detailed soft tissue information for appearance analysis. Broadhurst et al. [119] modelled the interior and exterior of the bladder, prostate, and rectum, within 1 cm of each boundary, with Gaussian weight defining six regions of interest (ROI). Quantile histograms [120] were used to capture appearance within the ROI, in order to use Euclidean methods such as PCA. Appearance was characterised using histograms of the entire organ interior and exterior regions in the work of Chen et al. [121]. Stough et al.[116] replaced the single Gaussian model of intensity with a number of local region-type Gaussian models, the local-clustered model capturing the exterior inhomogeneity gives a boundary partition consistent with anatomy. Rousson et al. [31] modelled the intensities of prostate interior, bladder interior and the rest exterior. Costa et al. [98] took only a small region of the prostate interior with a mean gray level way, and used it to move landmarks in the normal direction of the surface. In Chapter 5 and Chapter 6, SCDMs are further discussed and

employed in the delineation of prostate cancer GTV of inter-patient data sets.

3.8 Summary

This chapter covered a series of low level segmentation methods, which individually may not capable of segmenting complicated medical images. However, they can be applied as pre-processing to increase the robustness and accuracy of deformable model applications. Registration based methods were reviewed with an emphasis on point set registration and B-spline based image warping. The methodologies of SDMs are also reviewed, which were categorised into FDMs and SCDMs. The majority of the FDMs and SCDMs applications are targeting healthy organs, which have more natural and consistent shape and appearance deformation. There are fewer reliable and efficient applications focusing on target volume identification for radiotherapy. In the works presented in later chapters, FDMs and SCDMs are employed in a fully automatic GTV delineation applications for brain gliomas and prostate cancer.

Chapter 4

Automatic Identification of Brain Glioma

This chapter presents an automatic contouring system using edge based LSM for identifying higher grade (III and IV) glioma on T2 weighted MRI [1]. The series of low level image segmentation methodologies reviewed in Section 3.3 are cascaded to form a case-wise fully automatic initialisation pipeline for the level set function, see Section 4.4.

4.1 Introduction

Surgical operations remains the most major and effective treatment for brain cancer patients. High grade gliomas tend to diffuse into surrounding healthy tissue at a rate associated with the tumour grade. Grade II tumours proliferate relatively slowly, however, higher-grade tumours tend to grow more rapidly. Grade IV tumours, which are particularly aggressive, form new vascularisation to support growth around a necrotic core. Figure 2.8 shows the post-surgical CT and the pre-surgical MRI for the Grade II, III IV brain tumours used in the study. The CT images also show the GTV contour (inner red contour) and the PTV (outer red contour), which takes account of variations in size, shape and position relative to the treatment beams [10, 11]. Complete tumour resection is made difficult by the spread within the brain and is usually followed by radiotherapy or chemotherapy to ensure that any remaining cancerous

1. This chapter is based on the following publications:
i) Cheng K, Feng Y, Steel R, McLaren DB, Erridge SC, McLaughlin S, WH Nailon. Level set identification of radiotherapy target volumes on magnetic resonance images. In Proc of 5th of International Conference on Advances in Medical Signal and Information Processing (MEDSIP). Liverpool, UK, 5th-7th July 2012.
ii) Cheng K, Montgomery D, Feng Y, Steel R, Liao H, McLaren DB, Erridge SC, McLaughlin S, Nailon WH. Identifying Radiotherapy Target Volumes in Brain Cancer by Image Analysis. Healthcare Technology Letters, Volume 2, Issue 5, October 2015, p. 123 âĂŞ 128

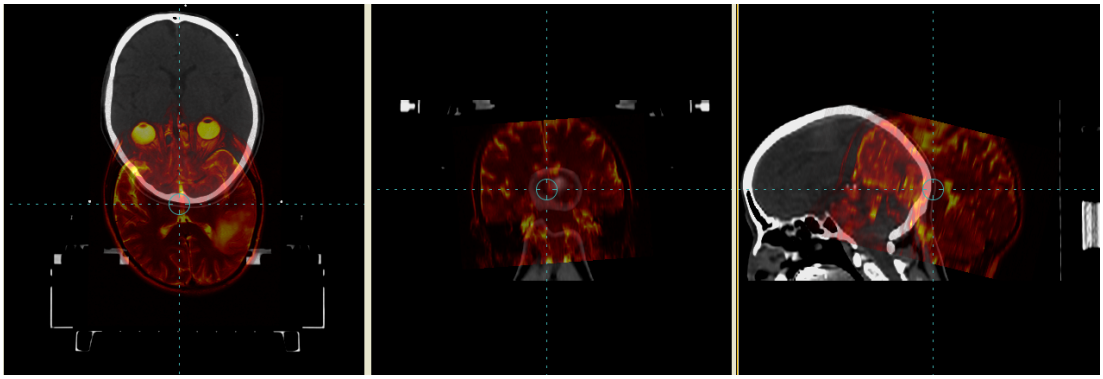

Figure 4.1: Left: Axial CT and corresponding MR image (red) illustrating the significant translation in the anterior-posterior and right-left directions required to align the images. The rectangular immobilisation device is visible beneath the images. Middle and Right: Coronal and sagittal CT and corresponding MR image (red) illustrating the significant rotation required to align the images.

tissue is treated. The effective delivery of radiotherapy relies on the accurate registration of the pre-surgical MR with the post-surgical CT image data. CT image data is universally used in radiotherapy because it provides electron density information that is necessary for calculating dose. However, defining the post-surgical volume that will receive radiation is made challenging by the fact that the CT images contains a void where the tumour has been resected. They also display poor soft tissue contrast compared to the pre-surgical MR images used to determine the resection volume. This problem is often compounded by the use of a diagnostic (concave) couch-top for the acquisition of the pre-surgical MR image data and a radiotherapy (flat) couch-top, including a full head and neck immobilisation device, for the post-surgical CT. The result is that a significant geometric adjustment is required to achieve alignment. Figure 4.1 shows an example of the adjustments, which have to be made to the MR (red) images in the axial, coronal and sagittal planes to align with the reference CT images. Fully- and semi-automatic image segmentation would therefore be of considerable benefit in the delineation of the GTV and OAR on multi-modality image volumes.

4.2 Previous and Related Work

The automatic segmentation of intra-cranial structures on MR image volumes has received considerable attention in recent years due to the pressing need for a reliable clinical solution to this problem [122, 123, 124]. However, many of the existing segmentation tools are designed to operate on image volumes that display natural, or healthy, anatomical topology. One commonly used method for segmenting normal intra-cranial MR image structures is to register to an anatomical atlas that contains information on the general shape and form of the structures of interest. By projecting the MR structures available from the atlas onto the MR volume under investigation, segmentation is performed [125, 126]. Such tools are ineffective in the segmentation of brain tumours where the intensity statistics of the tumour and healthy tissue overlap and oedema results in a lack of boundary clarity [127].

Other researchers have used voxel-based methods for brain tumour segmentation that allow clinicians to continuously adjust the parameters of the segmentation process. Birbeck et al. demonstrated using an interactive 2D graph cut method, which incorporates a 3D common energy function computed over several modalities, that the proposed semi-automatic tool improves segmentation time and inter- and intra-repeatability when compared with conventional manual segmentation [127]. Corso et al. [128] also used the concept of graph cuts and combined it with class models to explicitly represent different heterogeneous processes in the brain. In their work they modelled four classes of data: outside of head; brain matter; tumour and oedema. The tumour class was further divided into: necrotic; active; tumour infiltration/non-enhancing tumour. The majority of cases were segmented with accuracies near 70%, which the authors are improving by using a global context model of normal brain anatomy and brain tumour. Subbanna et al. [129] use a fully automated hierarchical probabilistic framework based on multi-window Gabor filters and an adapted Markov random field. In the first stage, a customised Gabor decomposition is developed, based on the combined-space characteristics of the two classes (tumour and non-tumour). A Bayesian framework provides a texture-based segmentation of tumours whose boundaries are refined through a modified MRF framework.

Zhu et al. [111] formulated the tumour boundary detection problem as an optimisation process, which minimised the energy function of an active contour model. The main advantage of the

approach is that it requires less computational time than standard active contour approaches because of the inherent parallel properties of the Hopfield neural network used [111]. Aloui and Naceur used a 3D level set approach to delineate brain tumours while not comparing the result with a ground truth segmentation [130]. Schmidt et al. [131] demonstrated that significant improvement in brain tumour segmentation is possible when using four different alignment-based features .

Here we present the preliminary findings of an approach, using limited prior information, for the segmentation of the significant tumour volume on the MR images of five brain cancer patients (Grade II, III and IV). As discussed earlier in Section 3.6.2, region based CV model requires constants c_1 for object and c_2 background in Equation (3.35), neither of them is able to be defined in this case. The boundaries of the lesions caused by higher grade glioma is reported to be traceable on T2 weighted MRI [38]. Consequently, edge based CL LSM model is implemented here for the LSF evolution. The boundary leakage problem shared by most of the edge based methods is resolved by filtering the image by an anisotropic enhanced diffusion filter, which is able to remove image noise while preserving edges. A set of MRI images from 5 brain glioma cancer patients were used as test data. The detailed description of data set is given in Section 4.3. The performance of this proposed algorithm were evaluated by Dice coefficient (DSC) comparing with ground truth clinical contours and evaluated by a doctor, which is covered in Section 4.5.

4.3 Data Set Definition

4.3.1 Image Acquisition

T2 weighted MRI scans were used in this study, from 5 patients treated at the ECC (Grade II two cases, Grade III one case, Grade IV two cases). Each image stack contained 34 to 44 MRI images of which between 6 to 14 slices were contoured by an experienced clinician, which was used as the ground truth for evaluation of the study. All MR images were acquired on a Siemens Symphony 1.5 Tesla scanner (Siemens, Munich, Germany) at 5 mm slice thickness and a 12-bit grey-level range. The size of each slice was $512 * 512$, a sub-image of size $251 * 209$ region

was sufficiently large to contain the whole human skull, and was therefore cut off the original image by using the skull boundary as landmarks from each image. Figure 4.2 demonstrates 9 sub-images from three patients (each row), in the superior (first column), mid (second column) and inferior (third column) range of glioma volume. Ground truth GTVs are also available on each sub-image.

4.3.2 Ground Truth GTV Contour

Contouring was performed by the experienced radiation oncologist (SE) using the Varian Eclipse^{TM} (v6.5) treatment planning system (Varian Medical Systems, Inc. Palo Alto, CA, USA). In order to reduce the variability the GTV contouring process strictly follows the ECC radiotherapy protocol for CNS cancer. Prior to radiotherapy each patient received a CT scan, which was rigidly registered to a pre-surgical MR scan using the Mirada Medical Systems platform (Mirada Medical Ltd., Oxford, UK), to establish the optimum tumour volume. The registered MR scan was reconstructed in the same resolution and geometry as the CT scan and therefore had a slice by slice correspondence, which substantially reduce the contouring variability.

4.4 Automatic Delineation of Brain Caner GTV

This automatic contouring algorithm was applied in five stages as shown in Figure 4.3. In the first stage noise was removed from the MR images using a coherence enhanced diffusion filter with optimised rotation invariance, as shown in Figure 4.4a. This was chosen because of its ability to preserve edge information [132], which is an essential feature of the edge based level set approach. In the second stage the a posteriori tumour intensity was used to set threshold levels from which a binary image was constructed containing the tumour as well as other unaffected homogeneous regions on the image, as shown in Figure 4.4b. A morphological opening kernel was applied to the binary image to remove non cancerous regions whilst it preserved the integrity of the significant tumour region. Canny edge detection was applied to extract the tumour edge contour and multiple contours were observed in Figure 4.4c. A

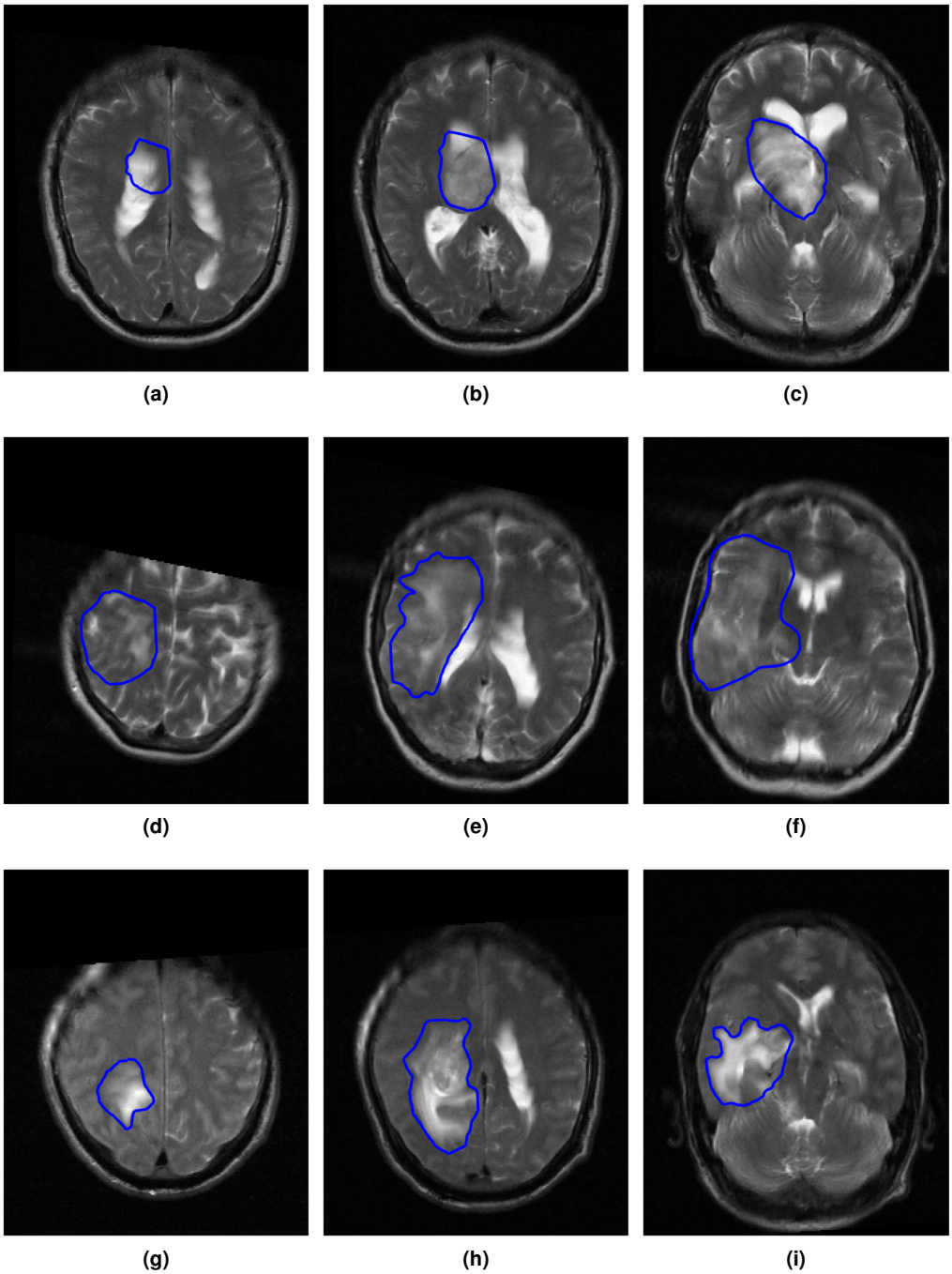

Figure 4.2: Sub-images of size $251 * 209$ were cut off the original image by using the skull boundary as landmarks from each image. 6 sub-images from three patient, (a)-(c), Grade II glioma, (d)-(f), Grade III glioma and (g)-(i) grade IV giloma. Figures listed on each column are taken from the inferior ((a),(d) and (g)), middle ((b),(e), and (h)), superior ((c),(f) and (i)) of the tumour volume. Blue contours are the clinical GTV delineated by a doctor, which are the ground truth contour for evaluation of algorithm performance.

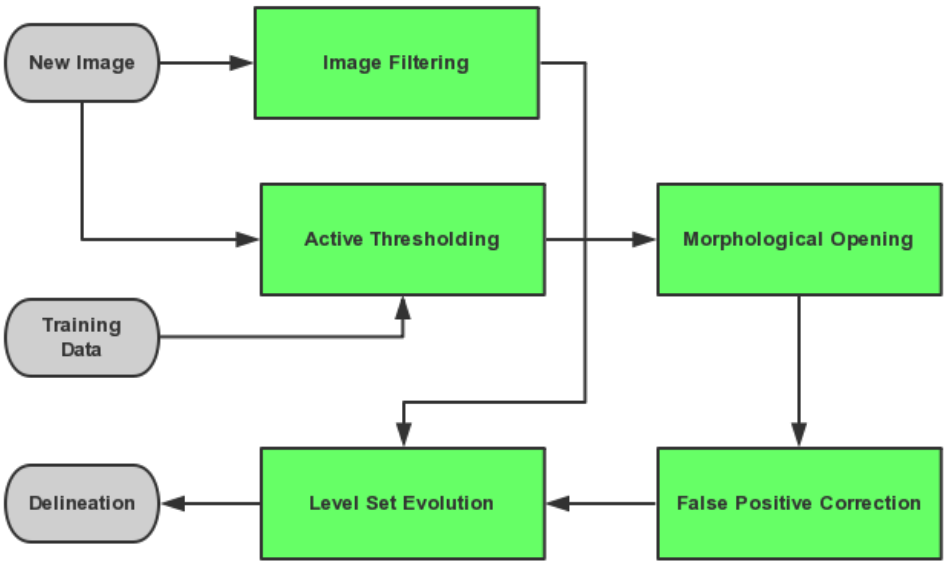

Figure 4.3: Work flow of glioma automatic identification.

initialisation correction method based on tumour centroid was applied to removed the false tumour contours. The green contour in Figure 4.4d was used to initialise the signed distance function for the evolution of the level set contour [20, 133]. Figure 4.4e shows the converged level set contour for the image. Figure 4.4f compares the converged contour with the ground truth.

4.4.1 Edge Preserving Image Smoothing

The acquisition of high-quality MR image data on indisposed patients is limited by patient comfort during scanning. This results in a trade-off between resolution and signal-to-noise ratio (SNR) for acquisition of image data in a clinically acceptable time frame, however, the effect can be reduced by post-processing noise reduction techniques [134, 135, 136]. A Rician distribution most accurately models the noise in MR image data [137]. Rician noise is dependent on the local intensity of the image and may introduce a signal-, or intensity-, dependent bias that reduces image contrast [134]. This makes noise reduction and image smoothing particularly challenging. As mentioned earlier, discrete gradients are bounded and as a result the level set propagating speed based gradient flow will then never reach zero and

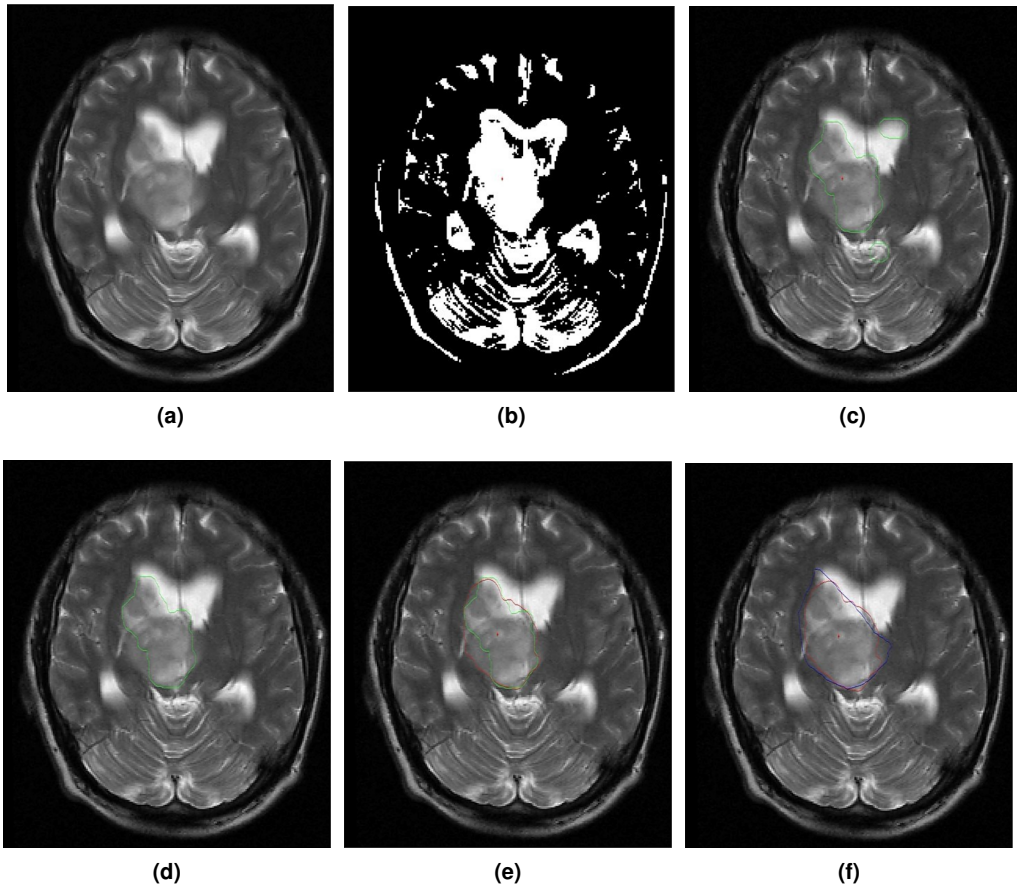

Figure 4.4: Work flow of the automatic delineation of brain caner GTV. (a): the smoothed image by coherence enhanced diffusion filter. (b) Binary image generated by active thresholding method. (c) Initial contours generated after morphological opening and canny edge detection. (d) Corrected initial contour with centroid constraint. (e) Red contour is the converged level set contour; green contour is the initial contour. (f) Blue contour is the ground truth and the red contour is the converged level set contour.

the curve will pass through weak boundaries eventually. It is therefore necessary to smooth the image while preserving and enhance useful edge information to the maximum extent. The level set approach used in this work required conspicuous edge information because it uses gradient flow to evolve the image contours [20]. To remove noise, smooth small gaps in lines and curves, and to prevent boundary leakage at points of weak gradient, an anisotropic diffusion filter was used [132]. The advantage of this filter over Gaussian smoothing is that edges are better preserved whilst smoothing is limited. The significance of this for our approach is shown in Figure 4.5, which shows the difference between a Gaussian (left) and coherence enhanced diffusion filtered image and the resulting leakage using the level set approach described in

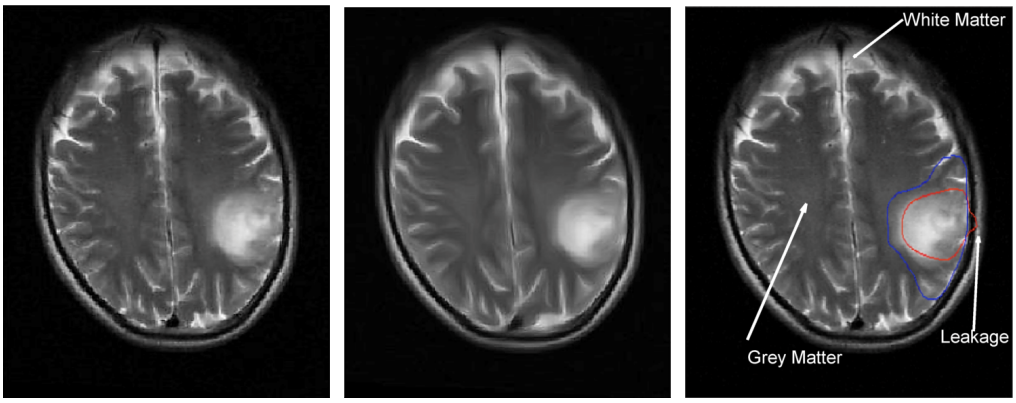

Figure 4.5: (a) Result of smoothing the MR image data using a Gaussian filter. (b) Result of smoothing using a coherence enhanced diffusion filter. (c) The level set contour obtained when the Gaussian smoothed (a) was used as input (red contour: evolving level set contour, blue contour: ground truth GTV).

Section 3.6.2.

Diffusion, the spread of particles or a substance throughout a medium, is described mathematically in two or more dimensions by Fick's law [138],

$$j = -C(\nabla I), \tag{4.1}$$

where j is the diffusive flux, the integral of a vector quantity, which is a measure of the rate of a substance (grey level) flowing through a small area in a small interval of time. C is the coefficient of diffusion, or diffusion tensor matrix, and ∇I is the gradient concentration within the image. Since mass is conserved in the diffusion process the transport can be described by the continuity equation,

$$\frac{\partial I}{\partial t} = -\nabla j, \tag{4.2}$$

where t is time. Substituting Equation (4.1) into Equation (4.2) gives,

$$\frac{\partial I}{\partial t} = \nabla \cdot (D\nabla I), \tag{4.3}$$

in which the gradient concentration in an image is derived from the gray level values. When the diffusion tensor D is constant, or homogeneous, over the whole image domain, the process is

termed isotropic. When it is inhomogeneous, or space-dependent, it is termed anisotropic. The use of anisotropic diffusion directs the flux based on the orientation of the interesting features of consistent (coherent) structures, which is extremely useful in MR images of the brain.
The diffusion tensor D is derived from the so-called structure tensor, which is given by,

$$J_\rho(\nabla I_\sigma) = G_\rho * (\nabla I_\sigma \nabla I_\sigma^T), \tag{4.4}$$

where G_ρ is a Gaussian with standard deviation $\rho \geq 0$ and I_σ and $I_\sigma = G_\rho * I_\sigma$ is a regularised version of I_σ obtained by convolution with G_ρ. The eigenvalues of J_ρ provide information on the contrast along the direction of the eigenvectors. These eigenvectors are the same as the eigenvectors of the diffusion tensor matrix D.
Weickaet and Scharr [132] illustrate how (4.3) can be solved numerically using schemes selected because of their simplicity. They demonstrated the limitations of these schemes in images containing rotational detail and present a modification to the coherence enhanced diffusion filter that takes account of rotation invariance. This filter, the coherence-enhanced diffusion filter with optimised rotation invariance, was used here to condition the MR images prior to level set evolution.

4.4.2 Case-wise Level Set Initialisation

This section covers the detail of the automatic initialisation pipeline for level set function. The posteriori intensity level, observed at the core of typical Grade II, III and IV tumuors, was used to establish two threshold T_L and T_H. The thresholds were used to create a binary image from which the tumour annulus was visible. A morphological kernel was used to remove small binary regions, whilst the boundary of the preliminary tumour region was preserved. Canny edge detection was applied to extract the initial tumour boundary as a set of points, which will be used to initialise the level set function.

Data Training and Active Thresholding

Figure 4.5c clearly shows three intensity groups, white/grey matter, tumour region and other low intensity tissues, which enable the position of the tumour to be estimated using thresholding. However, it is difficult to establish an intensity level that is suitable for different tumour grades and for identifying the same tumour region on different slices of the same patient. Registration to an atlas specifically for tumours may offer a solution to this, however, at the present time no such atlas exists . Here the approach adopted was to collect over 500,000 pixel intensities from the GTV identified by an experienced oncologist on MR scans of 10 brain cancer patients. From this it was noted that 93.27% of pixels were within the interval $[200, 800]$, which is shown in Figure 4.6. With this approach the initialisation was found to be more sensitive at lower thresholds, which may include more healthy tissue than higher thresholds. The left side of the histogram was estimated using a normal distribution, shown by the red line in Figure 4.6, and a lower threshold established in the range $[200, 800]$. The selection of a higher threshold was complicated by the variation of intensity with the grade of gliomas. Here an active thresholding scheme was adopted that searched every slice and determined the lower and higher threshold using an adaptive scheme based on the intensity of the potential tumour volume. After searching all slices in the MR volume and establishing the slice with the target volume as the starting slice the lower and thresholds are calculated from,

$$T_L = \mu - \sigma_s - (5 * |s - i|) \tag{4.5}$$

$$T_H = max(800 - 10 * |s - i|,\ \mu_s + 2 * \sigma_s) \tag{4.6}$$

where, s is the starting slice number, i is the current slice number, μ_s and σ_m are the mean and the standard deviation of the potential tumour region on the starting slice of a case. The term $|s - i|$ indicates the distance from the current slice to the starting slice, it can be observed on Figure 4.2h and i that, tumour region intensity are expected to be decreasing from the middle of the tumour to superior and inferior directions. The starting slice i is expected to be in the middle of the GTV, the selection process is described in the next section.

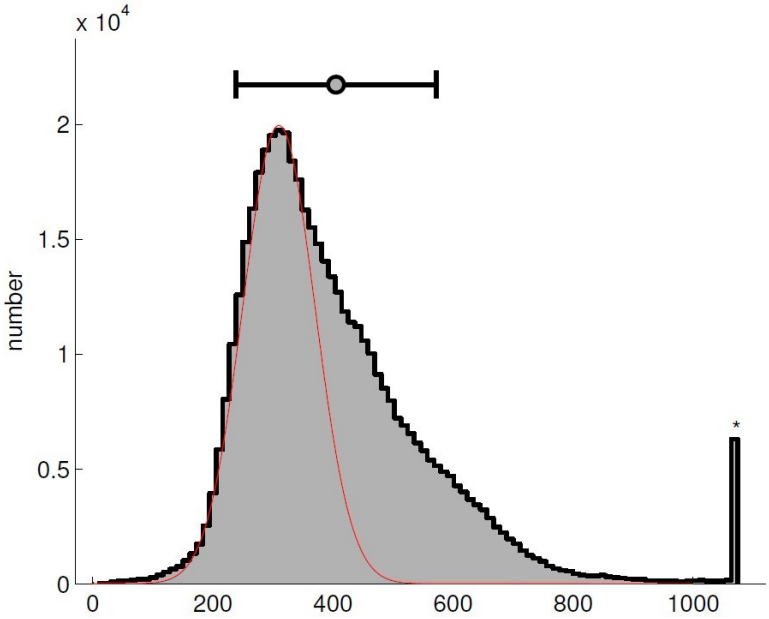

Figure 4.6: Histogram of tumour data collected from contoured GTV $(\mu = 405, \sigma = 167)$; Red line: estimated normal distribution $(\mu = 310, \sigma = 60)$ to fit the left part of tumour histogram. 80% of the overall pixels are included within the intensity range [300,600].

False Positive Contour Correction

Morphological opening might fail to remove all of the small non-tumour binary regions at the superior and inferior volume to be identified, resulting one or more false positive tumour contour, as shown in Figure 4.4c. To solve this a complete tumour identification algorithm was introduced to correct for inaccuracies in the thresholding process using the fact that the foci of the GTV is similar on two consecutive MR slices. Consequently the centroid information can be applied during application of the algorithm to remove erroneous contours as shown in Figure 4.4c. The following steps detail the use of training data and active thresholding to produce an reliable initialisation of the CL level set, which is further evolved to identify the GTV of glioma (Figure 4.7).

1. Thresholding all slices with $T_L = 300$ and $T_H = 600$, within which 80% of the tumour pixels are included, as shown in Figure 4.6.
2. A morphological opening kernel is applied to the thresholded images.
3. Within the slices which return a single object from the binary image, the slice i with the largest volume is defined as the starting slice.

4. Start level set evolution (refer to Section 3.6.2) until it converges or boundary leaking occurs, as shown in Figure 4.8. Calculate the centroid, intensity mean μ_s and standard deviation σ_s of current level set contour.

5. Using the centroid of the starting slice i to initialise level set function on slice $i-1$ This process repeated until slice $i-m$ on which initial contour area is less than 400 pixels, which is considered as initialisation failed.

6. Return to step 3 and repeat the process for slice $s+1$ to slice $s+n$.

7. Reinitialise the contour of these slices marked as contour leaking and calculate the starting slice using $T_L = 1.1 * T_L$ and the centroid P_l is recalculated by,

$$P_l = \frac{P_{l-1} + P_l + P_{l+1}}{3} \tag{4.7}$$

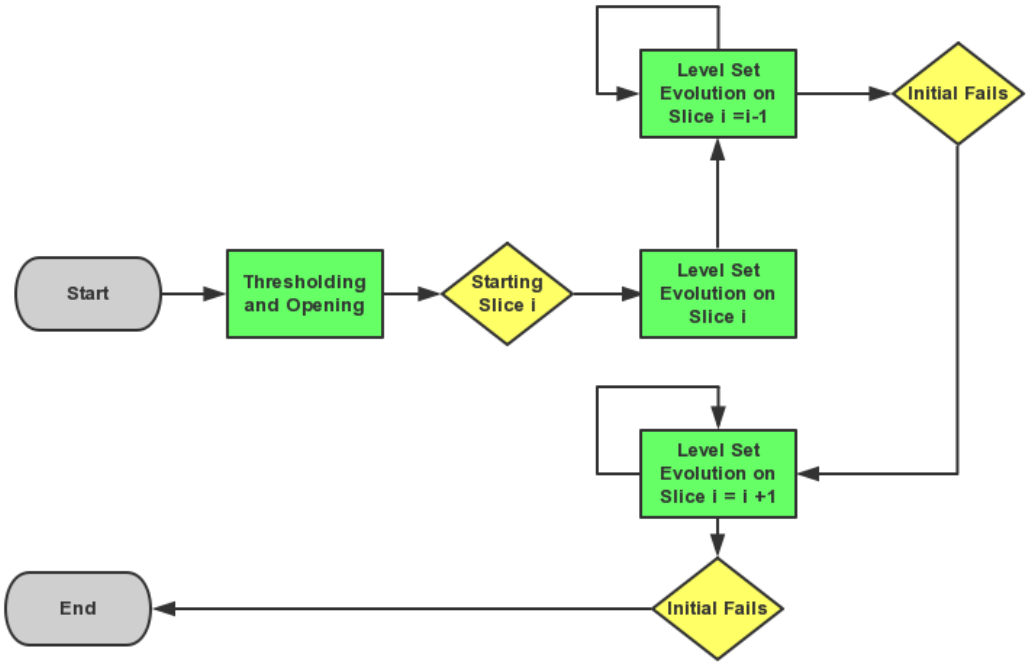

Figure 4.7: Case-wise automatic LSF initialisation.

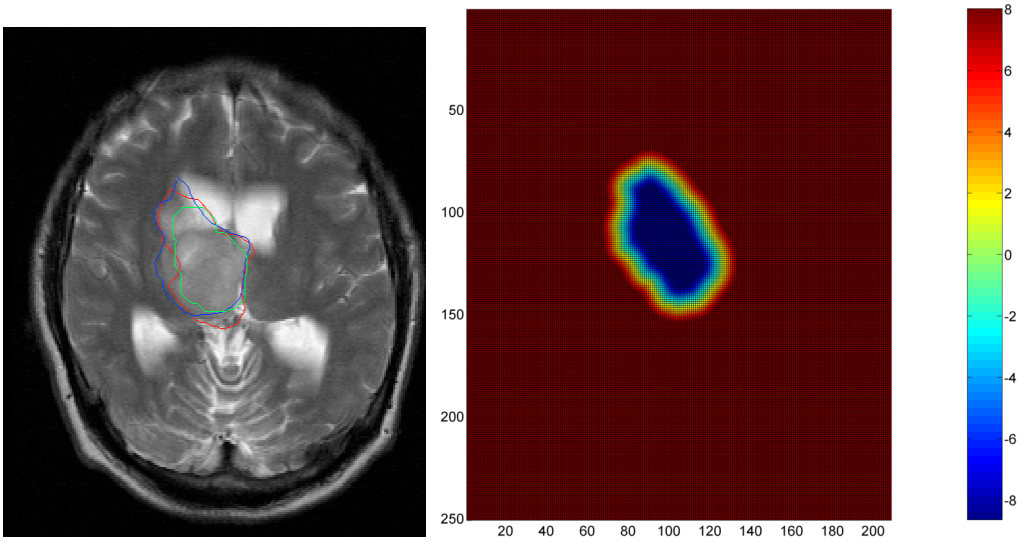

Figure 4.8: The 34th slice in case 1 is used for illustration. (a) Green: The initial contour of the level set function; Red: Converged contour generated by the Level set method proposed above; Blue: The Gross Tumor contour delineated by an experienced physician. (b) The level set function of corresponding slice.

4.5 Results and Discussion

4.5.1 Criterion: DSC and Hausdorff Distance

DSC and Hausdorff distance (HD) were used to evaluate the performance if the proposed methodology against the ground truth contours. DSC is defined using the following equation [139],

$$DSC = \frac{2|S_1 \cap S_2|}{|S_1| + |S_2|} \tag{4.8}$$

where S_1 and S_2 are the number of pixels within the image region defined by two given contours C_1 and C_2. $|S_1 \cap S_2|$ refers to the overlap of two image regions. The DSC gives a direct evaluation of the spatial overlap and similarity and ranges between 0 and 1, DSC greater than 0.7 is considered as a high level of similarity. HD is on the other hand measures for the dissimilarity of two contours C_1 and C_2, which is defined by [140],

$$HD = max(sup_{p_1 \in C_1} inf_{p_2 \in C_2} d(p_1, p_2), sup_{p_2 \in C_2} inf_{p1 \in C_1} d(p_1, p_2)) \tag{4.9}$$

where inf represents the infimum and sup the supremum. The HD is the longest of all the distances from a point p_1 in one contour to the closest point p_2 in the other contour.

4.5.2 Results Analysis

The DSC was calculated between the automatic and true clinical contours, the results of which are presented in Figure 4.9. The DSC was found to be between 60% and 80% and the overall mean DSC is 0.74, which indicates good geometric agreement between the clinical and automatically generated contours. Since the contours were produced in 2D, Hausdorff distance (HD) is also calculated. The mean HD was found to be between 0.95 cm and 1.86 cm also indicating good overall agreement between the clinical and automatically generated contours. Figure 4.8 shows examples of typical contours produced by the algorithm (red line) and the corresponding contours produced by the clinical oncologist (blue line). Table 4.1 presents a comparison of the clinical volume and the volume produced by the algorithm and Table 4.2 shows the computation time required by the Matlab 2009b-based algorithm on a Dell Desktop with an Intel(R) Xeon(R) Duo processor, 2.66 GHz, 4GB RAM running Windows 7.

Table 4.1: Comparison of the clinical volumes defined by a radiation oncologist and the automatic volumes generated by the level set algorithm.

	Case 1	Case 2	Case 3	Case 4	Case 5
Clinical Volume (cm^3)	80.84	302.42	157.49	143.25	286.13
AutomaticVolume (cm^3)	72.69	265.93	157.38	114.38	213.65
Volume Difference (cm^3)	8.15	36.49	0.11	28.87	72.66
Difference (%)	10.08	12.07	0.07	20.15	25.38
DSC($\mu \pm \sigma$)	0.83 ± 0.07	0.74 ± 0.07	0.66 ± 0.1	0.74 ± 0.12	0.75 ± 0.07
DSC Range (min, max)	0.71,0.92	0.58,0.82	0.51, 0.86	0.56, 0.94	0.71,0.92
HD Range(min,max) (cm)	0.95 ± 0.29	1.15 ± 0.47	1.39 ± 0.44	1.37 ± 0.63	1.86 ± 0.71

Table 4.2: Computational time required by the algorithm to compute the tumour volume on each case. The total computational time includes execution of the level set algorithm in addition to the file I/O and data handling. The average computation time was calculated only on the slices containing a contour.

	Case 1	Case 2	Case 3	Case 4	Case 5
Total Computation time (sec)	552	964	1301	907	913
MR slices containing GTV	18	30	38	23	28
Average for each GTV (sec)	29.0	31.4	32.3	36.8	30.4

The difference between the automatic and clinical tumour volume was most significant in case 4, 20.15% difference corresponding to 28.87 cm^3 was recorded, and case 5, 25.38% difference corresponding to 72.66 cm^3. In all cases the automatic volume was smaller than the clinical volume, a characteristic noted in all cases investigated. For case 5 the volume difference can be explained by the exceptionally long period of time, 114 days, between the MR and CT data acquisition. During this time there was a significant change in the tumour burden of the patient, which was highlighted by the clinician on the radiotherapy planning CT scan. Furthermore, unlike cases 1 to 4 in which a GTV was defined, a CTV was defined for this patient.

One of the major advantages of this approach is that it is computationally efficient because the level set does not require reinitialisation during detection of the tumour boundary; a step that is often associated with slow convergence. The method relied on calculation of the gradient flow during evolution towards the tumour boundary. With the widespread variation in tumour intensity with glioma grade, and the difficulty in establishing gradients at the interface between tumour and normal tissue, there is a need to investigate level set evolution using the statistics of the region such as in the Chan Vese approach [58]. Furthermore, the performance of the approach could be improved by modelling the MR intensity variations using non-Gaussian statistical methods, particularly Rician methods, which have been widely used in MR analysis [134].

4.5.3 Clinical Evaluation

In March 2012 bespoke software was developed to randomly present the oncologist with the automatic and clinical contour for all slices of the five patients investigated. With the 3 years passing of time since SE first outlined the tumour volume on these patients it was assumed that there would be no conscious bias from this assessment. The quality of the contours, both automatic and clinical, was graded by SE as excellent, good, acceptable and not acceptable. For automatically generated contours, which are presented in Figure 4.10, 7% were graded as excellent, 60% good and 33% acceptable. Figure 4.11 shows examples of typical contours produced by the algorithm, which were graded by SE as excellent (bottom), good (middle) and acceptable (top). In each image the red line is the automatic contour and the blue line the

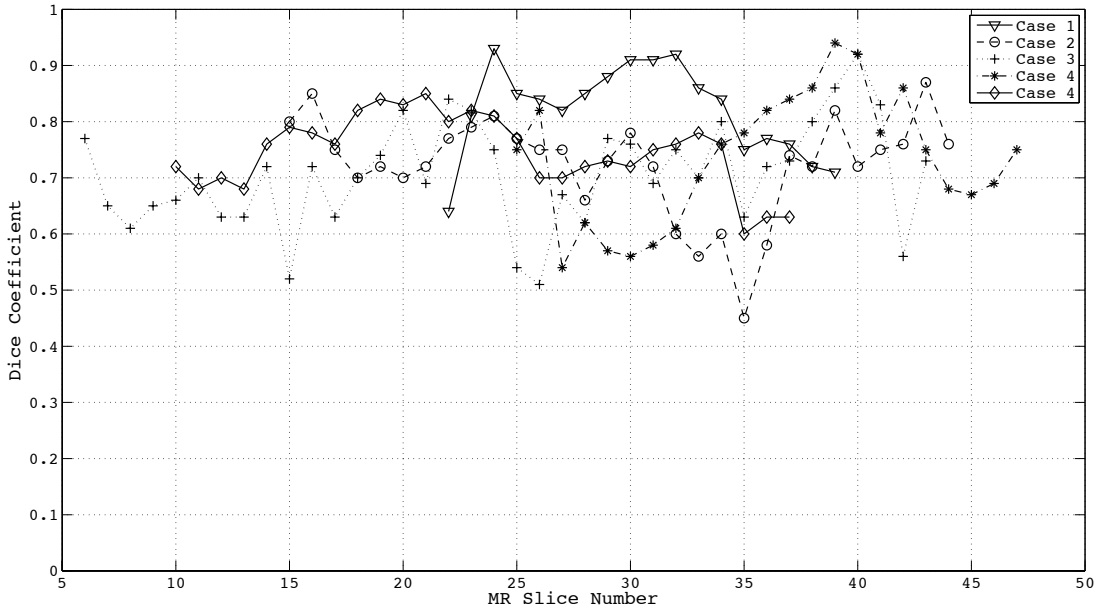

Figure 4.9: Results analysis by DSC.

original clinical contour. The evaluation results are included in Appendix A.

From the preliminary results presented the algorithm has the potential to be further developed to assist clinicians in the management of adults with malignant cerebral glioma. For example, including information on important functional areas would significantly improve the treatment of low grade glioma patients. However, more comprehensive analysis involving a much larger data set is required. This will also help to address important issues surrounding the inclusion of MR data in the radiotherapy planning process, which does not necessarily reduce inter-observer variability and has been show to result in larger tumour volumes than those produced using CT alone [52].

4.6 Conclusion

According to the Multimodal Brain Tumor Image Segmentation Benchmark (BRATS) organized in conjunction with the Medical Image Computing and Computer Assisted Intervention (MICCAI) 2012 and 2013 conferences, quantitative evaluations revealed considerable disagreement between manual delineation of various tumour sub-regions (DSC in the range 74%-85%), illustrating the difficulty of this task even for human experts [141]. In the latest

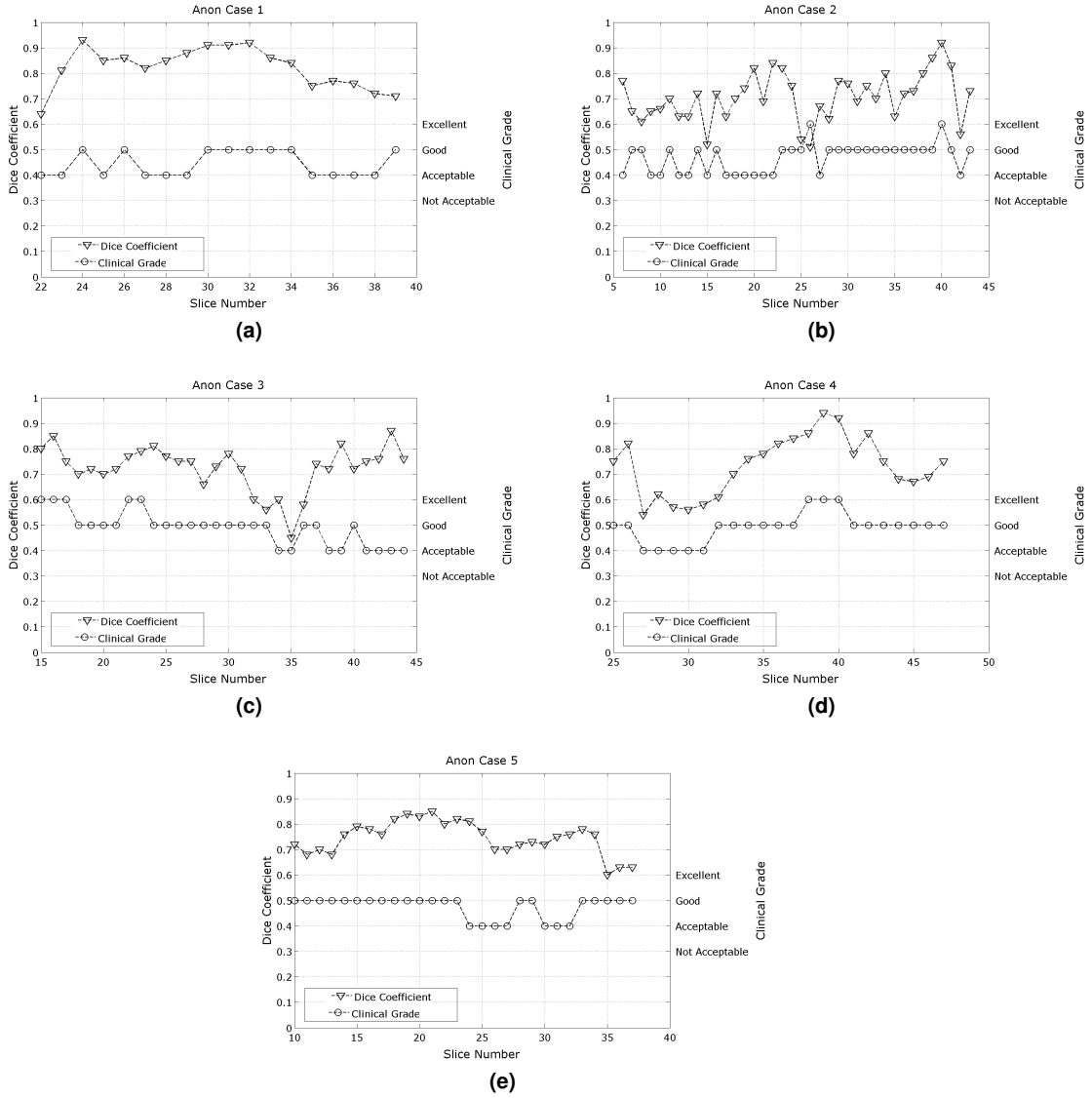

Figure 4.10: Anon Case 1-5: Performance of the automatic image analysis approach measured against the original contour for all patients where the top line is the DSC between the automatic and ground truth contours and the bottom line the quality of the automatic contour judged by the oncologist.

BRATS report [141], for the segmentation of giloma GTV ('core region' in the BRATS paper), the highest DSC was achieved is 0.75 by Subbanna et al. [129]. Another work by Guo et al. [142] gives a fairly quick segmentation (less than 1 minute per case) using a semi-automatic segmentation based on active contours, a mean DSC of 0.67 is achieved.

The approach presented in this chapter used a posteriori information on glioma GTV intensity to establish an adaptive active thresholding basis for level set evolution, which allows brain

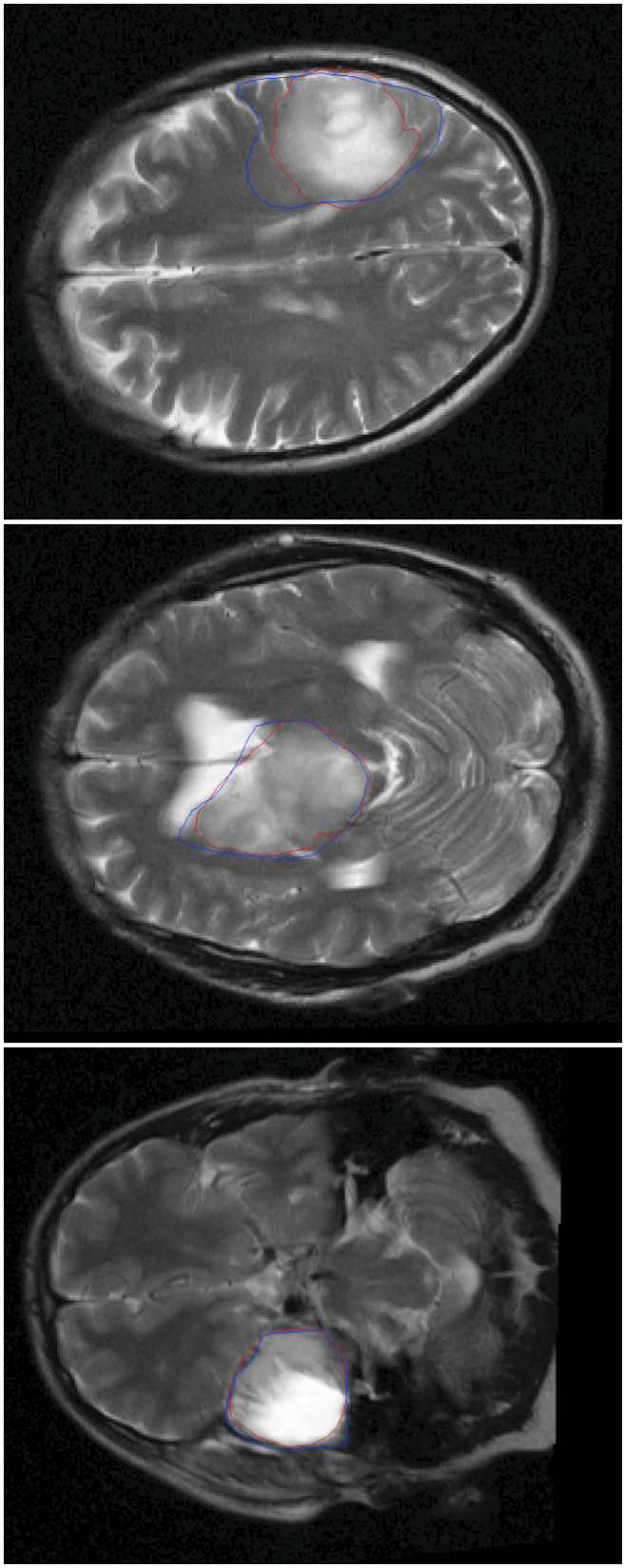

Figure 4.11: Oncologist's grade from bottom to top as, excellent, good, and acceptable.

GTV for radiotherapy to be estimated fully-automatically. The pilot results (mean DSC 0.74) presented on 5 patients demonstrate the efficacy of the approach, however, full validation is required on a much larger data set and using multiple observers to assess the automatically generated contours.

The ultimate aim of this work is to develop an approach to assist clinicians define the extent of tumour volume in a reliable and repeatable manner. This will not only save time but may reduce the radiotherapy fields used to treat brain cancer patients, which may be larger than necessary because of poor image information at the time of radiotherapy planning. This chapter reports our progress towards this aim and our ongoing work in this area.

Chapter 5

Automatic Delineation of Prostate GTV on Planning CT

In chapter 3, both low level image features based on the first order distribution and high level image features used in ASMs were reviewed. Conventional ASMs use grey level profiles obtained from the image intensity or image derivative, which are not sufficient for prostate GTV segmentation on CT images [69]. Here a new scheme is presented for the prostate GTV delineation based on an ASM with an optimised feature searching profile, which takes into account the texture statistics of the prostate and surrounding organs [2].

5.1 Introduction

Prostate cancer accounts for approximately 14% of all cancers diagnosed in men and is the third most common cancer worldwide [143]. External beam radiotherapy remains an important curative treatment for prostate cancer and with the increasing incidence of disease through greater prostate cancer diagnosis and an ageing population, it is imperative that treatment is as efficient as possible. There is a growing interest in radiation oncology on the use of models of anatomy, which contain information about the expected shape and appearance of structures of interest, to assist in the segmentation of different anatomical structures. ASMs [26] have been widely used in medical image analysis for delineation of lungs, heart and pelvic organs [116, 98, 31]. However, shape models of the GTV in radiotherapy planning CT of the prostate

2. This chapter is based on the following publication:
iii) Cheng K, Feng Y, Montgomery D, Steel R, Liao H, McLaren DB, McLaughlin S, Nailon WH. Active Shape Models for Prostate Cancer Planning with Optimized Features. Submitted to the International Society for Optics and Photonics (SPIE) 2014, San Diego.

have not been constructed due to large variations in shape and appearance.

According to a recent survey, 84% percent of the prostate cancer patients include in the study were diagnosed with multi-focal prostate disease [144], which mean cancerous focuses can be spread randomly within the prostate [145]. They also justified that the prostate gland must be included in the CTV volume if the aim is to treat all of the tumour focus. As discussed in Section 2.5.1, the CTV defined in the ECC radiotherapy protocol for prostate cancer, is formed by adding a 1 cm margin all around except posteriorly where it is 0.6 cm. Consequently, it is easy to understand that, the GTV shape of prostate cancer has limited shape variation from the prostate gland, which is suitable for the segmentation using SCDMs. The shape variation of prostate GTV is influenced by two major factors: the stage of the disease, for T3-T4 prostate cancer, seminal vesicles are included in the GTV volume, while not included for cases of stage T1-T2; patient's age has a significant impact on the prostate gland volume size, with a larger GTV volume expected for older patient [146]. The impact of these factors is demonstrated in the ASM shape variation analysis (Section 5.5).

The difficulty in contouring the prostate GTV on CT image is that the limited resolution and low soft tissue contrast. This is further complicated by the close proximity of the prostate to the bladder and rectum, which need to be identified as OARs.

In this chapter a novel solution is proposed to solve these issues that uses an ASM model trained on 2D contours identified by a radiation oncologist on sequential CT image slices. The pre-processing of the clinical contour is described in Section 5.3.3, including a new group-wise shape registration algorithm. To train the model the shape deformation was learnt using the conventional ASM approach [26]. In a novel development to the ASM model, a profile feature was selected from pre-computed texture features by minimising the MD to obtain the most distinct feature for each landmark, which is covered in Section 5.6. In Section 5.7, the interior of the GTV was modelled using quantile histograms to initialise the shape model on cases being segmented. The proposed model was initialised automatically based on appearance quantiles with shape model parameters summarised in Section 5.8 followed by an evaluation of the results in Section 5.8.1.

5.2 Previous and Related Work

There has been research on the segmentation of healthy prostate based on ASM. Before the publication of this work, limited application was found about the segmentation of prostate GTV on CT images because of the difficulty of this task. Relative studies on prostate gland (seminal vesicles not included) segmentation are reviewed here.

The delineation of prostate usually includes the segmentation of the bladder as an OAR, which is difficult because of a low intensity gradient at the prostate-bladder junction, especially on CT images. Studies have been done to overcome this obstacle towards a reliable and accurate GTV delineation. Due to the high shape correlation between pelvic organs, the SCDMs of prostate may be built for prostate only [147, 75], or a combination of organs such as prostate and rectum [121], prostate and bladder [116, 148]. Compared to the prostate, the bladder shape is much less predictable due to filling inside the bladder and consequently the bladder is not suitable for segmenting using shape models. Costa et al. [98] segmented the bladder using a region growing method and the prostate model was constructed incorporating the shape of bladder as a prior. Rousson et al. [31] simultaneously segmented the bladder and prostate with an non-overlapping constraint and a level set framework was used to segment the bladder. Ginneken et al. [69] replaced the gradient profile in conventional ASM by histogram based features in which each landmark profile using different features to train a KNN classifier best classify the interior and exterior points. In the initialisation of the model, Rousson [31] queried by human interaction, Chen et al. [121] put anatomical constraints using pre-located pelvic bone, and as mentioned before, affine registration was used in the work of Costa et al. [98].

DSCs of prostate GTV in inter-patient study have been reported by Chen et al [121] (0.82 median DSC), Costa et al [98] (0.77 mean DSC), Song et al [149] (0.80 mean DSC) and Rousson et al [31] (0.81 mean DSC). In terms of intra-patient study, the DSC reported are significantly improved to the range between 0.84 and 0.92 [98, 150, 151, 152].

In a more recent study, Martinez et al. [153] used a deformable shape model under a Bayesian framework, the segmentation is obtained by mapping a set of multi-scale edge observations to the space of organs with a customised likelihood function, a mean DSC of 0.87 was achieve on an inter-patient data set. Shao et al. [154] introduced a local boundary regressor based on

regression forest to vote the entire boundary of a target organ, bypassing the diffusivity in defining the 3D correspondences. The prostate segmentation was driven by both the regression forest map and a ASM model, a mean DSC of 0.88 was achieved.

5.3 Data Set Definition

5.3.1 Image Acquisition

Planning CT scans from from 42 prostate cancer patients treated at the ECC were investigated in this study. Each image stack contained 63 to 105 CT images of which between 16 to 28 slices were contoured. All CT images were acquired on a GE Medical System HiSpeed CT scanner at 3 mm slice thickness and a 12-bit grey-level range. The size of each slice was $512 * 512$, a sub-image of size $260 * 410$ region was sufficiently large to contain the whole pelvis, and was therefore extracted from the original image using the body boundary as landmarks from each image.

5.3.2 Ground Truth GTV Contour

In order to reduce the variability The GTV contouring process strictly follows the ECC radiotherapy protocol for prostate cancer. Contouring was performed by the experienced radiation oncologist (SE) using the Varian Eclipse^{TM} (v6.5) treatment planning system (Varian Medical Systems, Inc. Palo Alto, CA, USA). As shown in Figure 5.1, the points at which the mouse was clicked by the clinician on the clinical contours are not evenly spaced along the GTV boundary.

5.3.3 Data Conditioning

The data conditioning refers to constructing an isotropic prostate GTV shape and its corresponding 3D volume image for the training of the ASM. Binary masks are generated from the clinical contour and duplicated superior to inferior between the original CT images to form an

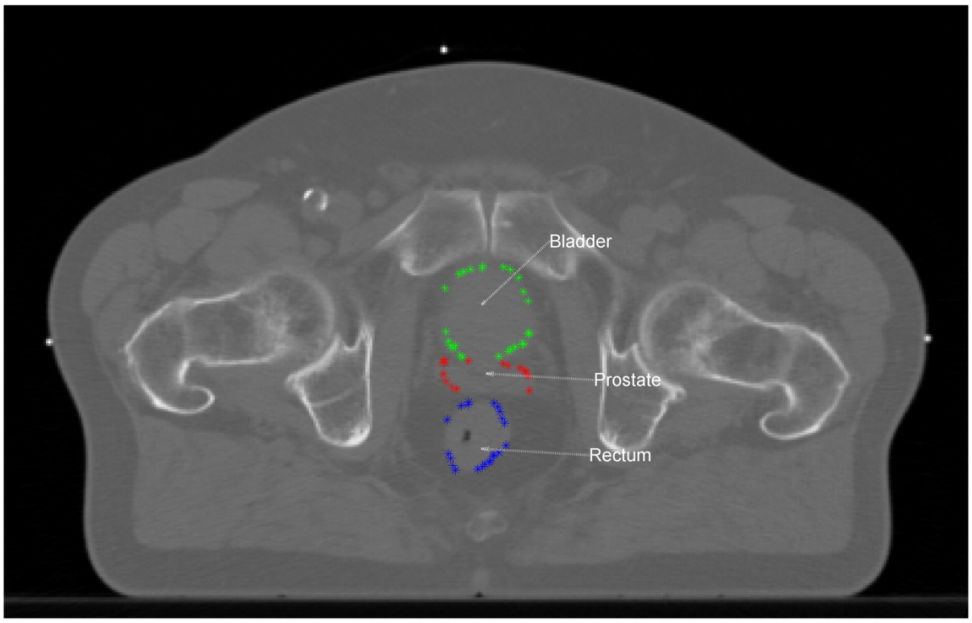

Figure 5.1: An axial CT scan of the pelvis in which the prostate GTV (red), bladder (green) and rectum (blue) have been contoured. Contours were delineated based on clinical knowledge and what you are looking at is the points at which the mouse was clicked by the oncologist.

isotropic binary volume. Isotropic prostate shapes represented by finite points are obtained by an iso-surface extraction algorithm and the corresponding image volume shown in Figure 5.2.

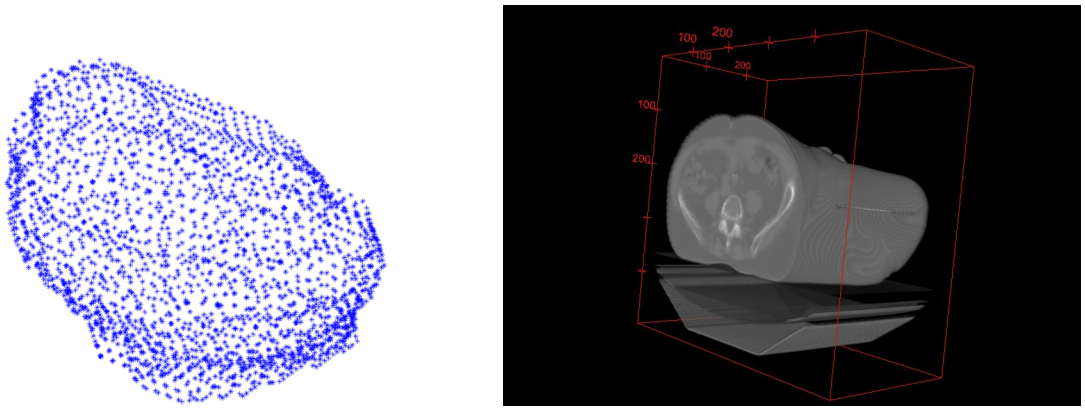

(a) **(b)**

Figure 5.2: (a) An iso-surface of the prostate GTV represented by 2604 points. (b) The corresponding isotropic image volume obtained from stacking the CT images.

5.4 Group-wise Shape Alignment and Correspondence Definition

5.4.1 Group-wise Registration of Point Sets

The main purpose of point set registration is in establishing correspondence among more than two groups of objects. Consequently, a group-wise registration scheme is required to efficiently and accurately register the whole group together. It is common practice to perform a pairwise registration of every subject in the group to a reference subject, or the group mean, based on: ICP [75], minimum description length (MDL) [155] and shape context followed by ICP [156]. These approaches are believed not fully persuasive in medical cases, due to the pronounced anatomic variability between individuals [30]. CPD method outperforms ICP and RPM algorithms in the presence of noise and outliers [84] and is more effective at dealing with non-rigid transformation. The disadvantage of the CPD method lies in the large in-plane rotation, which is believed can be compensated using other method before CPD is applied. A new group-wise registrations scheme is introduced to register multiple point sets, using the combination of ICP and CPD, for the training of ASM model for prostate GTV segmentation, as demonstrated in Section 5.4.2. Compared with the methods in [75, 155, 156], the proposed scheme is more memory efficient because it does not require all training shapes to be loaded at a time.

5.4.2 A New Group-wise Registration Scheme

Shape alignment (point set registration) is an indispensable component in the construction of SCDMs. As a geometric feature, the mean shape and its variation of the prostate GTV need to be well preserved in the merge of the training data set. Consequently, an accurately defined correspondence between the training archive is fundamentally important in the training of the ASM. In terms of 3D shapes, it is difficult to predict the length of the point set acquired using iso-surface method, as it depends on the surface geometrical complexity. However, shape analysis using PCA requires that the input shape vectors have an identical length. Group-wise registration scheme which register the group to a reference shape can solve this problem easily, it can be understood as the group is re-sampled into the same size of the reference shape. Here

a new group-wise registration scheme is introduced to solve the correspondence definition and shape vector length regularisation simultaneously as shown in Figure 5.3.

A test set of 4 prostate GTV shapes extracted from the isotropic binary volume are used

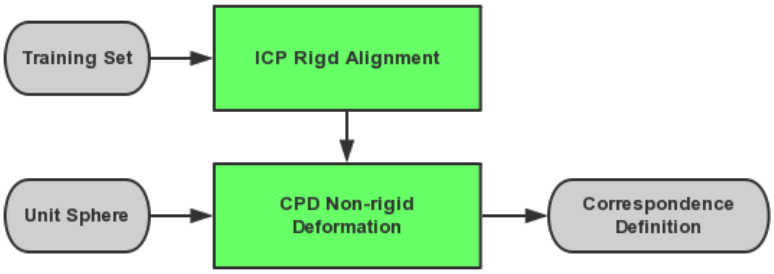

Figure 5.3: A new group-wise point sets registration scheme

here to explain how the registration scheme works. Variation in rotation and translation is first removed using rigid ICP registration to compensate for the weakness of CPD in dealing with large rotation. As shown in Figure 5.4, the 4 prostate shapes are rigidly aligned. Instead of registering all other cases to a selected shape or the group mean, as the common practice does, a unit sphere (Figure 5.5) represented by 2562 points is non-rigidly registered to the pre-aligned prostate GTVs using the CPD algorithm non-rigid deformation, as shown in Figure 5.6 and Figure 5.7. Consequently, the group-wise correspondence between all shapes are implicitly defined through the unit sphere vertices. Figure 5.8 demonstrates the group-wise correspondence in different colours. Compare with the scheme used in [155, 156], the proposed algorithm has a larger variation tolerance and is more memory friendly.

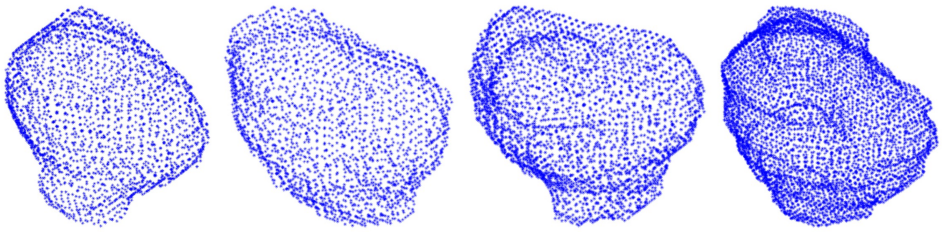

Figure 5.4: A group of 4 prostate GTV extracted from binary volume mask, which provides as the ground truth segmentation. From left to right, prostate GTV is represented by N_1, N_2, N_3 and N_4 points. These shapes have been aligned rigidly using ICP method to remove large variation in rotation and translation.

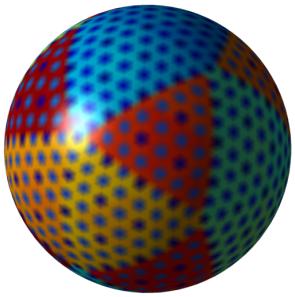

Figure 5.5: A unit reference sphere to be registered with other shape.

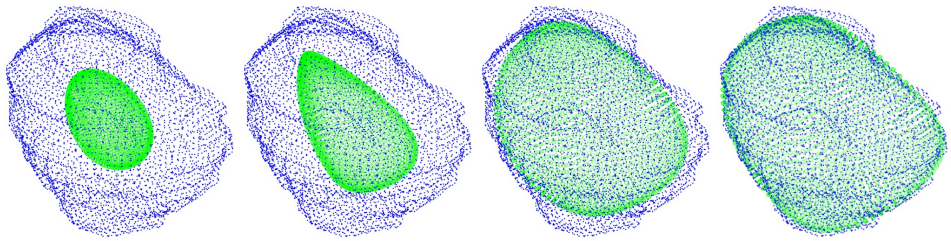

Figure 5.6: CPD non-rigid registration after 1, 5, 12, 24 iterations (left to right).

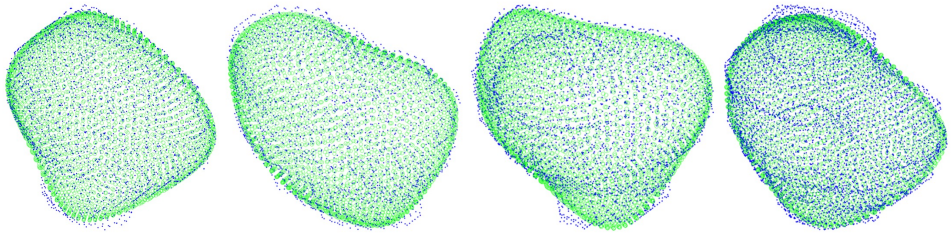

Figure 5.7: Converged CPD registration of unit sphere and shapes in Figure 5.4.

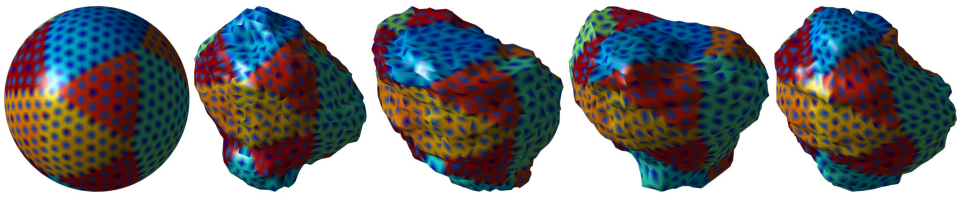

Figure 5.8: The group-wise correspondence defined through the unit sphere (left).

5.5 Shape Variation Analysis

The shape variation of a prostate GTV is expected to be larger than the healthy prostate, as described in Section 5.1. The shape training used here followed the convention for the ASM method [26] proposed by Cootes et al as introduced in Section 3.7.1. The shape model parameters control the GTV shape within an expected space region, normally within two

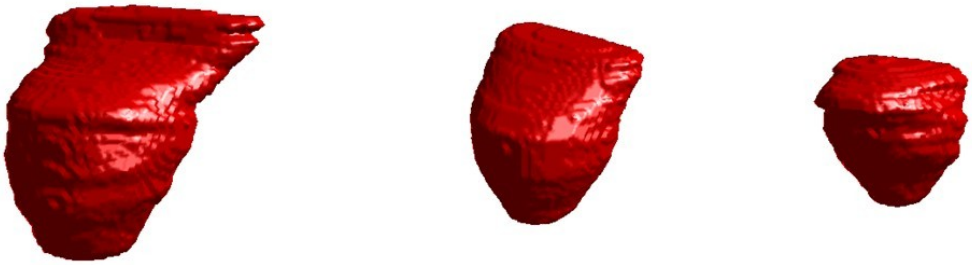

Figure 5.9: The middle shape is the mean shape of the ASM, the left and right shape are deformations by varying the first shape parameters by $\pm 2\sigma$.

.

standard deviations [26]. In this model, 95% of the shape variation of the GTV, including the prostate and seminal-vesicles, was retained. This was represented by the largest 18 shape deformation and the corresponding shape parameters according to Equation (3.43). Figure 5.9 shows the mean shape of the model and two deformations by manipulating the largest shape parameter. The physical meaning of the first shape deformation in Figure 5.9 is considered to be composed of two parts, a volume change and a shape change. Recall Section2.4.3, T3 and T4 prostate cancer involves the seminal vesicles which is reflected by the left shape in Figure 5.9. The prostate volume is influenced by the patient's age [157], however in this study, the patients' age information was not included in the training of the model. These two factors presented 34.77% of the overall shape variation in our model, as shown in Table 5.1.

Table 5.1: Shape Variation of the First 5 PCs

	1	2	3	4	5
Eigenvalue	108976	58447	33835	23589	18508
Individual Contribution	34.77	18.65	10.80	7.53	5.91
Cumulative Contribution	34.77	53.43	64.22	71.75	77.66

5.6 Texture Optimisation

The difficulty in segmenting prostate GTV based on CT image intensity has been stated in earlier sections (Figure 2.7). In this section, a novel development to the conventional ASM is described. Recall Section 3.4.3, Figure 3.7 showed the potential to use image texture features to segment prostate GTV on CT images. Based on the defined correspondence, the texture optimisation procedure here intends to find a specific image feature which most efficiently distinguishes between the GTV interior and exterior at each landmark on a GTV surface. As discussed in Section 3.4.3, 3D texture features includes: intensity, derivative, mean, variance, coarseness, skew, kurtosis, energy and entropy was pre-calculated. Only one out of these nine features were selected for each specific landmark, which best classified the GTV interior and exterior. This was known as the most distinct feature and was selected by minimising the overall MD among the training data set.

The assumption made here is, the built ASM is optimised if it gives the same segmentation as the ground truth GTV. As introduced in Section 3.4.3, MD is used in the segmentation of ASM to find the optimal displacement of landmark points. Consequently, the texture selection is based on minimising the MD among the training archive. The pipeline of the algorithms is shown in Figure 5.10 and is described as follows:

The kurtosis feature is used here as an example, for landmark $X_i(x_i, y_i, z_i)$ $(i = 1, 2..., n)$ from the case j $(j = 1, 2..., m)$, the corresponding Kurtosis feature profile vector g_{ij}, was extract from the pre-calculated and normalised kurtosis texture image. Since the group-wise correspondence between shapes are defined already, a distribution of Kurtosis profiles for ith landmark from all training cases can be constructed as $[g_{i1}, ..., g_{im}]$, as shown in Figure 5.10 (left row). The Kurtosis MD between a individual case g_{ij} and the modelled distribution $[g_{i1}, ..., g_{im}]$ was calculated using Equation (3.44) as MD_{ij}, as shown in Figure 5.10(second to the right). The overall MD of the landmark X_i using the kurtosis feature was formed from,

$$MD_i(Kurtosis) = \sum_{j=1}^{m} MD_{ij}(Kurtosis) \tag{5.1}$$

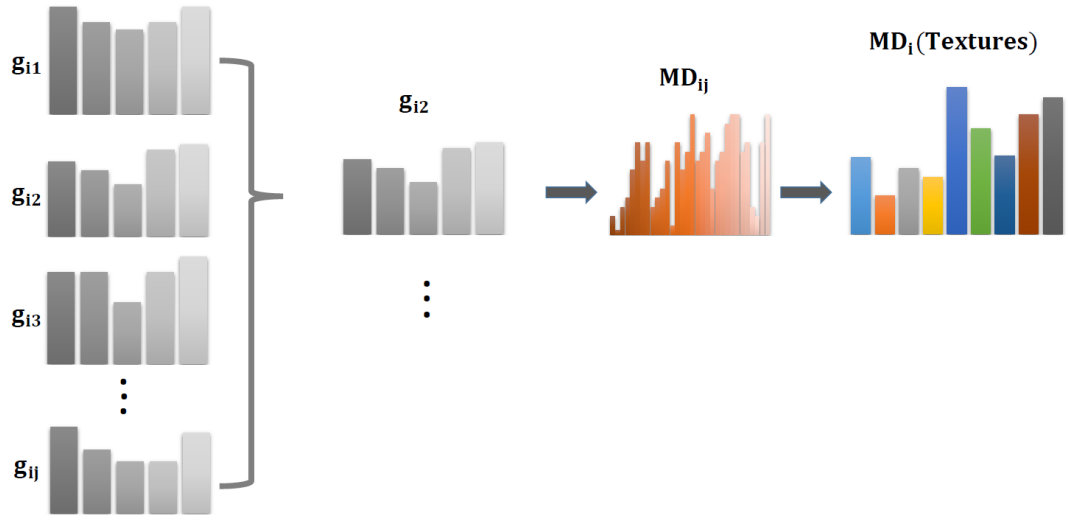

Figure 5.10: The pipeline of feature optimisation algorithm.

.

The optimised feature for landmark i was defined by the texture feature with the smallest $MD_i(Textures)$ calculated by Equation (3.44), as shown in Figure 5.10 (first to the right). For improved accuracy and robustness, the MD in Equation (5.1) involves 4 adjacent landmarks perpendicular to the shape surface on both sides, with a Gaussian weighted voting as,

$$MD_i(m) = \alpha_1 MD_i(m) + \alpha_2 MD_i(m \pm 1) + \alpha_3 MD_i(m \pm 2) \tag{5.2}$$

where α_1, α_2 and α_3 are the Gaussian weights. $MD_i(Textures)$ contains 9 MD for each texture features, the one with the lowest MD is selected as the most significant feature. The optimisation process went through all the m landmarks and gives a landmark-wise feature selection vector L, indicating the optimised feature number for each landmark as function of i,

$$Textures = [intensity, derivative, mean, variance, coarseness, skew, \ldots kurtosis, energy, entropy] \tag{5.3}$$

$$Texture = Textures(L(i)) \tag{5.4}$$

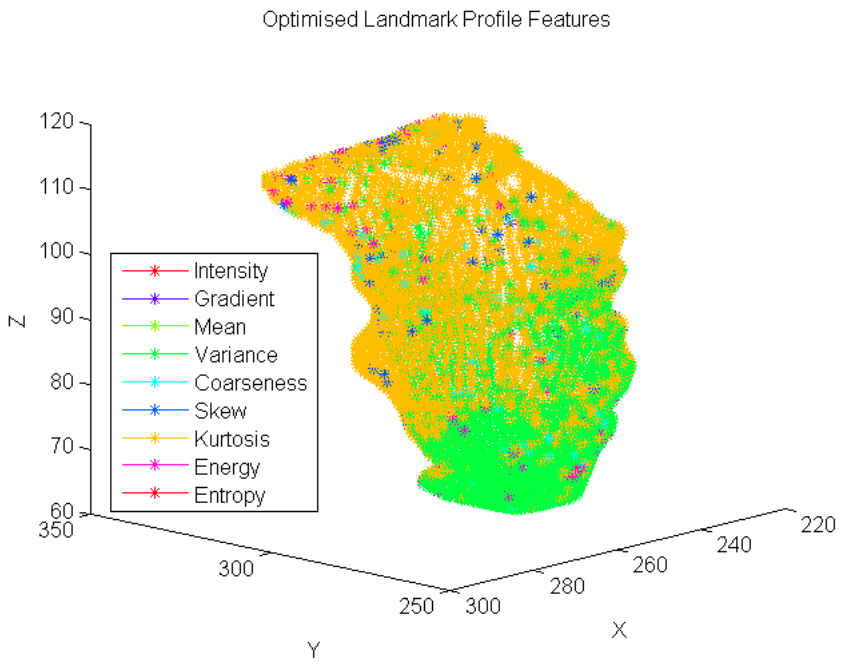

Figure 5.11: Most-significant feature identified for each landmark of the GTV model. Where the prostate is adjacent to the bladder kurtosis is most significant. Variance dominates at other locations because of the large intensity variations in the surrounding tissue.

Figure 5.11 indicates the selected feature for each landmark on the GTV surface. On the prostate surface where adjacent to the bladder, the kurtosis feature is most significant. The variance feature dominates at other locations because of the large intensity variations in the surrounding tissue. This feature vector is a key component of the proposed ASM. During the search of ASM, a specific feature image is obtained using the feature vector and the corresponding feature image is used to drive the landmark displacement. The selected feature for individual landmarks is the most appropriate for distinguish between the GTV interior and exterior and maximise the posterior-probability of segmenting prostate GTV based on the given training set.

5.7 Automatic Initialisation Using Regional Intensity Quantile Functions

Regional Intensity Quantile Functions (RIQF) is a probabilistically representation of the image appearance, which is derived from the intensity histogram within a region of interest. Assuming two continuous distribution q and r, with cumulative distribution Q and R, the Mallow distance (earth mover's distance)(MaD) measures the similarity between q and r and is calculated by,

$$MaD(q,r) = (\int_0^1 |Q^{-1}(t) - R^{-1}(t)|^p dt)^{1/2} \tag{5.5}$$

An n-dimensional RIQF is actually the inverse cumulative distribution function represented *by* n quantiles, each storing the average of 1/n of the distribution. Distribution q and r can therefore be represented as vectors in Euclidean space as $\hat{q} = (\hat{q}_1, ..., \hat{q}_n)$ and $\hat{r} = (\hat{r}_1, ..., \hat{r}_n)$. The Mallow distance between q and r is defined as,

$$MaD(\hat{q},\hat{r}) = (\frac{1}{n}\sum_{i=1}^{n} ||\hat{q}_i - \hat{r}_i||)^{1/2} \tag{5.6}$$

Histogram distributions are interpreted by RIQF as points in an n-dimensional Euclidean space in which the similarity of distribution corresponds to the M_2 metric. The mean shift and variance scaling of a distribution are then represented as linear change in the RIQF feature space, where PCA can be employed. RIQF is considered to be a regional based feature, which was implemented in many regional based statistical modelling applications [116, 120].

In this study, the appearance of the GTV interior was modelled using RIQF and applied as prior to initialise the trained ASM into new images. PCA was applied to retain 98% of the appearance variation, as shown in Figure 5.12. The mean shape of the model is moved across the whole pelvic region to determine the lowest quantile difference with the approximate initialisation location $P(x,y,z)$. A multi-start initialisation is performed at locations offset by 5 pixels in x,y and z to $P(x,y,z)$, and matched shape texture profile to the model. The displacement with the lowest MD is taken as the true start location.

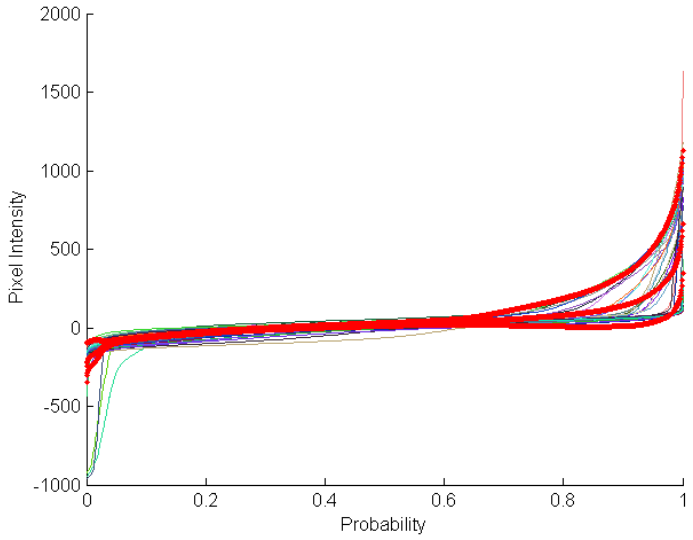

Figure 5.12: The red lines show the mean and $\pm 1.5\sigma$ along the direction of the 1^{st} principal direction of variation of the GTV interior. The other color lines are the quantiles of the GTV interior of each case.

5.8 Automatic Contouring the Prostate GTV

The searching scheme of the landmark-wise shape model is similar to the conventional ASM scheme, only differing in the profile extraction. For a new image to be segmented, 9 texture images are firstly calculated and profile used to displace the landmark i are extracted from the corresponding texture image defined by Equation (5.4). During the search, feature profiles are sampled at intervals of 3 pixels either side and the current landmark. The quality of the fit is tested by calculating the MD as in Equation (3.44). Landmarks are moved to new positions to give the best match (lowest MD) within a step size of 3 pixels. After each iteration, the GTV shape parameter is calculated and constrained to make sure that the active shape model is deformed within the pre-trained shape variation, until reaching convergence or maximum iterations. The parameters used in this landmark-wise texture optimised ASM are summarised in Table below.

Table 5.2: Landmark-wise texture optimised ASM parameters

Paramet	Value	Information
n	2562	Number of points used to represent GTV
n_l	5	Texture profile length
n_t	9	Texture image
n_s	3	Searching step size
n_{search}	20	Number of iterations
m	3	Shape constraint within $m\sqrt{b_s}$

5.8.1 Evaluation Using DSC

On patients previously treated at the Edinburgh Cancer Centre for prostate cancer 42 cases were selected for this study. From these 32 cases were randomly selected and used for training and the remaining 10 cases for testing. Results were evaluated by comparing the gold standard clinical contour to the automatically generated contour. The model achieved an overall Dice coefficient of 0.81 over all the test cases. Performance was increased to 0.87 when the volume size of the new case was similar to the mean shape volume of the model as shown in Table 5.3 and Table 5.4. Figure 5.13 shows examples of the automatic contour against the clinical contour in 2D.

Case Number	Case 1	Case 2	Case 3	Case 4	Case 5
Clinical Volume (Voxels)	67467	69237	46377	97755	51615
ASM volume (Voxels)	67348	69158	51778	64172	63745
Clinical Volume (cm^3)	65	67	45	94	50
ASM volume (cm^3)	65	66	50	52	61
Dice Coefficient	0.91	0.78	0.75	0.71	0.75

Table 5.3: Volume of clinical shape and ASM shape, and the DSC, from Case 1 to Case 5.

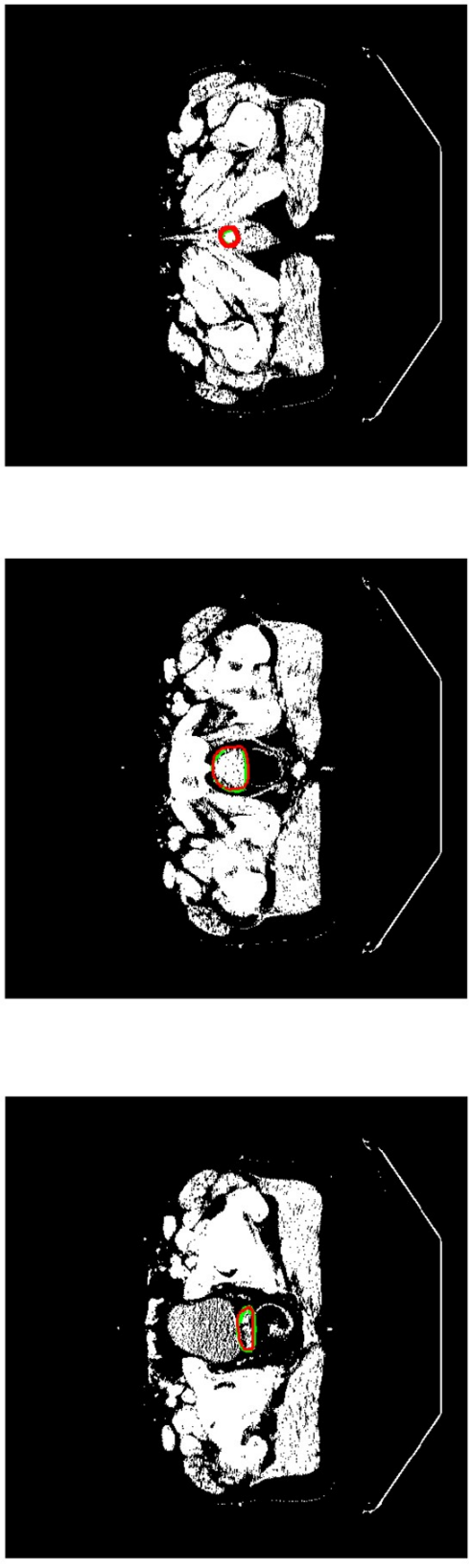

Figure 5.13: Clinical contour in green, ASM result in red. Bottom: a apical slice taken form inferior part of the GTV shape, contoured the seminal vesicles. Middle: central slice of the GTV shape, also the middle of prostate gland. Top: basal slice from the superior of the GTV, contoured the bottom of prostate gland. A thresholding process was applied on the CT images to show the structures in pelvis more clearly.

Case Number	Case 6	Case 7	Case 8	Case 9	Case 10
Clinical Volume (Voxels)	51211	73452	60877	63101	86874
ASM volume (Voxels)	53800	69120	65111	64678	67331
Clinical Volume (cm^3)	49	71	59	61	84
ASM volume (cm^3)	52	67	63	62	65
Dice Coefficient	0.89	0.82	0.89	0.87	0.75

Table 5.4: Volume of clinical shape and ASM shape, and the DSC, from Case 6 to Case 10.

5.8.2 Result Analysis

As shown in Table 5.3 and 5.4, the mean of the clinical volume is 64.6 cm^3 and the ASM volume is 60.6 cm^3. Degenerated performance is observed on the cases with larger volume variation. The ASM algorithm shows its disadvantage in finding global optimisation and could stick in local minima, it is because the ASM is naturally an edge based segmentation method. A study on the volume healthy prostate and prostate GTV reported that [158] a larger range of volume of prostate GTV (9-177 cm^3) is observed than the volume range of healthy prostate (15-140 cm^3). The patients' age involved in the study is between 42 and 90. Consequently, in order to improve the segmentation of prostate GTV, the volume variation has to be considered more seriously. This can be done by including the patient age during the training of the ASM and use age information as a prior in the segmentation of new images. While this requires a much larger training archive, which need be categorised into multiple groups based on the age.The training the ASM is employed to each groups and constructed a multi-scale or multi-age model.

5.9 Conclusion

This chapter presents a novel method for optimising an ASM that takes into account the statistics, in the form of texture features, of the important image structures. The results shows that the model performs well as in a inter-patient study ($Dice = 0.81$), particularly when the mean volume of the model is close to the volume of the case being matched ($Dice = 0.87$). As a summary, the proposed landmark-wise texture optimised ASM for automatic contouring prostate GTV has the potential to improved the radiotherapy performance, by providing reliable

auto-contours for the prostate radiotherapy planning. More work is required however, particularly on how to incorporate additional patient-specific clinical features such as age, stage, grade and PSA to improve performance. The performance of this algorithm is somewhat constrained by a limited amount of training, an increased number of training images is expected to improve the performance to some extent.

Chapter 6

Active Appearance Model for Auto Delineation of Prostate Cancer GTV on MRI

In clinical practice, MRI has become more widely used for the diagnosis and treatment planning of prostate cancer [159, 160]. There has also been increasing research interest into use of MRI for the segmentation of prostate and prostate GTV and for tracking disease progression [161]. The unparalleled soft tissue contrast on MRI is the key to building an AAM. In Chapter 5, the ASM model for prostate GTV on CT was shown to suffer from the small capture range, which is shared by most edge based methods. AAM utilise a region based metric in the training and segmentation, which has the potential to increase the capture range over the ASM method. The B-spline based FFD image warping algorithm (Section 3.5.4) was employed here to gather appearance information from training MRI data for the construction of an prostate AAM. In a novel development of the AAM, the image appearance of a smaller region around the ground truth GTV, is retained and used to segment the prostate GTV on new images.

6.1 Introduction

MRI provides sufficient pathological information required to automatically delineate the prostate GTV. Taking advantage of MRI the AAM method is capable of producing a reliable and reproducible segmentation of the prostate GTV.

6.1.1 Weakness of Conventional AAM in the Segmentation of Prostate

A conventional AAM models the image appearance of the contoured prostate GTV interior. In this chapter an extended AAM algorithm is introduced and applied on the planning MRI for automatic contouring of the GTV for prostate cancer radiotherapy.

As discussed in Section 2.4.4, brachytherapy is normally applied to early stage prostate cancer (PSA level is 10 ng/ml or less, Gleason score less than 6 and stage is T1 - T2a) [162]. With a PSA of between 10 and 20 and a Gleason score of 7, brachytherapy may still be an option as long as tests show that the cancer is unlikely to have spread outside of the prostate. However, external beam radiotherapy remains the mainstay treatment for prostate cancer and is usually used when brachytherapy fails to control tumour growth. In low dose rate (LDR) brachytherapy small radioactive seeds are inserted into the prostate gland and left to release their radioactivity for up to a 6 month period. Additionally, the GTV interior appearance is also influenced by the location of the focus of the cancerous growth within the prostate gland and the stage of the cancer. The inserted seeds and the multi-focal feature could cause a distorted appearance within the prostate on MRI images and make the conventional AAM model capture an inaccurate appearance, as shown in Figure 6.1. The brachytherapy seeds on CT (left) is very bright and can be easily identified, but appears as signal void with MRI (right) [163]. Additionally, recall Figure 2.4, gold markers are usually implanted into prostate gland for alignment, which benefits the treatment simulation and delivery and the fusion of modalities. The implanted gold markers has a similar impact on the image appearance as the brachytherapy seeds. It is therefore easy to understand that the conventional AAM modelling scheme, which includes the whole object interior, is not optimum for analysis of prostate GTV appearance.

Despite all of these, Vincent et al. [32] also claims that the conventional AAM method shows poor segmentation results at the apex and the base of the prostate. This is because of the continuous change of tissue without strong edge or texture and can be improved by involving surrounding structure such as the bladder and rectum. Coupled models (prostate and bladder [116], prostate and rectum [121]) are not considered here because they significantly increase the computational cost and require the clinical contour for other organs, which are not always available.

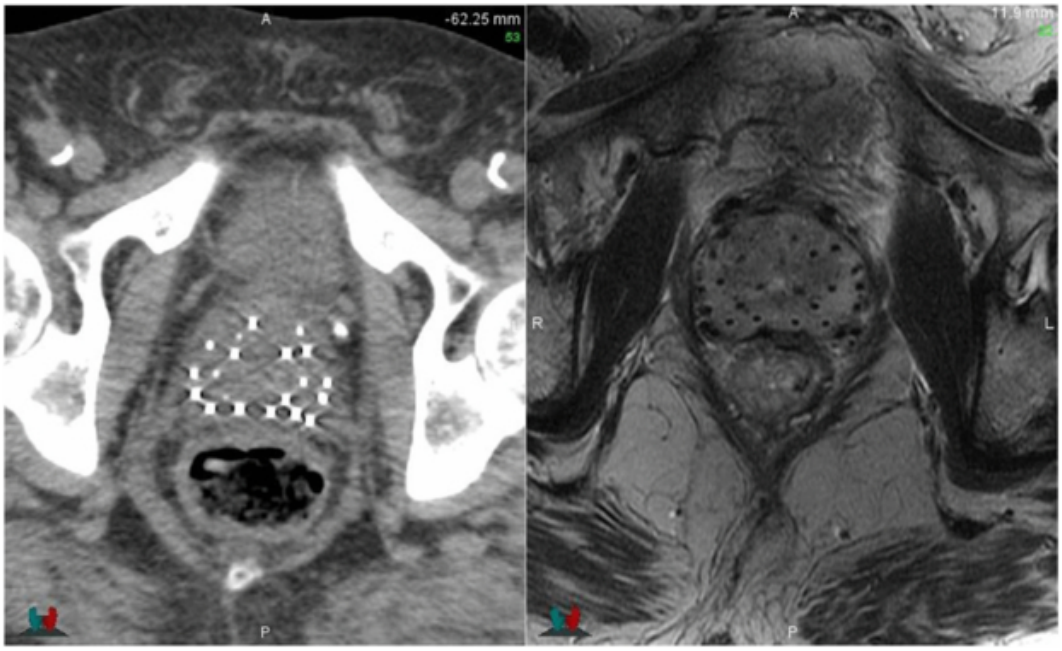

Figure 6.1: Post-implant CT and MRI images of a prostate cancer patient treated by brachytherapy. The brachytherapy seeds on CT (left) is very bright and can be easily identified, but appears as signal void with MRI (right) [163]. These seeds will cause a distortion in image appearance within the prostate gland and result in difficulties in modelling the prostate interior using AAM.

6.1.2 A Narrow Band Appearance Extraction

An extended AAM algorithm for segmenting prostate GTV, known as a narrow band AAM (NBAAM), is presented later in this chapter to overcome the disadvantages of conventional AAM. The NBAAM algorithm accounts for the interior appearance near GTV boundary to avoid potential appearance distortion as shown in Figure 6.1 and Figure 2.4. In addition to that, an exterior appearance including part of neighbouring organs is also included in the appearance analysis. This is achieved by expanding the GTV surface perpendicular to the surface. A 2D example is shown in Figure 6.2, where the clinical contour (blue) is expanded to from a belt shaped region indicated by the expanded contours (green). It requires further investigation to find the optimal amount of the expansion shown in Figure 6.2. While in this case the margins between blue contour and green contours are set to 1cm for both interior and exterior. It follows the definition of a CTV margin added to GTV (Section 2.5.1), which is based on a

clinical judgement taking into account sub-clinical malignant disease. The NBAAM captures a comparatively smaller region of appearance than the conventional AAM and the potential CTV is contained and analysed within this patch and can be used to segment prostate GTV effectively on the new image.

The remainder of this chapter is organised as follows, data conditioning including data re-

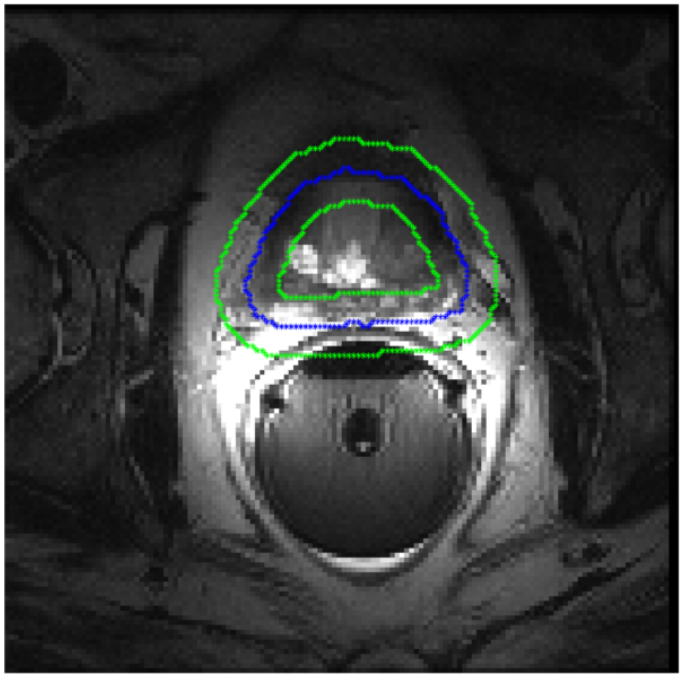

Figure 6.2: A 2D example of NBAAM appearance patch. The NBAAM appearance patch is defined by green contours and used to extract the image appearance for the blue clinical contour.

sampling and reslicing are described in Section 6.2. In Section 6.3 details about the NBAAM appearance extraction and training is presented. A customised automatic initialisation algorithm for NBAAM is proposed in Section 6.4, which was inspired by the CV level set model optimisation (Section 3.6.2). The performance of the proposed model for segmenting a new image and the important parameters used are summarised in Section 6.5. This is followed by a results evaluation in Section 6.6.

6.2 Data Set Definition and Conditioning

The data investigated in this chapter was downloaded from the MICCAI grand challenge: prostate MR image segmentation 2012 (MICCAI PROMISE 12) website. The training set provided contains 50 cases pre-contoured transversal T2-weighted MR images of the prostate.The data is multi-centre and multi-vendor and has different acquisition protocols (e.g. differences in slice thickness, with/without endorectal coil). The set was selected to ensure that there is a sufficient spread in prostate sizes and appearance [32]. Figure 6.3 shows sample slices from 4 centres to illustrate differences in appearance. The details of the acquisition protocols are listed in Table 6.1.

Table 6.1: Details of the acquisition protocols for the different centres

Centre	Field Strength	Endorectal coil	Resolution (mm/pixel)
Haukeland	1.5 T	Yes	0.5/0.5/3.6
Brigham	3 T	Yes	0.25/0.25/2.2
UCL	1.5 T and 3T	Yes	0.5/0.5/3.6
Radboud	3 T	Yes	0.5/0.5/3.6

Ground truth segmentation was provided as a binary volume, a slice of the segmentation and the corresponding MRI is shown in Figure 6.4. An iso-surface algorithm can be applied to transform the mask into contours as shown in Figure 6.4b. Before the analysis of the segmentation and image appearance, it was necessary to re-sample and re-slice the training image volume and the segmentation volume. The image re-sampling process was guided by the image resolution and in this data set all training images were re-sampled into a $1 * 1 * 1$ mm/pixel isotropic frame. The re-sampling and re-slicing process was repeated on the corresponding segmentation volume. Table 6.2 summarises 3 types of image volumes before and after re-sampling and re-slicing.

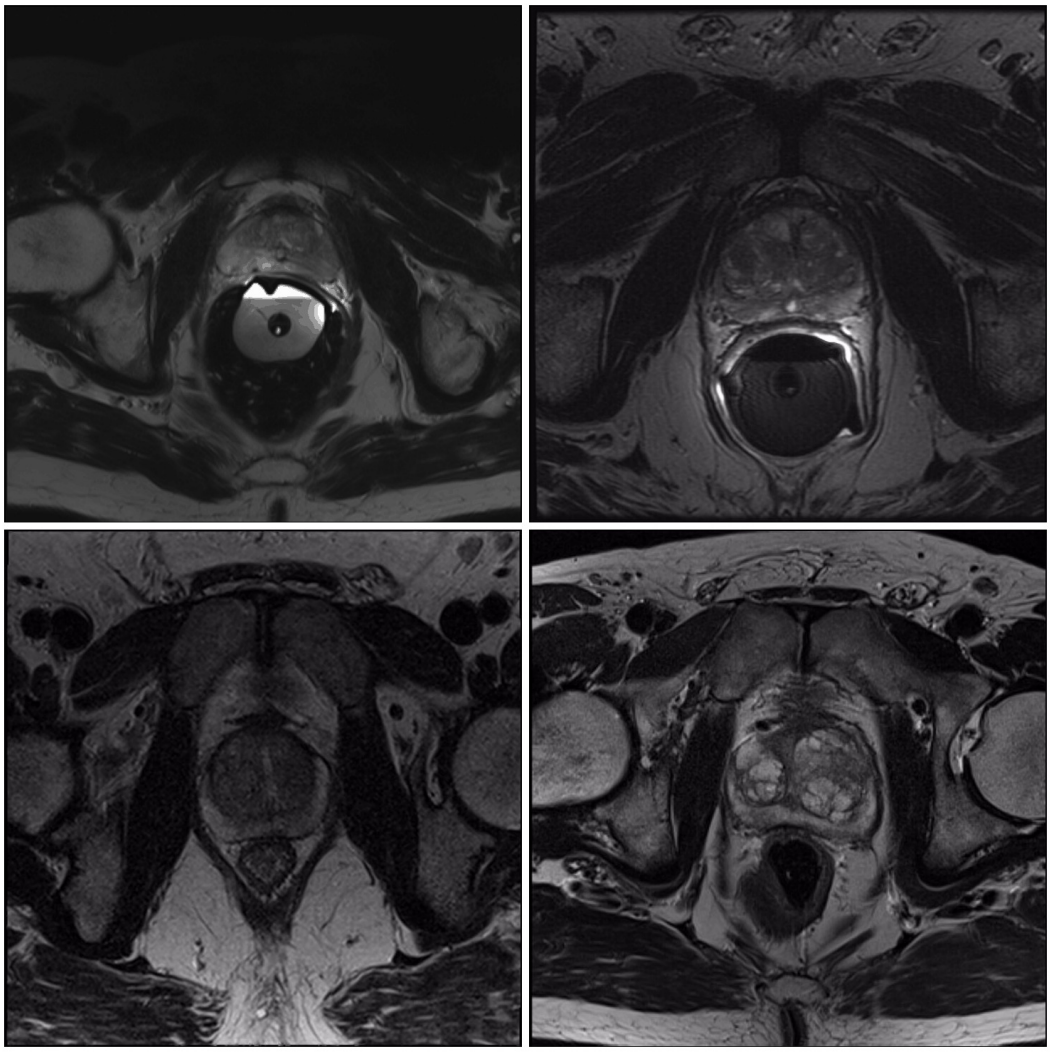

Figure 6.3: MRI scans from 4 centres, top left: Haukeland University Hospital, Norway, 1.5T with endorectal coil; top right: Brigham and Womens' Hospital. USA, 3.0T with endorectal coil; bottom left, University College London, United Kingdom, 1.5T and 3.0T without endorectal coil; bottom right: Radboud University Medical Centre, The Netherlands, 3.0T without endorectal coil.

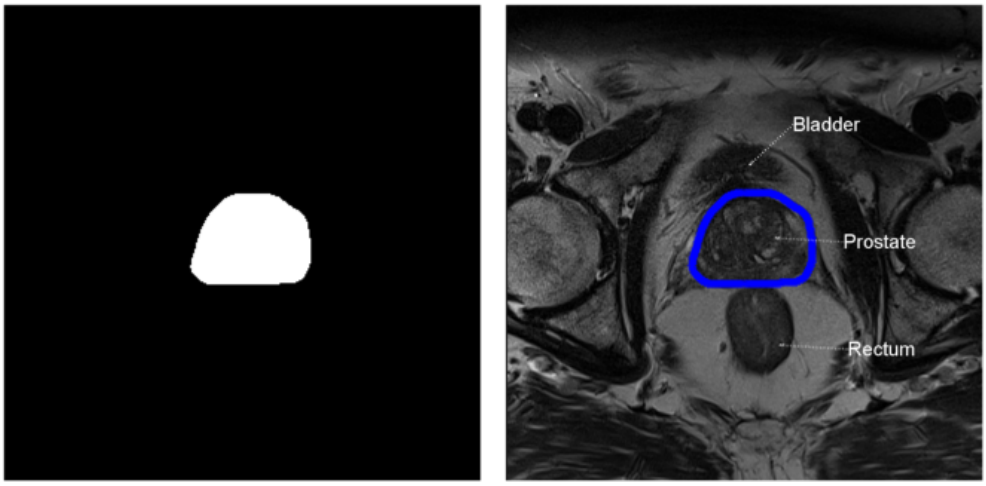

(a) (b)

Figure 6.4: An example image from the training set. (a) Segmentation provided as a binary mask extract from the 3D volume of size $320 * 320$. (b) An example T2-weighted MRI of size $320 * 320$, image spacing is $[0.6250.6253.6]$.

Table 6.2: Details image re-sampling and re-slicing

Volume Size	Resolution	New Volume Size	New Resolution (mm/pixel)
512*512*54	0.25/0.25/2.20	140*140*118	1.00/1.00/1.00
320*320*24	0.625/0.625/3.60	200*200*86	1.00/1.00/1.00
512*512*23	0.39/0.39/3.30	200*200*75	1.00/1.00/1.00

6.3 Narrow Band Active Appearance Modelling

This section provides details of the NBAAM algorithm, with an emphasis on the appearance training based on image appearance near the GTV surface. Group-wise registration (Section 5.4.2) and shape variation analysis (Section 3.7.1) were firstly carried out before the appearance modelling. The appearance patch in Figure 6.2 was extended to 3D. A 3-layer binary mask generated by displacements perpendicular to the GTV mean shape, which is defined as $\hat{S}_E$, $\hat{S}_M$ and $\hat{S}_I$ from the exterior to the interior, are shown in Figure 6.5c. This 3-layer surface is similar to the mean shape used in the conventional AAM and the training

shapes including their appearance are warped towards it and generates the shape free patch for the NBAAM appearance analysis.

Given an image volume V_i and its corresponding segmentation indicated by a shape S. The

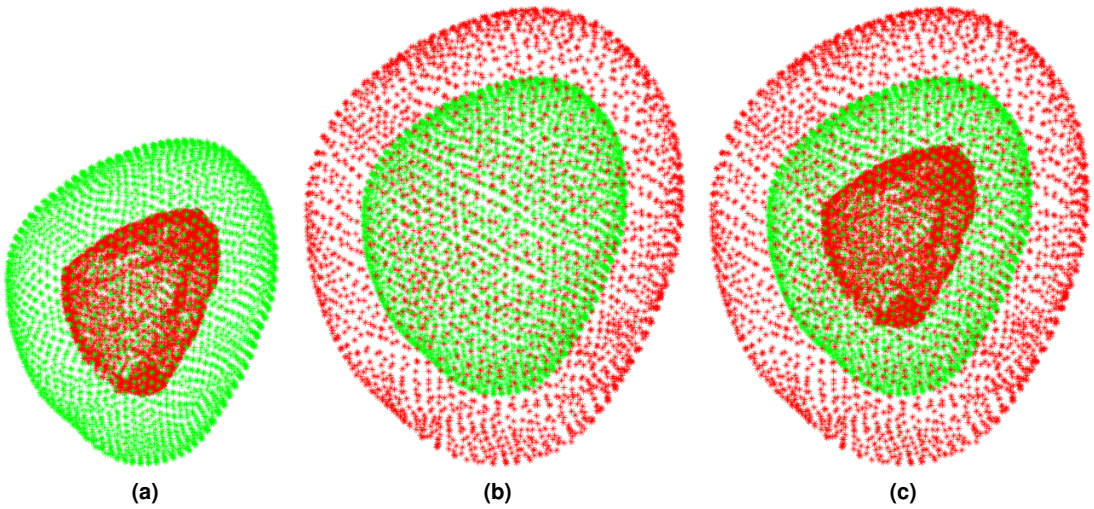

Figure 6.5: (a) Mean GTV shape $\hat{S}_M$ (green) and the surface $\hat{S}_I$ displaced 10 pixels interiorly (red). (b) Mean GTV shape $\hat{S}_M$ (green) and the surface $\hat{S}_E$ displaced 10 pixels exteriorly (red). (c) The 3-layer surfaces including $\hat{S}_E$, $\hat{S}_M$ and $\hat{S}_I$ from the exterior to the interior.

extended GTV volume V_E including its image appearance were firstly sampled by S_E, which was a 10 pixels displacement of S in the direction of the exterior, from the training image volume V_i. The image volume V_E was then warped into the reference shape $\hat{S}_E$ shown in Figure 6.5, using the B-spline based FFD introduced in Section 3.5.4, resulting in the shape free volume $\hat{V}_E$. The inner volume of $\hat{V}_E$ defined by the interior surface $\hat{S}_I$ is removed and formed the final NBAAM shape free patch $\hat{V}_i$. The shape free patch of NBAAM $\hat{V}_i$ has a similar shape with a "pitted avocado". The captured appearance variation involves pathological growth between GTV definition and the potential CTV definition and also surrounding parts of adjacent organs. The appearance void in the middle spares the potential disruption caused by brachytherapy seeds or gold markers.

The image appearance in $\hat{V}_i$ were extracted to construct the appearance feature vector g_i. The appearance vectors extracted from the training images were stacked into a appearance matrix and analysed following the conventional AAM method using PCA. The appearance captured are a "belt shaped" in 2D in the central slice of the "pitted avocado", as shown in Figure 6.6b.

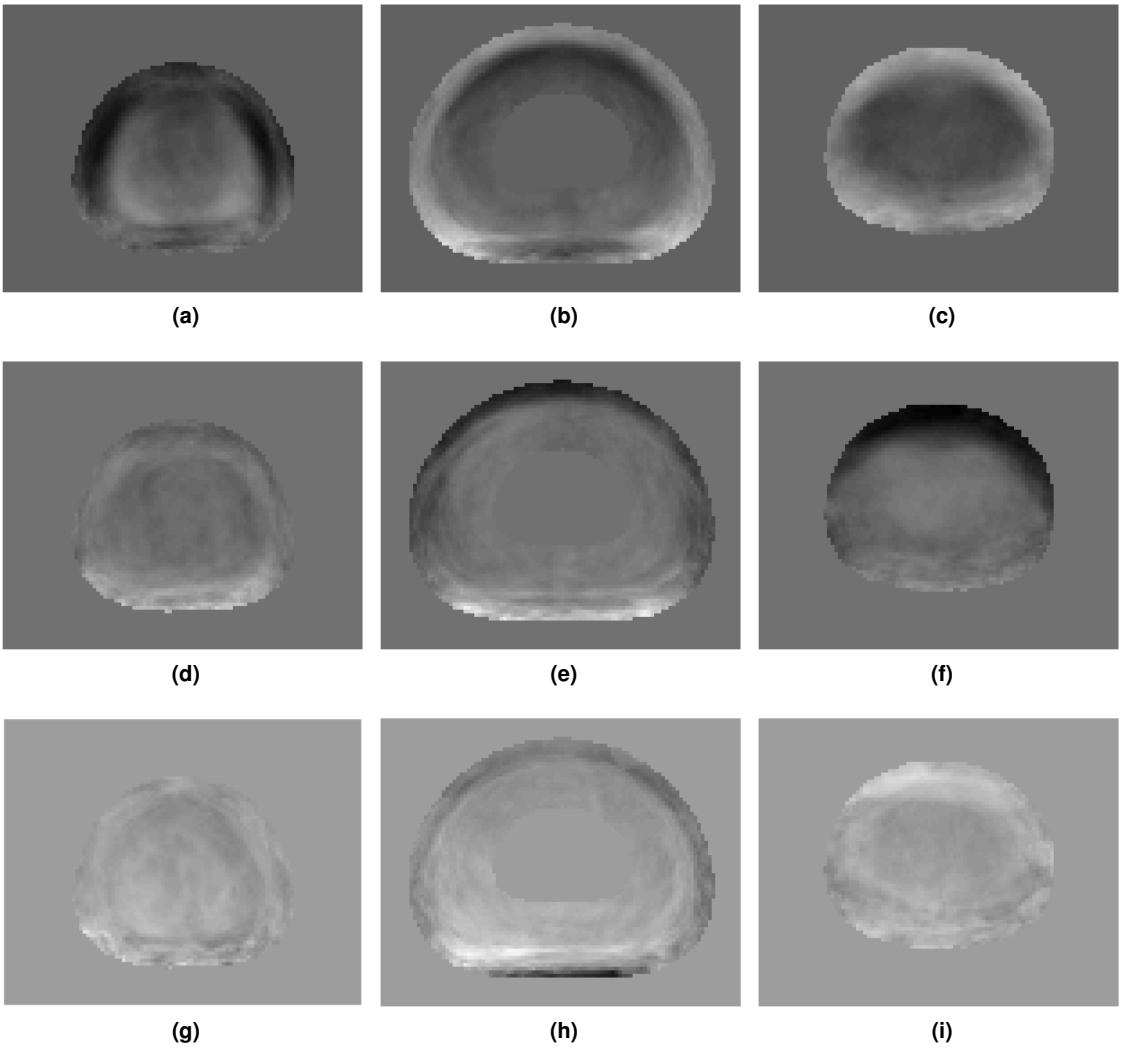

Figure 6.6: (a)-(c) Mean GTV appearance of apical, central and basal slices. (d)-(f) The first principal component of trained GTV appearance of apical, central and basal slices. (g)-(i) The second principal component of trained GTV appearance of apical, central and basal slices.

Figure 6.6d, e and f are the apical, central and basal slices of the first principal component of the trained NBAMM. Figure 6.6g, h and i were taken from the second principal component. It is worth noting that the appearance images shown in Figure 6.6 can be considered as a expanded GTV contour, which is expected to contains inhomogeneities. Firstly in the mean appearance patches (first row), salient boundaries are observed which gives a good segmentation of GTV interior and exterior. Recall that in Figure 6.4b, the appearance differences in the exterior of Figure 6.6a and c result from the different soft tissues adjacent to prostate apex and base. This is also reflected by the large variation in the upper region (dark regions) of the first principal component patches (second row), where the prostate is adjacent to the bladder and the lower region (bright regions) where the prostate is adjacent to the rectum. The second principal component shows variation in both interior and exterior, which contains information about the pathological growth near the GTV boundary.

The variation of shape and appearance was next combined together to obtain the shape appearance parameters in Equation (3.52), 95% of the shape and appearance variation of the GTV was represented by the largest 27 shape appearance deformation and its corresponding shape parameters.

Table 6.3: Combined Shape Appearance Variation of the First 5 PCs

	1	2	3	4	5
Eigenvalue	27274	19526	13460	11398	9617
Individual Contribution	16.41	11.75	8.10	6.86	5.78
Cumulative Contribution	16.41	28.16	36.27	43.13	48.9

3D shape patches show the shape and appearance variation more intuitively and Figure 6.7 shows the effect by varying the first component shape appearance parameter of the NBAAM model up to 2 standard deviation [27]. This segmentation did not include the seminal vesicles, the major shape variation is the volume change. In terms of image appearance, Figure 6.7a, b and c show the superior-anterior part of the NBAAM patches, in which the appearance variation was caused by the surrounding tissue of the bladder and possible pathological invasion. Figure 6.7d, e and f are the patches from the anterior view and their appearance are influenced

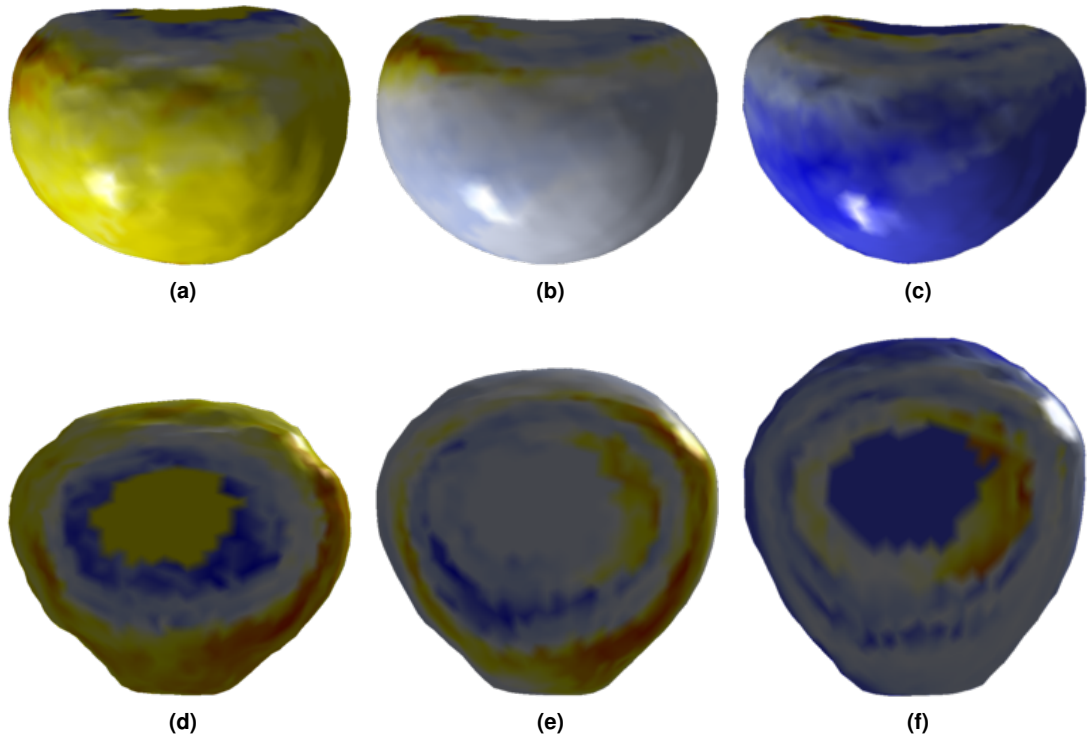

Figure 6.7: The effect of varying the first component shape and appearance parameters by up to 2 standard deviation. (a) and (d) are the appearance patches generated by subtracting 2 standard deviation from the mean patch. (b) and (e) are the mean of the appearance patch. (c) and (f) are generated by adding 2 standard deviation to the mean patch. (a), (b) and (c) are plotted from the superior-anterior view, where the prostate is adjacent to the bladder. (d), (e) and (f) are in the anterior view.

by the rectum. As discussed in Section 2.5.1, a CTV of prostate cancer adds a posterior margin of 0.6 cm for sparing the rectum from CTV definition. As the 1 cm expansion used here in this study, the NBAAM patch involves the rectum in posterior, resulting in a prostate-rectum junction in the second row of Figure 6.7. It is interesting to see that there is an area of inhomogeneity on Figure 6.7d, e and f, which reflects the volume of rectum tissue captured by the patch. A smaller region of inhomogeneity is observed in Figure 6.7d indicates that a smaller patch could involve less tissues from the rectum. While in Figure 6.7f a larger patch produces a large area of inhomogeneity, which influences nearly the whole posterior region. The distance between prostate and rectum is also a key factor influencing this homogeneity issue and the performance of the segmentation on new image , which is discussed in Section 6.7.

Figure 6.7 summarises the appearance captured by the NBAAM, which contains useful appearance information from the prostate and the surrounding rectum and the bladder. The appearance

extraction and training focus on the GTV neighbourhood region, which contains the boundary of either the prostate gland (T1 and T2) or the pathological growth (T3 and T4). NBAAM discards the inner prostate appearance which may contain distortions from multi-focal feature and brachytherapy seeds or the gold markers. The degraded performance of conventional AAM at the apex and base of the prostate can be improved using this appearance extraction scheme.

6.4 NBAAM Automatic Initialisation

As described in Section 6.3, the NBAAM captures the image appearance around the prostate GTV boundary in the shape of a belt as shown in Figure 6.6b. Recall the optimisation concept in the CV level set algorithm (Section 3.6.2), where Equation 3.35 is minimised when the level set contour $C = C_0$. Inspired by this, an initialisation scheme for the NBAAM is proposed, considering the NBAAM as a surface with thickness of 2 cm (1 cm either side of the prostate surface). The mean shape of the NBAAM is moved across the new image to find the initialisation location $P(x,y,z)$ by minimising the RIQF and NBAAM appearance difference. The cost function is minimised only when the model surface matches with the prostate surface in the new image. Unlike in Section 5.7, prostate volume variation is taken into account in this approach. A 17% volume variation was observed among the training data set and the initial shape of NBAAM were rescaled into 3 different volumes as 87%, 100% and 117% of the mean shape.

The searching algorithm proceeds in a coarse-to-fine manner as described in Figure 6.8. Firstly the mean shape is moved around the pelvis in a step size of $[10,10,10]$ to find top three $P_1(x,y,z)$ with the lowest RIQF difference. The mean shape is then rescaled into 87%, 100% and 117% and RIQF recalculated around location $P_1(x,y,z)$ with a smaller displacement step size $[3,3,3]$. The corresponding scale S and location $P_2(x,y,z)$ from the refined RIQF optimisation is stored and used as the input of the final refinement using a multi-scale NBAAM appearance with step size $[1,1,1]$, as shown in Figure 6.9. In Figure 6.9a and b, the mean shape was displaced around $P_2(x,y,z)$ and the appearance difference was calculated as 1039. In Figure 6.9c and d, the mean shape was rescaled to 87% and displaced around $P_2(x,y,z)$, the appearance difference was calculated as 671. In Figure 6.9e and f, the mean shape rescaled to 113% and displaced

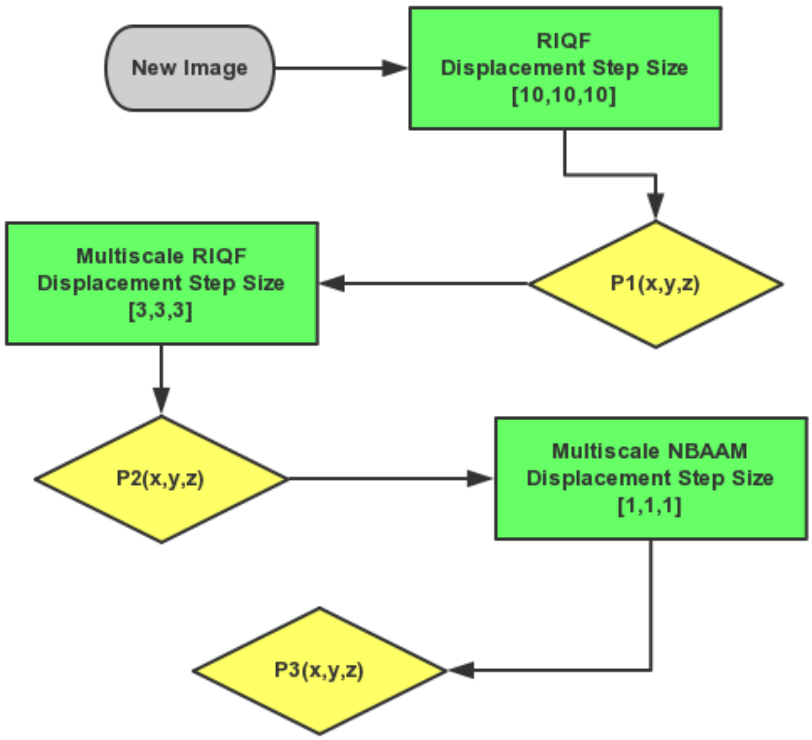

Figure 6.8: NBAAM coarse-to-fine initialisation scheme.

around $P_2(x,y,z)$, the appearance difference was calculated as 1322. Consequently, the scale 87% and the displacement of $P_3(x,y,z)$ is stored and used to initialise the NBAAM model.

6.5 Automatic Segmentation Using NBAAM

An AAM based segmentation seeks to match both the position of the model points and a representation of the appearance of the object to an image. The proposed NBAAM seeks to match the GTV contour and the appearance of the region near the GTV. In the segmentation of a new image, the mean shape or the scaled mean shape S_M is displaced into the image at $P_3(x,y,z)$.

Recall Section 3.48, the model parameters consisted of combined shape and appearance parameter c, translation parameter t and scaling parameter s. The initialisation discussed in Section 6.4 gives a reliable positioning of the model. Consequently, the translation parameter

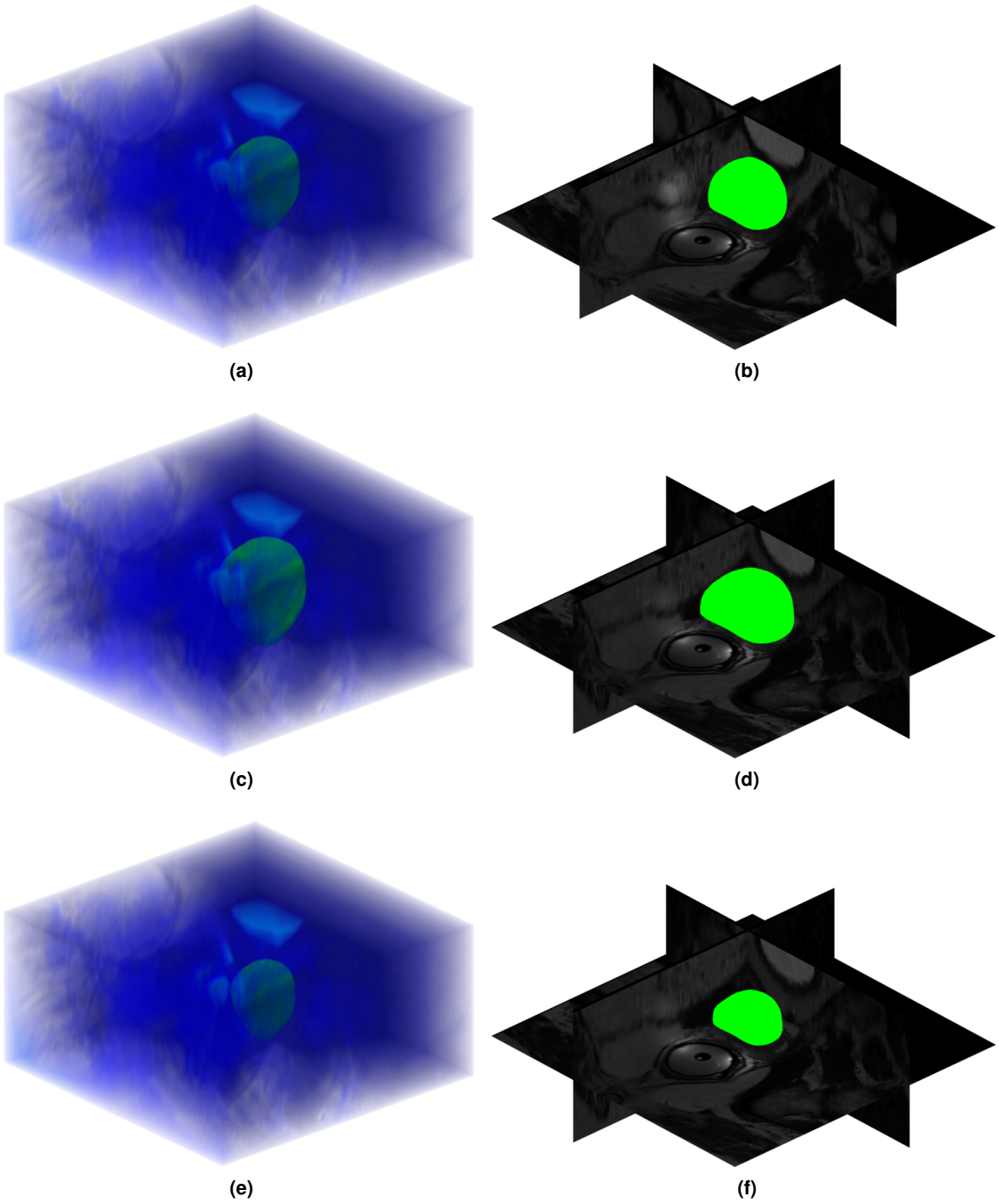

Figure 6.9: (a) and (b), mean shape displaced in $P_2(x,y,z)$, appearance difference calculated 1039. (c) and (d), mean shape rescaled to 87% and displaced in $P_2(x,y,z)$, appearance difference calculated 671. (e) and (f), mean shape rescaled to 113% and displaced in $P_2(x,y,z)$, appearance difference calculated 1322. The scale 87% and the displacement of $P_2(x,y,z)$ is stored and used to initialise the NBAAM model.

is eliminated in the NBAAM searching procedure. The model parameters update matrix R is obtained by calculating $\frac{\delta r}{\delta U}$ and substituting in Equation (3.53). Each parameter in U is perturbed from its optimal value with [-1, -0.5, 0.25, -0.1, 0.1, 0,25, 0.5, 1] standard deviations. $\frac{\delta r}{\delta U}$ is then calculated as the weighted average of the resulting appearance difference r caused by the 8 perturbations.

In the segmentation of a new image, the image appearance at the initialisation is extracted using S_E and warped to the shape free appearance patch. The appearance difference r is calculated and used to update the model parameter U by Equation (3.52). The model parameters are updated by with step size of k as:

$$U = U + k\delta U \tag{6.1}$$

The landmarks of the GTV are moved by updating the model parameters U; the new appearance difference is calculated as E'_G. If $E'_G < E_G$, the shape update is accepted, otherwise, a smaller $k = 0.5$ or $k = 0.2$ is tried. This procedure is repeated until no improvement in error E_G is found and convergence is assumed. The initialisation scheme introduced in Section 6.4 is considered as a pre-segmentation step, which provides a robust estimated location of the prostate and also a size of the volume. This results in fast converge of the NBAAM in the segmentation of new images, usually 3-5 iterations, as shown in Figure 6.10. The initialisation of the NBAAM takes an average time of 15 minutes and the segmentation of NBAAM converges in 2 minutes. An example of the NBAAM segmentation iterations is illustrated in Figure 6.10. It is worth noting that the color of the patch indicates the mesh distance (mm) between the ground truth segmentation and the evolving NBAAM shape.

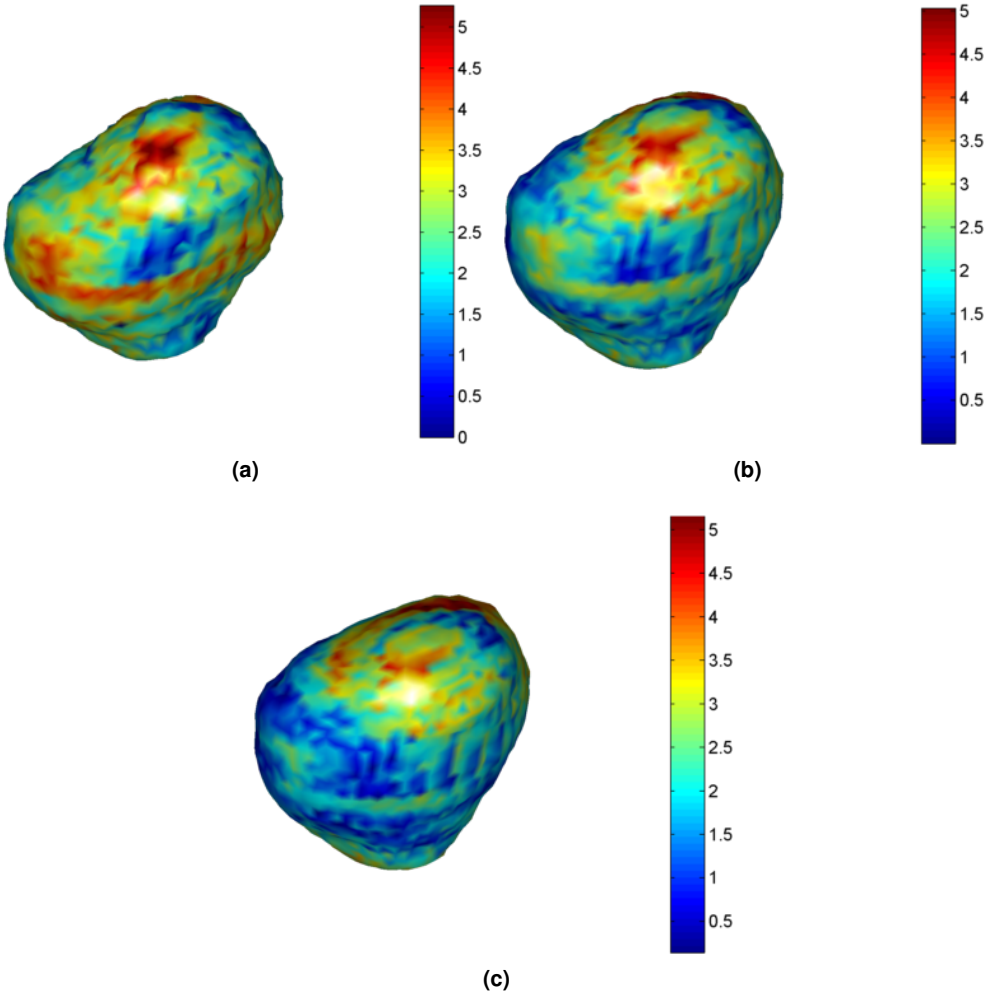

Figure 6.10: Distance meshes of 3 iterations of the NBAAM search against the clinical shape, the distance is calculated using a pairwise Euclidean distance (mm) based on the point correspondence. The mesh is coloured using this distance error. The NBAMM appearance difference for each iteration is (a) 491, (b) 311 and converged at (c) 197.

Table 6.4: Parameters Used in NBAAM

Paramet	Value	Information
n	2562	Number of points used to represent GTV
n_e	10	Landmark exterior displacement
n_i	5	Landmark exterior displacement
Box	[120, 80,100]	Texture warping box
n_{search}	20	Maximum number of iterations
$S(x,y,z)$	[17%,17%,17%]	Variation of volume scale
C	[1,0.5,0.2]	Step size of parameter update

6.6 Evaluation using DSC

Six test image volumes of different image resolutions (0.25/0.25/2.20, 0.625/0.625/3.60 and 0.39/0.39/3.30, 2 of each resolution), which have been excluded from the training set are used to evaluate the performance of the NBAAM. The performance of the segmentation is evaluated using DSC metric by comparing with the ground truth segmentation, summarised in Table 6.5. The segmentation shape was reconstructed into 2D contours for clarity. Figure 6.11 shows the

Case Number	Case 1	Case 2	Case 3	Case 4	Case 5	Case 6
Clinical Volume (cm^3)	45	42	28	87	65	58
MBAAM volume (cm^3)	44	45	32	77	65	62
Dice Coefficient	0.88	0.77	0.84	0.79	0.93	0.89

Table 6.5: The NBAAM segmentation performance evaluation by calculating DSC against the ground true segmentation.

comparison of clinical contour (blue) and NBAAM contour (red), the DSC of Figure 6.11a is 0.87 and the DSC of Figure 6.11b is 0.85.

6.7 Discussion

Comparing this work with the related work based on the conventional AAM application on prostate segmentation of Vincent et al ([155] overall mean DSC 0.88), the proposed NBAAM offers marginal improvement in segmentation performance at the prostate apex and base as shown in Figure 6.11 and Figure 6.12. The NBAAM results show the robustness at the weak GTV boundary at the prostate apex and base where the performance of conventional AAM significantly degenerate. This is due to the novel NBAAM appearance extraction and training scheme, which involves the bladder and rectum and uses them to drive the segmentation.

Another advantage of the NBAAM algorithms is that, the segmentation spares the bladder and rectum from the GTV volume effectively. The inhomogeneity of appearance caused by the involvement of rectum and bladder shown in Figure 6.7 has a strong influence on the appearance error E_G, which can be easily picked up by in the segmentation and used as the stopping criteria of the model deformation. With 1 cm interior to the patch, the inhomogeneity region of bladder and rectum will be excluded from the GTV definition.

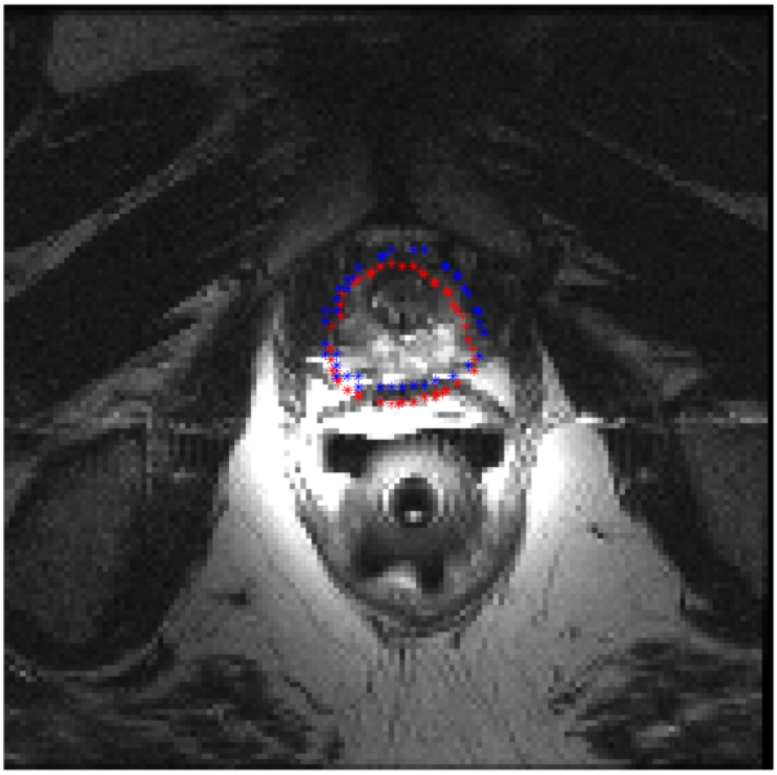

(a)

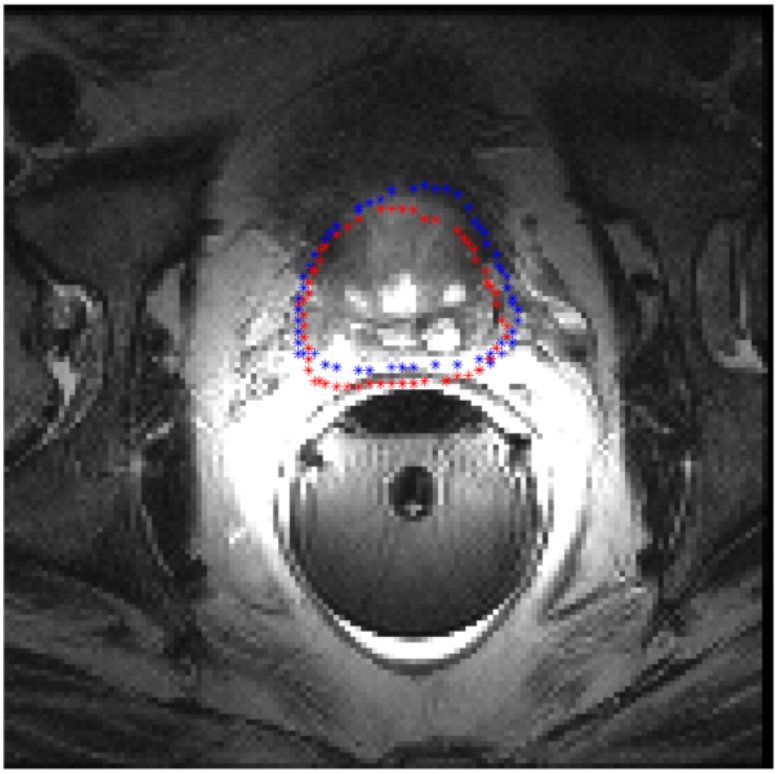

(b)

Figure 6.11: The segmentation results for (a) prostate base and (b) prostate apex. Red contour is the segmentation of NBAAM and blue contour is the clinical contour. The showing MRI is down-sampled from the original scan to [1,1,1] and the resolution is lost.

A draw back of the approach is that a contour shift towards the rectum is observed, as shown in Figure 6.11. This shift also influenced the middle area of prostate shape and result in a degradation in overall performance. The overall mean DSC of NBAAM was 0.85 with a large standard deviation of 0.06. This is considered as a "side effect" of the expanded appearance extraction. The contour somehow caused by the strong intensity field of the rectal coil, which usually have a intensity of 2000+, as shown in Figure 6.13. It is shown in Figure 6.2 that, the 1cm expansion of the NBAAM appearance patch involves this strong intensity field near the boundary of the S_E. In the segmentation of new images, the model may seek a region with this higher intensity as the stopping criteria in the model landmarks propagation. While the distance between the prostate and rectum varies, which results in the shift towards the rectum when the prostate and rectum are close. This influence is believed to be improved or completely resolved on a intra-patient data set, which has a comparatively fixed distance between prostate and surrounding structures and a consistent scanning protocol (with / without rectal coil).

6.8 Conclusion

The chapter introduces the NBAAM algorithms that can be applied to MRI images scans and automatically delineate the prostate GTV. The major advantage of the proposed NBAAM lies in the fast and reliable initialisation and the improved performance on prostate based and apex. The improved performance takes advantage of the anatomical structure in pelvis by expanding the appearance extraction 1cm to the GTV.

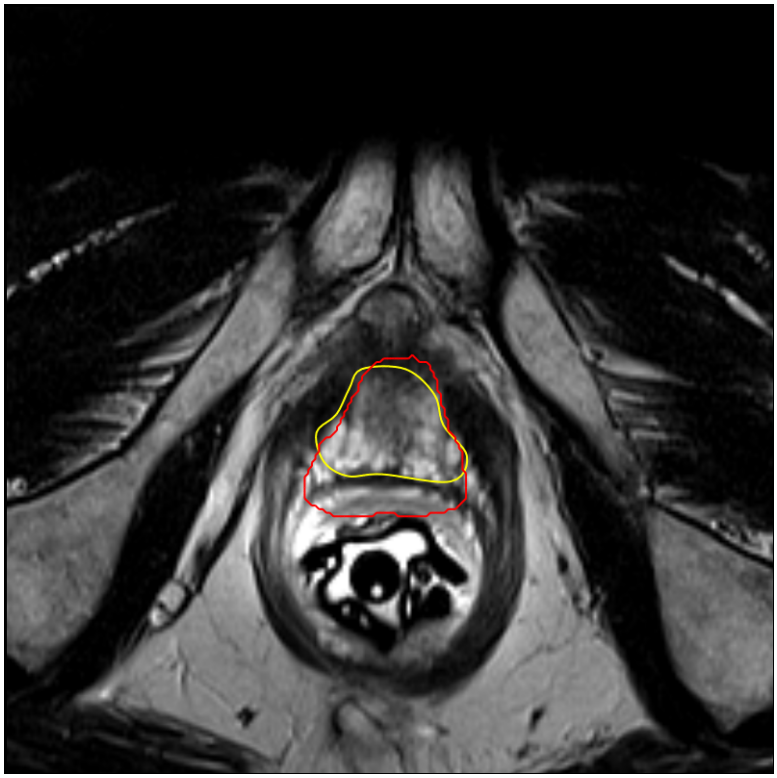

(a)

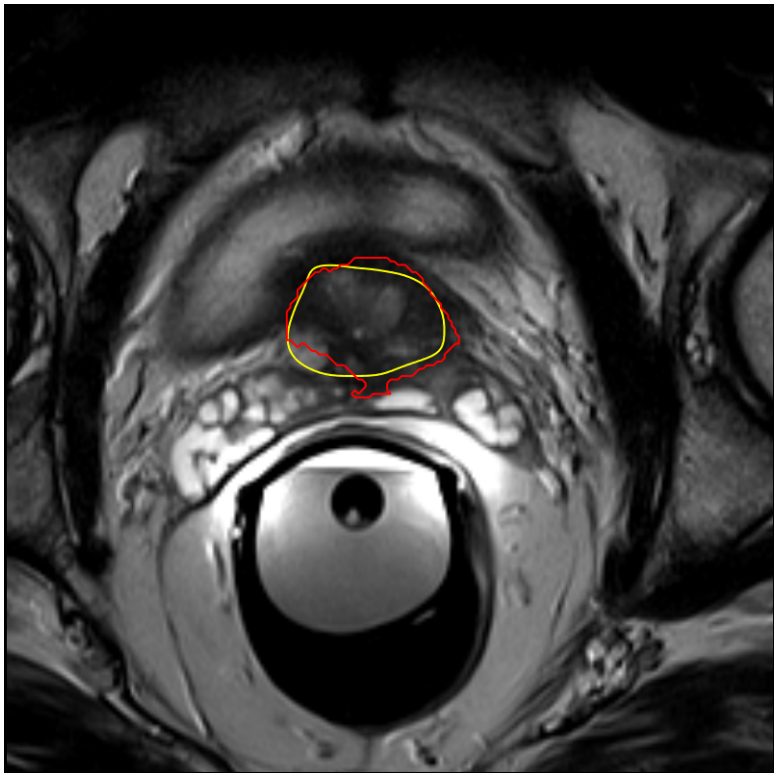

(b)

Figure 6.12: The segmentation results of Vincent et al. for (a) prostate base and (b) prostate apex. Red contour is the automatic segmentation and gold contour is the clinical contour [155].

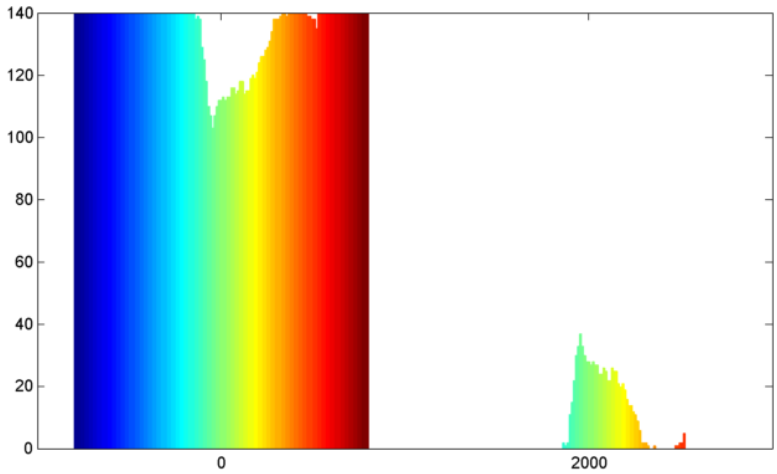

Figure 6.13: Image histogram of Figure6.11b, the rectal coil creates a much higher intensity region at around 2000.

Chapter 7

Conclusions

7.1 Summary

The thesis presents a series of automatic contouring algorithms for radiotherapy using deformable models, with preliminary results presented for a range of images and diseases. This research has the potential to reduce the inter- and intra-clinical variability in the delineation of the GTV in radiotherapy planning. The advantages of IGRT and IMRT can also be fully utilised by adding these algorithms into the system, providing the opportunity to contour the treatment day images in real time. The radiation dose can thus be more accurately and effectively delivered and improve the treatment outcome.

Chapter 1 of the thesis discussed the context of the research by connecting cancer radiotherapy and medical image analysis.

In Chapter 2, the background information of the thesis is described. CT MRI and PET were introduced as the major imaging modalities in radiotherapy, followed by the important anatomical information on the human brain and pelvis. Cancer diagnosis, staging, grading and treatment options were also discussed and IMRT and IGRT emphasised and the concept of CGRRT introduced as a future advancement of modern radiotherapy. The importance of an automatic contouring system in the CGRRT was also addressed.

Chapter 3 briefly reviewed image processing techniques related to this work, in particular segmentation was reviewed as a fundamental component of the process. Several low level segmentation methods were reviewed for their potential in the image pre-processing. Image features including first order distribution based features, GVF and image profiles were discussed. Image and point set registration methods were reviewed as registration based methods. Deformable models including FDMs and SCDMs were reviewed followed by their applications.

Chapter 4 demonstrated a LSM in the automatic delineation of high grade glima on brain MRI. The main contribution of this chapter was the series of low level image segmentation methodologies, reviewed in Section 3.3, cascaded to form a case-wise fully automatic initialisation pipeline for the level set function.

Chapter 5 starts with an new scheme of group-wise point registration for the correspondence definition of SCDMs. An ASM with an optimised feature searching profile, which takes into account the texture statistics of the prostate and surrounding organs, was implemented in the delineation of prostate GTV on CT. The optimised texture profiles showed their advantage over standalone pixel intensity, which is the contribution in this chapter.

In Chapter 6 fully automatic delineation algorithm of prostate GTV on MRI was proposed. The segmentation performance at the prostate base and apex area was shown to be improved by extending the appearance extraction 1 cm exterior the prostate shape. The novel appearance modelling scheme also spares the OARs from the GTV definition, which is the contribution in this chapter.

7.2 Conclusion

It can be concluded that deformable models including LSM, ASM and AAM have the ability to automatically delineate the GTV in brain and prostate radiotherapy. Depending on the disease and imaging modality, an accurate GTV definition is achievable by utilising the appropriate deformable model and pre-processing techniques. An automatic and accurate GTV definition can reduce inter- and intra-clinical variability and fully facilitate IGRT and IMRT, resulting in an improved radiotherapy outcome.

The work in this thesis focused on segmentation accuracy, which fits nicely to the new radiotherapy framework of CGRRT proposed in Section 2.5.4. In the delineation of glioma GTV on MRI, the most time efficient LSM algorithm of CL model [20] was employed, initialised using a fast but reliable active thresholding method. The ASM segmentation of prostate GTV on CT image uses a texture optimisation scheme to overcome the poor resolution of CT, first order distribution statistics is used instead of computationally expensive higher order statistics to ensure the segmentation can be obtained in almost real time. The NBAAM method improved

the segmentation at the prostate apex and base by extending the appearance extraction 1 cm exterior to the GTV, which is usually done by a coupled segmentation of prostate and bladder or rectum [98, 31]. The training of SCDMs including ASM and NBAAM was done in the offline phase, while the segmentation phase takes only a few minutes. The time efficiency of SCDMs can be further increased in the intra-case studies, the training of a much smaller data set can be done in real time and used immediately to match radiotherapy plans to OBI images. This has the potential to eliminate the work of patient immobilisation and take advantage of four-dimensional radiation therapy (4DRT) [164].

With the progress in the applications of deformable models, the CGRRT framework (Figure 2.13) can be extended as shown in Figure 7.1. Firstly, the new CGRRT is a unified framework for all medical imaging modalities, for example CT, MRI, CBCT, PET and TRUS and not limited to radiotherapy. For a specific modality and disease, a corresponding deformable model is optimised and employed in the automatic contouring. In the planning stage, a inter-patient deformable model containing larger variation is constructed, in which, clinical input including patient specific information, stage and grade of the disease, ground truth segmentation (SCDMs) are imported into the system. The priority of the inter-patient contouring system is accurate and robust against large shape and appearance variation. Treatment day images from previous fractions are stored and used to construct a patient-oriented automatic contouring system of the intra-patient data. The intra-patient contouring system utilises a time-efficient deformable model because of the significantly smaller shape and appearance variation. The clinical input imported into intra-patient contouring system could be more patient specific, for example biopsy data, faction interval length and treatment dose etc. The priority of the intra-patient contouring lies in the time efficiency, the segmentation need be done in real time to fully utilise the advantage of IGRT and IMRT.

The pilot results of Chapter 4, Chapter 5 and Chapter 6 shows the potential of deformable models in the contouring of brain and prostate cancer GTV. Leveraging the increasing accuracy, automatic contouring systems based on deformable models have the potential to assist clinicians define the extent of radiotherapy tumour volume in a reliable and repeatable manner. The further development of automatic contouring, particularly real time automatic contouring

is essential for the next generation of modern radiotherapy, probably the CGRRT.

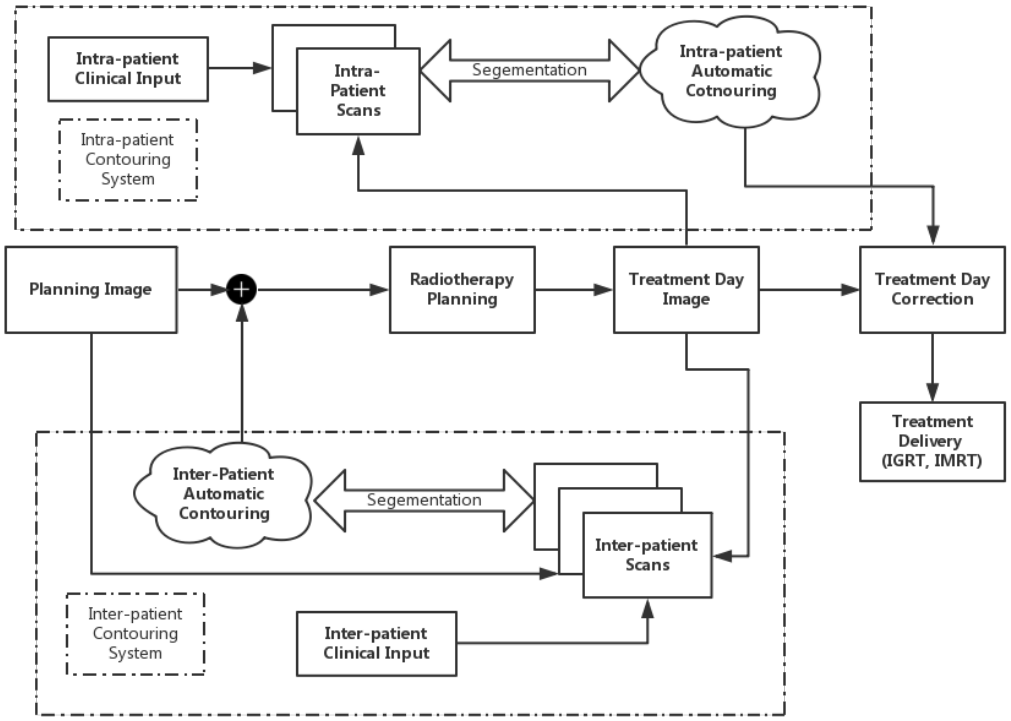

Figure 7.1: The extended CGRRT workflow.

7.3 Future work

Until today, manual contouring is still the first choice in the planning of radiotherapy, although it has many disadvantages. There is no doubt that the automatic contouring systems cannot replace the oncologist at this stage. The major reason for this is that experience oncologists have a perfect merge of clinical, pathological, anatomical and medical imaging knowledges which optimises contouring of the GTV. While the reproducibility, adaptability and time efficiency will make the automatic contouring a major future development in the next generation radiotherapy.

In the future more clinical and pathological information will be merged into the construction of deformable models. An anatomical atlas can be used to overcome the local minimum issue of FDMs. Staging, grading, and biopsy information may significantly improve the accuracy,

robustness and efficiency of the initialisation, particular for a inter-patient planning. Patient specific information, for example age, gender and treatment history, are also valuable for improving the efficiency of intra-patient planning update.

Additionally, a much larger data set contoured by multiple observers has the potential to improve the model significantly. Leveraging the development of computational power and storage, particularly cloud computing technology, the training data now can be not limited to a single cancer centre but available worldwide.

Moreover, the accuracy of contouring for radiotherapy planning need be further improved, particularly on CT images. Higher order image features have the potential to achieve that, at the cost of more computational time.

Finally, more research is required to adapt the contouring system to other popular modalities and registered modalities. The utilisation of features of different modalities is also useful in the development towards an CGRRT radiotherapy framework.

Appendix A

Publications

- Cheng K, Montgomery D, Feng Y, Steel R, Liao H, McLaren DB, Erridge SC, McLaughlin S, Nailon WH. Identifying Radiotherapy Target Volumes in Brain Cancer by Image Analysis. Healthcare Technology Letters, Volume 2, Issue 5, October 2015, p. 123 âĂŞ 12.
- Feng Y, Welsh D, McDonald K, Carruthers L, Cheng K, Montgomery D, Lawrence J, Argyle DJ, McLaughlin S, McLaren DB, H. Nailon WH. Identifying the Dominant Prostate Cancer Focal Lesion using Image Analysis and Planning of a Simultaneous Integrated SABR Boost. Acta Oncologica, 54.9 (2015): 1543-1550.
- Cheng K, Feng Y, Montgomery D, Steel R, Liao H, McLaren DB, McLaughlin S, Nailon WH. Active Shape Models for Prostate Cancer Planning with Optimized Features. In Proc of the International Society for Optics and Photonics (SPIE) 2014, San Diego.
- Feng Y, Cheng K, Lawrence Y, Forrest L, McLaren DB, McLaughlin S, Argyle DJ, Nailon WH. A new image registration framework for improving radiotherapy delivery. In Proc of Symposium on Small Animal RadioTherapy, 3rd-5th March 2013, Maastricht, the Netherlands.
- Montgomery D, Campbell, S, Cheng K, Feng Y, Murchison J, McLaren DB, Yong AW, Ritchie G, McLaren DB, Erridge SC, McLaughlin S, Nailon WH. Predicting the occurrence of radiation induced pneumonitis by texture analysis of CT images from lung cancer patients. In: MICCAI Workshop on Pulmonary Image Analysis, MICCAI 2013.
- Cheng K, Feng Y, Steel R, McLaren DB, Erridge SC, McLaughlin S, Nailon WH. Level set identification of radiotherapy target volumes on magnetic resonance images. In Proc of 5th of International Conference on Advances in Medical Signal and Information Processing (MEDSIP). Liverpool, UK, 5th-7th July 2012.

- Feng Y, Cheng K, Tian Y, McLaren DB, McLaughlin S, Argyle D, Nailon WH. Scale invariant image registration for focal treatment of prostate cancer by radiotherapy. In Proc of 5th International Conference on Advances in Medical Signal and Information Processing (MEDSIP). Liverpool, UK, 5th-7th July 2012

Identifying Radiotherapy Target Volumes in Brain Cancer by Image Analysis

Kun Cheng[1], *Dean Montgomery*[1], *Yang Feng*[1], *Robin Steel*[1], *Hanqing Liao*[2], *Duncan B McLaren*[3], *Sara C Erridge*[3], *Stephen McLaughlin*[4], *William H Nailon*[1,5]

[1] *Department of Oncology Physics, Western General Hospital, Crewe Road South, Edinburgh, EH4 2XU, UK.*
[2] *Department of Electrical Engineering and Electronics, the University of Liverpool, Liverpool, L69 3GQ, UK.*
[3] *Department of Radiation Oncology, Western General Hospital, Crewe Road South, Edinburgh, EH4 2XU, UK.*
[4] *School of Engineering and Physical Sciences, Heriot Watt University, David Brewster Building, Edinburgh, EH14 4AS, UK.*
[5] *School of Engineering, the University of Edinburgh, the King's Buildings, Mayfield Road, Edinburgh, EH9 3JL, UK.*
E-mail: W.Nailon@ed.ac.uk

Published in Healthcare Technology Letters; Received on xxx; Revised on xxx.

Background To establish the optimal radiotherapy fields for treating brain cancer patients the tumour volume is often outlined on magnetic resonance (MR) images, where the tumour is clearly visible, and mapped onto computerised tomography (CT) images used for radiotherapy planning. This process requires considerable clinical experience and is time consuming, which will continue to increase as more complex image sequences are used in this process.
Purpose Here the potential of image analysis techniques for automatically identifying the radiation target volume on MR images, and thereby assisting clinicians with this difficult task, was investigated.
Material and Methods A gradient-based level set approach was applied on the MR images of five patients with grade II, III and IV malignant cerebral glioma. The relationship between the target volumes produced by image analysis and those produced by a radiation oncologist was also investigated.
Results The contours produced by image analysis were compared with the contours produced by an oncologist and used for treatment. In 93% of cases the Dice similarity coefficient was found to be between 60% and 80%.
Conclusions This feasibility study demonstrates that image analysis has the potential for automatic outlining in the management of brain cancer patients, however, more testing and validation on a much larger patient cohort is required.

1. Introduction: Radiotherapy is the core treatment modality in the management of high and low grade glioma but the radiation doses required to optimise local control have the potential to affect adjacent normal tissues [15, 16, 12]. Consequently, accurate delineation of the radiotherapy target is particularly important. A number of studies have been performed that highlight the challenges of delineation of the gross tumour volume (GTV) and clinical target volume (CTV) in patients with brain cancer [25, 26, 11, 19, 43]. Not only does the abnormality on the radiotherapy planning CT and registered MR images need to be accurately defined, but also the areas of likely anatomic spread need to be appreciated. The level of difficulty faced by clinicians in carrying out this task is evident in Figure 1. This shows the extent of grade II, (left), grade III (middle) and grade IV (right) gliomas on MR images where disease can be identified, and on CT where it is more difficult to identify. At present clinicians must use their experience to define the GTV or CTV from analysis of both data sets, a process that is complicated by the fact that the size and shape of the GTV may appear different, sometimes quite significantly, depending on the imaging modality used to visualise the tumour [21, 22]. As a result, significant variability has been reported in the manual segmentation of brain tumours: intra-rater, $20 \pm 15\%$; inter-rater, $28 \pm 12\%$ [29].

Image analysis approaches have the potential to assist clinicians with this difficult task by improving the consistency of target delineation and providing solutions for automatic segmentation of intra-cranial structures on MR image volumes. This has received considerable attention over the past two decades with comprehensive coverage of the important contributions in the field prior to 2007 available in [1]. Contributions thereafter until the present day can be found in [3]. One commonly used method for segmenting intra-cranial MR image structures is to register to an anatomical atlas that contains information on the general shape and form of the structures of interest. By projecting the MR image structures available from the atlas onto the MR image volume under investigation, segmentation is performed [44, 14]. Prastawa et al adopted this approach by first registering to an atlas of healthy brains in their framework for automatically segmenting brain tumours on MR image volumes [33]. Cuadra et al used a similar approach by first registering to an atlas and including a model of lesion growth. The method proved useful in the segmentation of grossly deformed cerebral structures [13]. Wang et al also used prior probabilities from the International Consortium for Brain Mapping (ICBM) together with normalised Gaussian mixture models (NGMM) of grey and white matter and cerebrospinal fluid to establish a Gaussian Bayesian classifier (GBC). The GBC was used to initialise a three-dimensional (3D) fluid vector flow (FVF) algorithm, which was used for brain tumour segmentation [40]. The approach was validated on publicly available datasets and the Tanimoto distance metric used to assess performance. The findings reported closely matched those of Corso et al [10].

When a suitable atlas is not available, as is generally the case with tumour segmentation, pixel- or voxel-based methods such as level sets [20] or active contour based approaches [45] can be used. However, these methods require careful initialisation to avoid propagation across weak or missing boundaries, as shown in Figure 2 (left) [36]. Here we present the preliminary findings of a pilot study investigating a level set-based approach, which uses limited prior information, for the segmentation of the significant tumour volume, or GTV, on the MR images of five brain cancer patients. Using this approach the GTV could then be mapped to the corresponding CT for radiotherapy planning.

Acta Oncologica, 2015; 54: 1543–1550

Taylor & Francis
Taylor & Francis Group

ORIGINAL ARTICLE

Identifying the dominant prostate cancer focal lesion using image analysis and planning of a simultaneous integrated stereotactic boost

YANG FENG[1], DANIEL WELSH[1], KIM MCDONALD[1], LINDA CARRUTHERS[1], KUN CHENG[1], DEAN MONTGOMERY[1], JESSICA LAWRENCE[5], DAVID J. ARGYLE[5], STEPHEN MCLAUGHLIN[4], DUNCAN B. MCLAREN[2] & WILLIAM H. NAILON[1,3]

[1]*Department of Oncology Physics, Edinburgh Cancer Centre, Western General Hospital, Crewe Road South, Edinburgh, UK,* [2]*Department of Clinical Oncology, Edinburgh Cancer Centre, Western General Hospital, Crewe Road South, Edinburgh, UK,* [3]*School of Engineering, the University of Edinburgh, the King's Buildings, Mayfield Road, Edinburgh, UK,* [4]*School of Engineering and Physical Sciences, Heriot Watt University, Edinburgh, UK and* [5]*Royal (Dick) School of Veterinary Studies, University of Edinburgh, Edinburgh, UK*

ABSTRACT

Background. Prostate cancer is now the only solid organ cancer in which therapy is commonly applied to the whole gland. One of the main challenges in adopting focal boost or true focal therapy is in the accurate mapping of cancer foci defined on magnetic resonance (MR) images onto the computerised tomography (CT) images used for radiotherapy planning.

Material and methods. Prostate cancer patients (n = 14) previously treated at the Edinburgh Cancer Centre (ECC) were selected for this study. All patients underwent MR scanning for the purpose of diagnosis and staging. Patients received three months of androgen deprivation hormone therapy followed by a radiotherapy planning CT scan. The dominant focal prostate lesions were identified on MR scans by a radiologist and a novel image analysis approach was used to map the location of the dominant focal lesion from MR to CT. An offline planning study was undertaken on suitable patients (n = 7) to investigate boosting of the radiation dose to the tumour using a stereotactic ablative body radiotherapy (SABR) technique.

Results. The non-rigid registration algorithm showed clinically acceptable estimates of the location of the dominant focal disease on all CT image data of patients suitable for a boost treatment. Standard rigid registration was found to produce unacceptable estimates of the dominant focal lesion on CT. A SABR boost dose of 47.5 Gy was delivered to the dominant focal lesion of all patients whilst meeting all dose-volume histogram (DVH) constraints. Normal tissue complication probability (NTCP) for the rectum decreased from 1.28% to 0.73% with this method.

Conclusions. These preliminary results demonstrate the potential of this image analysis method for reliably mapping dominant focal disease within the prostate from MR images onto planning CT images. Significant dose escalation using a simultaneous integrated SABR boost was achieved in all patients.

Prostate cancer, which accounts for 25% of new male cancers, is now the only solid organ cancer in which therapy is applied to the whole gland [1]. Traditionally whole gland ablative treatment with radiotherapy or surgery has been utilised due to the perception that disease is multifocal within the prostate. There has however been significant progress in detecting localised low-risk prostate cancer through prostate-specific antigen (PSA) screening and in identifying its location within the prostate gland using trans-rectal biopsies, template mapping biopsies and multi-parametric MR imaging. Identification of early disease with small dominant focal volumes opens up the possibility of truly focal treatment of the cancer within the prostate using techniques, such as radiotherapy, thus preserving genitourinary and rectal function in low- to moderate-risk prostate cancer patients [2]. Alternatively a boost may be applied to the tumour whilst a tumouricidal lower dose is delivered to the rest of the prostate gland providing that dose constraints to the

Correspondence: W. H. Nailon, Department of Oncology Physics, Edinburgh Cancer Centre, Western General Hospital, Crewe Road South, Edinburgh EH4 2XU, UK. Tel: + 44 131 5373560. Fax: + 44 131 5371092. E-mail: W.Nailon@ed.ac.uk

(Received 15 May 2015; accepted 15 June 2015)

ISSN 0284-186X print/ISSN 1651-226X online © 2015 Informa Healthcare
DOI: 10.3109/0284186X.2015.1063782

Active Shape Models with Optimized Texture Features for Radiotherapy Planning of Prostate Cancer

K. Cheng[1], Y. Feng[1], D. Montgomery[1], D.B. McLaren[1], S. McLaughlin[2], W.H. Nailon[1]
[1]Edinburgh Cancer Centre, Western General Hospital, Edinburgh, UK
[2]School of Engineering and Physical Sciences, Heriot-Watt University, Edinburgh, UK

Abstract

There is now considerable interest in radiation oncology on the use of shape models of anatomy to improve target delineation and assess anatomical disparity at time of radiotherapy. In this paper a texture based active shape model (ASM) is presented for automatic delineation of the gross tumor volume (GTV), containing the prostate, on computed tomography (CT) images of prostate cancer patients. The model was trained on two-dimensional (2D) contours identified by a radiation oncologist on sequential CT image slices. A three-dimensional (3D) GTV shape was constructed from these and iteratively aligned using Procrustes analysis. To train the model the shape deformation variance was learnt using the Active Shape Model (ASM) approach. In a novel development to this approach a profile feature was selected from pre-computed texture features by minimizing the Mahalanobis distance to obtain the most distinct feature for each landmark. The interior of the GTV was modelled using quantile histograms to initialize the shape model on new cases. From the archive (num=42) of contoured CT scans 32 cases were randomly selected for training and 10 for evaluating performance. The gold standard was taken as the contour defined by the radiation oncologist. The shape model achieved an overall dice coefficient of 0.81 for all test cases. Performance was found to increase, mean DC of 0.87, when the volume size of the new case was similar to the mean shape of the model. With further work the approach has the potential to be used in real-time delineation of target volumes.

Description of purpose

Prostate cancer accounts for approximately 14% of all cancers diagnosed in men. External beam radiotherapy remains an important curative treatment for prostate cancer and with the incidence of disease set to rise through greater prostate-specific antigen (PSA) testing, an aging population and fewer competing causes for death, it is imperative to maximize the efficiency of treatment. There is a growing interest in radiation oncology on the use of models of anatomy, which contain information about the expected shape and appearance of structures of interest, to assist in the segmentation of different anatomical structures. Automatic segmentation in this way has the potential to increase accuracy and be used on images acquired at time of radiation treatment where it is vital that any analysis is done as quickly as possible to ensure that the patient does not move. ASMs have been widely used in medical image analysis for delineation of lungs, heart and pelvic organs. However, shape models of the GTV used in radiotherapy planning of the prostate have not been constructed due to large variations in patient shape and appearance. This is further complicated by the close proximity of the prostate to the bladder and rectum. In the proposed scheme an ASM with an optimised

SYMPOSIUM ON SMALL ANIMAL RADIOTHERAPY

ABSTRACT

Abstract title: **A NEW IMAGE REGISTRATION FRAMEWORK FOR FOCAL TREATMENT OF PROSTATE CANCER BY RADIOTHERAPY**

Authors: Y. Feng (1), K. Cheng (1), J. Lawrence (3), L. Forrest (4), D.B. McLaren (1), S. McLaughlin (2), D.J. Argyle (3), W.H. Nailon (1)

Affiliations :

(1) Edinburgh Cancer Centre, Western General Hospital, Edinburgh, EH4 2XU, UK

(2) School of Engineering and Physical Sciences, Heriot Watt University, Edinburgh, EH14 4AS, UK

(3) The Royal (Dick) School of Veterinary Studies, Edinburgh, EH25 9RG, UK

(4) The University of Wisconsin-Madison School of Veterinary Medicine, Madison, WI, USA

Email address presenting author: **s1031630@sms.ed.ac.uk**

Introduction:

Image registration is the process of aligning two or more images of the same scene acquired at different times, viewpoints, and/or by different sensors. A registration framework was designed to include both a rigid registration algorithm based on the scale invariant feature transform (SIFT) and mutual information (MI), and a non-rigid registration algorithm based on manually defined features and robust similarity function. This method has been developed to register multi-modality image data from computed tomography (CT), magnetic resonance (MR) and histology to plan focal radiotherapy of the prostate. Our hypothesis is that this framework is suitable for other multi-modality image registration problems.

Materials & Methods

SIFT is a method that can find key points and their descriptors in scale space and extract robust image features. Calculation of the MI of these features is a powerful indicator of image match. In the approach developed a rigid registration algorithm extracts feature points from the reference and target image data based on the SIFT algorithm and finds the best affine match by optimizing the MI of the SIFT features. Next a non-rigid registration algorithm is applied that uses the Euler distance between contour points and the MI between pathologically identified points as a robust similarity function. A fuzzy-to-deterministic approach is used to establish the match between feature points and a cubic B-spline method is applied after non-rigid transform. A posteriori weights for different data sets are used to adjust the similarity function and optimisation performed using simulated annealing and the Broyden–Fletcher–Goldfarb–Shanno (L-BFGS) method. Rigid registration performance was assessed using CT and MR image data acquired on the Radionics Phantom 2 (Radionics, Inc., Burlington, MA), a geometric verification phantom used for quality assurance in stereotactic radiotherapy. EPID and DRR images acquired from human prostate cancer patients were used. The non-rigid registration algorithm has been assessed on manually warped test images. The whole framework is additionally being tested on contemporaneous CT and MR series from dogs with sinonasal tumours.

Results

The mean error of the rigid method applied on the phantom data was less than 1.5% and was 10x faster than conventional MI-based registration. EPID and DRR images were registered within clinically acceptable limits. The similarity function provided a clear peak at the position of the best match between the reference and target images.

Conclusion

The rigid and non-rigid registration algorithms developed performed well on test image data. Preliminary evaluation supports the use of this framework for registration of canine nasal tumour CT and MR images and may prove useful in other tumour types. This approach is currently being investigated to establish the widespread applicability in radiation therapy.

Tick this box if you would prefer a poster ☐

Predicting the Occurrence of Radiation Induced Pneumonitis by Texture Analysis of CT Images from Lung Cancer Patients

Dean Montgomery*[1], Sorcha Campbell[2], Kun Cheng[1], Yang Feng[1], John Murchison[3], Ai Wain Yong[3], Gillian Ritchie[3], Duncan B McLaren[2], Sara C Erridge[2], Stephen McLaughlin[4], and William H Nailon[1]

[1] Department of Oncology Physics, Western General Hospital, Edinburgh and the University of Edinburgh
[2] Department of Radiation Oncology, Western General Hospital, Edinburgh
[3] Department of Radiology, Royal Infirmary of Edinburgh, Edinburgh
[4] School of Engineering and Physical Sciences, Heriot Watt University

Abstract In 13-37% of cases, lung cancer patients treated with radiotherapy suffer from radiation induced lung disease, such as radiation induced pneumonitis. Three dimensional (3D) texture analysis, combined with patient-specific clinical parameters, were used to compute unique features (n=2138). Principal component analysis (PCA) was used to remove highly correlated features and a series of support vector machines (SVM) were used for classification in a leave one out scheme. On radiotherapy planning CT data of 57 patients, (14 symptomatic, 43 asymptomatic), the classifier obtained an area under the receiver operating curve of 0.873 with sensitivity, specificity and accuracy of 92%, 72% and 87% respectively. The combination of texture and clinical features demonstrates a statistically significant performance increase over the use of the clinical features alone. With further development the approach has the potential to be used to predict the likelihood of patients developing radiation induced pneumonitis in a clinical environment.

1 Introduction

Over the last two decades lung cancer has accounted for the majority of cancer attributable deaths and in Scotland the incidence of lung cancer is amongst the highest in the world [7,12]. Patients with stage I and stage II disease are treated with radical radiotherapy if they are inoperable or decline surgery. For stage III disease radical radiotherapy often combined with chemotherapy is the treatment of choice. The exposure of lung tissue to ionising radiation during radiotherapy can lead to physiological changes in the lung tissues and subsequently, radiation induced lung injury. Radiation induced pneumonitis develops in 13-37% of

* This work is generously supported by NHS Lothian, Edinburgh and Lothian Health foundation (charity number SC007342), the James Clerk Maxwell Foundation, the Jamie King Uro-Oncology Endowment Fund and Darwin Awards from the University of Edinburgh.

LEVEL SET IDENTIFICATION OF RADIOTHERAPY TUMOUR VOLUMES ON MAGNETIC RESONANCE IMAGES (MEDSIP12)

K. Cheng[1], Y.Feng[1], R.Steel[1], D.B. McLaren[1], S.Erridge[1], S. McLaughlin[2], W.H. Nailon[1]
[1]Edinburgh Cancer Centre, Western General Hospital, Edinburgh, UK
[2]School of Engineering and Physical Science, Heriot-Watt University, Edinburgh, UK

Introduction

Gliomas are the most common primary brain tumours with an incidence of six to eight in 100,000. Grade I (benign) gliomas are slow growing with good survival after total resection. Grade II (malignant) to Grade IV (highly malignant) tumours are more diffuse and aggressive and associated with poor prognosis [1]. Radiotherapy is applied after complete tumour resection to ensure that any remaining cancerous tissue is treated. It is therefore essential that the gross tumour volume (GTV) is accurately defined to preserve the immediate and long-term function of the central nervous system from the effects of radiation. This is a complex and specialist process that is further complicated by the fact that the size and shape of the GTV may appear different, sometimes significantly, depending on the imaging modality used to visualize the tumour (e.g. Computerised Tomography (CT) or Magnetic Resonance (MR) imaging). Here we present preliminary findings of an approach, using limited prior information, for segmentation of radiotherapy planning MR images. The approach developed is based on Chunming Li's variational level set formulation of the active contour without re-initialization [2].

Methodology

Here, a level set-based algorithm was applied in three stages to identify the GTV on MR images of brain cancer patients [2]. In the first stage a coherence enhanced diffusion filter with optimised rotation invariance [3] was applied to remove noise whilst preserve edge information, as shown in Fig.1. Edge information significantly affects level set evolution because boundary leakage may occur when the level set function encounters weak edge points. In the second stage intensity information was extracted from contoured MR images as prior information. An intensity interval was set to construct binary images containing possible tumour regions as well as comparatively smaller unaffected brain regions. The threshold was updated for each MRI slice, based on the statistics of potential tumour region, a technique more commonly known as active thresholding. A morphological opening kernel was applied to the binary images to remove the non-cancerous regions and preserve the integrity of the significant tumour region. The centroid of GTV on previous slice was incorporated as a constraint to keep the morphological operation robust to all MRI slices. In the final stage a signed distance function was constructed from the tumour region located in the second stage and the level set evolution, based on the Chunming Li approach, started. This method is based on the variational level set formulation of the active contour without re-initialization. This formulation consists of an internal energy term, which eliminates the need for re-initialization by penalizing the deviation of the level set function by a signed distance function, and an external energy that drives the motion of the zero level set contour to the potential tumour contour. This level set model is computationally more efficient than the classic level set method and insensitive to weak boundaries and noise [2]. The whole identification algorithm is presented in Fig.2.

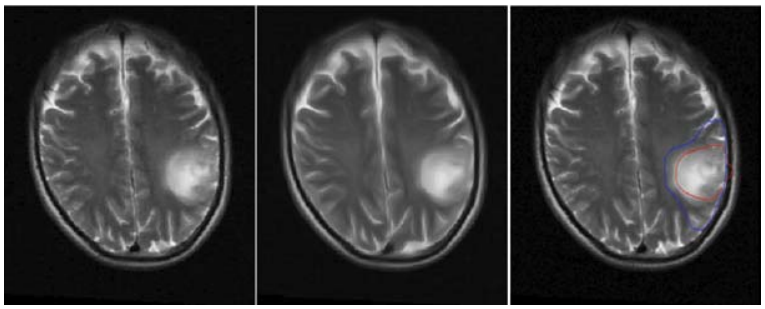

Fig(1). Left: Result of smoothing the MR image data using a Gaussian filter. Middle: Result of smoothing using a coherence enhanced diffusion filter. Right: The level set contour obtained when the Gaussian smoothed (left image) was used as input (red line: level set contour, blue line: GTV). Significant contour leakage results because of the weak edge gradients produced by the Gaussian smoothing kernel.

Scale Invariant Image Registration for Focal Treatment of Prostate Cancer by Radiotherapy

Y. Feng[1], K. Cheng[1], Y. Tian[1], D.B. McLaren[1], S. McLaughlin[2], D.J. Argyle[3], W.H. Nailon[1]
[1]Edinburgh Cancer Centre, Western General Hospital, Edinburgh, UK
[2]School of Engineering and Physical Sciences, Heriot Watt University, Edinburgh, UK
[3]The Royal (Dick) School of Veterinary Studies, Edinburgh, UK

Introduction: Structural and functional imaging can provide disease-specific insights and assist in the management of cancer patients. In radiotherapy of the prostate, computerized tomography (CT) images are acquired to provide structural information and electron density information for dose calculation [1]. Positron emission tomography (PET) images and/or magnetic resonance (MR) images provide functional information to identify the biological features of tumour regions [2]. Planning CT data can be reconstructed to form digital reconstructed radiographies (DRR) which are direct representation of the planned treatment position [3]. Electronic portal imaging devices (EPID) provide a view of the patient at the treatment position. Mapping EPID images to DRR images will ensure that the patient is positioned in the correct location for treatment. However, it is difficult to map the information in images on different modalities. Image registration is the process of aligning two or more images of the same scene acquired at different times, viewpoints, and/or by different sensors [4]. In this paper a rigid registration method based on the scale invariant feature transform (SIFT), and mutual information (MI) approach, is presented. This method has been developed to register multi-modality image data from CT, MR, DRR and EPID to plan focal radiotherapy of the prostate. However, it is suitable for other multi-modality image registration problems.

Methodology: Matching common features in the source and target image can reduce computation in an image registration approach. However, it is difficult to identify suitable features acquired on different modalities because of differences in resolution, scale and position. SIFT is a method that can find key points and their descriptors in scale space and extract robust image features. Calculation of the mutual information of these features is a powerful indicator of image match. The method presented contains four stages: pre-processing; feature extraction with SIFT; calculation of MI; and optimization. The pre-processing stage includes segmentation of the regions of interest, de-noising, resampling of the original data set and the down-sampling of the resulting images. Each pre-processed image was selected as a flow data set and SIFT features extracted. The SIFT threshold for feature extraction was set to generate 50 features on every image slice. Therefore the problem of physical background and reconstruction field background pixels, which can significantly affect the accuracy of the MI-based method, was removed [5]. An affine transform was applied to the flow data set to alter the position of the features. The MI of the key feature points on the source image and the neighbouring points on the target image were calculated using (1), where P_A and P_B are the marginal, and P_{AB} the joint, probability distributions.

$$I(A,B) = \sum_{a,b} P_{AB}(a,b) \log \frac{P_{AB}(a,b)}{P_A(a) * P_B(b)} \quad (1)$$

Simulated annealing optimization was performed on the 7-dimensional parameter space (T_x T_y T_z α β γ scale) over a 1 pixel, 1° interval to find the global maximum representing the best match.

Results: Registration performance was assessed using CT and MR image data acquired on the Radionics Phantom 2 (Radionics, Inc., Burlington, MA), a geometric verification phantom that is used for quality assurance in stereotactic radiotherapy. The CT and MR data were mapped with an average error rate of 1.5% (Figure 1). The method was found to be x10 faster than conventional MI-based registration because fewer feature points are acquired (figure 2). EPID and DRR images from patients with prostate cancer are included in the test data as well. They can be appropriately registered as shown in figure 3.

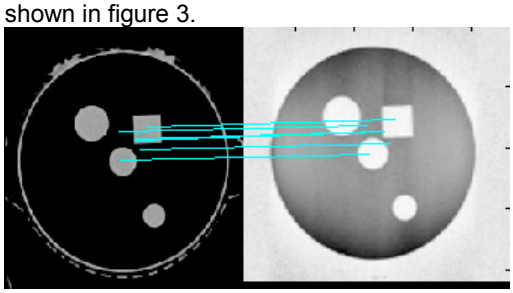

	T_x	T_y	T_z	α	γ	β
Actual	0	0	0	90	-90	0
Calculated	0	0	9	90	-90	0
Shift Range	100	100	100	/	/	/
Rotation Range	/	/	/	180	180	180
Error Rate	0	0	9%	0	0	0
Average Error Rate	1.5%					

Figure 1. Left: CT (left) and MR image (right) acquired on the Radionics Phantom 2，which is configured with a cone, cylinder, cube and sphere. The lines show corresponding SIFT features between CT and MR. Right: Affine transform parameters and results.

Appendix B

Clinical Review

B.1 Sequence of the Randomised Contours

Case No.3		
Slice Number	Blue Contour	Red Contour
22	Clinical	Automatic
23	Clinical	Automatic
24	Automatic	Clinical
25	Clinical	Automatic
26	Automatic	Clinical
27	Automatic	Clinical
28	Clinical	Automatic
29	Clinical	Automatic
30	Clinical	Automatic
31	Automatic	Clinical
32	Clinical	Automatic
33	Clinical	Automatic
34	Clinical	Automatic
35	Clinical	Automatic
36	Clinical	Automatic
37	Clinical	Automatic
38	Automatic	Clinical
39	Automatic	Clinical

Case No.4		
Slice Number	Blue Contour	Red Contour
15	Automatic	Clinical
16	Clinical	Automatic
17	Clinical	Automatic
18	Clinical	Automatic
19	Clinical	Automatic
20	Automatic	Clinical
21	Automatic	Clinical
22	Clinical	Automatic
23	Automatic	Clinical
24	Clinical	Automatic
25	Clinical	Automatic
26	Clinical	Automatic
27	Automatic	Clinical
28	Automatic	Clinical
29	Clinical	Automatic
30	Clinical	Automatic
31	Clinical	Automatic
32	Automatic	Clinical
33	Automatic	Clinical
34	Automatic	Clinical
35	Clinical	Automatic
36	Automatic	Clinical
37	Automatic	Clinical
38	Clinical	Automatic
39	Clinical	Automatic
40	Clinical	Automatic
41	Automatic	Clinical
42	Clinical	Automatic
43	Automatic	Clinical
44	Clinical	Automatic

Case No.5		
Slice Number	Blue Contour	Red Contour
6	Clinical	Automatic
7	Clinical	Automatic
8	Automatic	Clinical
9	Automatic	Clinical
10	Clinical	Automatic
11	Clinical	Automatic
12	Clinical	Automatic
13	Clinical	Automatic
14	Automatic	Clinical
15	Clinical	Automatic
16	Automatic	Clinical
17	Automatic	Clinical
18	Clinical	Automatic
19	Clinical	Automatic
20	Clinical	Automatic
21	Clinical	Automatic
22	Clinical	Automatic
23	Automatic	Clinical
24	Clinical	Automatic
25	Clinical	Automatic
26	Automatic	Clinical
27	Clinical	Automatic
28	Automatic	Clinical
29	Automatic	Clinical
30	Clinical	Automatic
31	Automatic	Clinical
32	Clinical	Automatic
33	Clinical	Automatic
34	Automatic	Clinical

Case No.5 Continued		
Slice Number	Blue Contour	Red Contour
35	Automatic	Clinical
36	Automatic	Clinical
37	Clinical	Automatic
38	Clinical	Automatic
39	Automatic	Clinical
40	Automatic	Clinical
41	Clinical	Automatic
42	Clinical	Automatic
43	Automatic	Clinical

Case No.6		
Slice Number	Blue Contour	Red Contour
25	Automatic	Clinical
26	Clinical	Automatic
27	Clinical	Automatic
28	Clinical	Automatic
29	Automatic	Clinical
30	Clinical	Automatic
31	Clinical	Automatic
32	Automatic	Clinical
33	Clinical	Automatic
34	Clinical	Automatic
35	Clinical	Automatic
36	Clinical	Automatic
37	Clinical	Automatic
38	Automatic	Clinical
39	Automatic	Clinical
40	Automatic	Clinical
41	Clinical	Automatic
42	Clinical	Automatic
43	Clinical	Automatic
44	Automatic	Clinical
45	Clinical	Automatic
46	Clinical	Automatic
47	Clinical	Automatic

Case No.9		
Slice Number	Blue Contour	Red Contour
10	Automatic	Clinical
11	Automatic	Clinical
12	Clinical	Automatic
13	Clinical	Automatic
14	Clinical	Automatic
15	Automatic	Clinical
16	Clinical	Automatic
17	Automatic	Clinical
18	Automatic	Clinical
19	Automatic	Clinical
20	Clinical	Automatic
21	Clinical	Automatic
22	Clinical	Automatic
23	Automatic	Clinical
24	Clinical	Automatic
25	Automatic	Clinical
26	Clinical	Automatic
27	Clinical	Automatic
28	Clinical	Automatic
29	Clinical	Automatic
30	Automatic	Clinical
31	Automatic	Clinical
32	Automatic	Clinical
33	Clinical	Automatic
34	Automatic	Clinical
35	Automatic	Clinical
36	Clinical	Automatic
37	Automatic	Clinical

B.2 Original Grades by SE

Excelent = E, Good = G,Acceptable = A, Not Acceptable = NA

Case No.3

NO.	Color	E	G	A	NA	Comments
22	Blue		✓			
	Red			✓		
23	Blue		✓			
	Red			✓		
24	Blue		✓			
	Red		✓			
25	Blue		✓			
	Red			✓		
26	Blue		✓			
	Red			✓		
27	Blue			✓		
	Red		✓			
28	Blue		✓			
	Red			✓		
29	Blue		✓			
	Red			✓		
30	Blue		✓			
	Red		✓			
31	Blue		✓			
	Red	✓	✓			
32	Blue	✓				
	Red		✓			
33	Blue	✓				
	Red		✓			
34	Blue	✓				
	Red		✓			
35	Blue	✓				
	Red			✓		
36	Blue	✓				
	Red			✓		

NO.	Color	E	G	A	NA	Comments
37	Blue		✓			
	Red			✓		
38	Blue			✓		
	Red		✓			
39	Blue		✓			
	Red		✓			

Doctor : SE CM. Sci : KC

SE
KC

Excelent = E, Good = G,Acceptable = A, Not Acceptable = NA						
Case No.4						
NO.	Color	E	G	A	NA	Comments
15	Blue	✓				
	Red	✓				
16	Blue	✓				
	Red	✓				
17	Blue	!	✓			
	Red	✓				
18	Blue	✓				
	Red		✓			
19	Blue	•	✓			
	Red		✓			
20	Blue		✓			
	Red	✓				
21	Blue		✓			
	Red	✓				
22	Blue	✓				
	Red	✓				
23	Blue	✓				
	Red	✓				
24	Blue	✓				
	Red		✓			
25	Blue	✓				
	Red		✓			
26	Blue	✓				
	Red		✓			
27	Blue		✓			
	Red	✓				
28	Blue		✓			
	Red	✓				
29	Blue	✓				
	Red	•	✓			

NO.	Color	E	G	A	NA	Comments
30	Blue		✓			
	Red		✓			
31	Blue		✓			
	Red		✓			
32	Blue		✓			
	Red	✓				
33	Blue		✓			
	Red	✓				
34	Blue			✓		
	Red	✓				
35	Blue	✓				
	Red			✓		
36	Blue		✓			
	Red	✓				
37	Blue		✓			Slide 38? Red from G not NRG
	Red	✓				
38	Blue	✓				
	Red			✓		
39	Blue	✓				
	Red			✓		
40	Blue		✓			
	Red		✓			
41	Blue			✓		
	Red		✓			
42	Blue		✓			
	Red			✓		
43	Blue			✓		
	Red		✓			
44	Blue		✓			
	Red			✓		

Excelent = E, Good = G,Acceptable = A, Not Acceptable = NA						
Case No.5						
NO.	Color	E	G	A	NA	Comments
6	Blue			✓		
	Red			•		
7	Blue			✓		
	Red		✓			
8	Blue		✓	✓		
	Red			✓		
9	Blue			✓		
	Red			✓		
10	Blue			✓		
	Red			✓		
11	Blue			✓		
	Red		✓			
12	Blue		✓			
	Red			✓		
13	Blue	✓				
	Red	•		✓		
14	Blue		✓			
	Red		✓			
15	Blue		✓			
	Red			✓		
16	Blue		✓			
	Red			✓		
17	Blue			✓		
	Red		✓			
18	Blue	✓				
	Red		✓	✓		
19	Blue	✓				
	Red			✓		
20	Blue	✓				
	Red			✓		

NO.	Color	E	G	A	NA	Comments
21	Blue	✓				
	Red			✓		
22	Blue	✓				
	Red			✓		
23	Blue		✓			
	Red	✓				
24	Blue		✓			
	Red		✓			
25	Blue	✓				
	Red		✓			
26	Blue	✓				
	Red			✓		
27	Blue		✓			
	Red			✓		
28	Blue		✓			
	Red		✓			
29	Blue		✓			
	Red		✓			
30	Blue	✓				
	Red		✓			
31	Blue		✓			
	Red	✓				
32	Blue	✓				
	Red		✓			
33	Blue	✓				
	Red		✓			
34	Blue		✓			
	Red		✓			
35	Blue		✓			
	Red		✓			
36	Blue		✓			
	Red		✓			

NO.	Color	E	G	A	NA	Comments
37	Blue	✓				
	Red		✓			
38	Blue		✓			
	Red		✓			
39	Blue		✓			
	Red		✓			
40	Blue	✓				
	Red		✓			
41	Blue		✓			
	Red		✓			
42	Blue		✓			
	Red			✓		
43	Blue		✓			
	Red		✓			

Excelent = E, Good = G,Acceptable = A, Not Acceptable = NA						
Case No.6						
NO.	Color	E	G	A	NA	Comments
25	Blue		✓			
	Red		✓			
26	Blue		✓			
	Red		✓			
27	Blue	✓				
	Red			✓		
28	Blue	✓				
	Red			✓		
29	Blue			✓		
	Red	✓				
30	Blue	✓				
	Red			✓		
31	Blue	✓				
	Red			✓		
32	Blue		✓			
	Red		✓			
33	Blue		✓			
	Red		✓			
34	Blue	✓				
	Red		✓			
35	Blue	✓				
	Red		✓			
36	Blue	✓				
	Red		✓			
37	Blue	✓				
	Red		✓			
38	Blue	✓				
	Red	✓				
39	Blue	✓				
	Red	✓				

NO.	Color	E	G	A	NA	Comments
40	Blue	✓				
	Red	✓				
41	Blue					
	Red		✓			
42	Blue		✓			
	Red		✓			
43	Blue		✓			
	Red		✓			
44	Blue		✓			
	Red		✓			
45	Blue		✓			
	Red		✓			
46	Blue		✓			
	Red		✓			
47	Blue		✓			
	Red		✓			

Large white into
Surrounding tissues
- need G intensity

Excelent = E, Good = G,Acceptable = A, Not Acceptable = NA						
Case No.9						
NO.	Color	E	G	A	NA	Comments
10	Blue		✓			
	Red		✓			
11	Blue		✓			
	Red		✓			
12	Blue	✓				
	Red		✓			
13	Blue	✓				
	Red		✓			
14	Blue	✓				
	Red		✓			
15	Blue		✓			
	Red	✓				
16	Blue	✓				
	Red		✓			
17	Blue		✓			
	Red	✓				
18	Blue		✓			
	Red	✓				
19	Blue		✓			
	Red	✓				
20	Blue	✓				
	Red		✓			
21	Blue	✓				
	Red		✓			
22	Blue	✓				
	Red		✓			
23	Blue		✓			
	Red	✓				
24	Blue	✓				
	Red			✓		

NO.	Color	E	G	A	NA	Comments
25	Blue			✓		
	Red	✓				
26	Blue	✓				
	Red			✓		
27	Blue	✓				
	Red			✓		
28	Blue	✓				
	Red		✓			
29	Blue		✓			– Blue < GV.
	Red		✓			
30	Blue		✓	✓		
	Red		✓	✓		
31	Blue			✓		
	Red		✓			
32	Blue			✓		
	Red		✓			
33	Blue		✓			
	Red		✓			
34	Blue		✓			
	Red	✓				
35	Blue		✓			– Red = GV.
	Red		✓			
36	Blue		✓			
	Red		✓			
37	Blue		✓			
	Red		✓			– Red GV.

Bibliography

[1] T. Heimann and H. P. Meinzer, "Statistical shape models for 3D medical image segmentation: A review," *Medical Image Analysis*, vol. 13, no. 4, pp. 543–563, 2009.

[2] E. Bianconi, A. Piovesan, F. Facchin, A. Beraudi, R. Casadei, F. Frabetti, L. Vitale, M. C. Pelleri, S. Tassani, F. Piva, S. Perez-Amodio, P. Strippoli, and S. Canaider, "An estimation of the number of cells in the human body.," *Annals of Human Biology*, vol. 40, no. 6, pp. 463–71, 2013.

[3] L. Hayflick, "The limited in vitro lifetime of human diploid cell strains," *Experimental Cell Research*, vol. 37, no. 3, pp. 614–636, 1965.

[4] Cancer Reserach UK, "Incidence , survival and mortality." `http://www.cancerresearchuk.org/cancer-help/about-cancer/what-is-cancer/statistics/incidence-survival-and-mortality`. [Online; accessed 15-May-2015].

[5] K. Saika, T. Sobue, *et al.*, "Epidemiology of breast cancer in Japan and the US," *Japan Medical Association*, vol. 52, no. 1, pp. 39–44, 2009.

[6] F. Bray, J. Lortet-Tieulent, J. Ferlay, D. Forman, and A. Auvinen, "Prostate cancer incidence and mortality trends in 37 European countries: An overview," *European Journal of Cancer*, vol. 46, no. 17, pp. 3040–3052, 2010.

[7] W. F. Regine, J. L. Huhn, R. A. Patchell, W. H. S. Clair, J. Strottmann, A. Meigooni, M. Sanders, and A. B. Young, "Risk of symptomatic brain tumor recurrence and neurologic deficit after radiosurgery alone in patients with newly diagonised brain metastases: results and implications," *International Journal of Radiation Oncology Biology Physics*, vol. 52, no. 2, pp. 333–338, 2002.

[8] A. J. Stephenson, S. F. Shariat, M. J. Zelefsky, M. W. Kattan, E. B. Butler, B. S. Teh, E. a. Klein, P. a. Kupelian, C. G. Roehrborn, D. a. Pistenmaa, H. D. Pacholke, S. L. Liauw, M. S. Katz, S. a. Leibel, P. T. Scardino, and K. M. Slawin, "Salvage radiotherapy for recurrent prostate cancer after radical prostatectomy.," *JAMA : the journal of the American Medical Association*, vol. 291, no. 11, pp. 1325–1332, 2004.

[9] ICRU, "Report 29. Dose specification for reporting external beam therapy with photons and electrons," tech. rep., International Commission on Radiation Units and Measurements, Bethesda, Maryland, 1978.

[10] ICRU, "Report 50. Prescribing, recording, and reporting photon beam therapy," tech. rep., International Commission on Radiation Units and Measurements, Bethesda, Maryland, 1993.

[11] ICRU, "Report 62. Prescribing, recording, and reporting photon beam therapy (supplement to icru report 50)," tech. rep., International Commission on Radiation Units and Measurements, Bethesda, Maryland, 1999.

[12] R. J. H. M. Steenbakkers, J. C. Duppen, I. Fitton, K. E. I. Deurloo, L. J. Zijp, E. F. I. Comans, A. L. J. Uitterhoeve, P. T. R. Rodrigus, G. W. P. Kramer, J. Bussink, K. De Jaeger, J. S. a. Belderbos, P. J. C. M. Nowak, M. Van Herk, and C. R. N. Rasch, "Reduction of observer variation using matched CT-PET for lung cancer delineation: A three-dimensional analysis," *International Journal of Radiation Oncology Biology Physics*, vol. 64, no. 2, pp. 435–448, 2006.

[13] P. Tai, J. Van Dyk, E. Yu, J. Battista, L. Stitt, and T. Coad, "Variability of target volume delineation in cervical esophageal cancer," *International Journal of Radiation Oncology Biology Physics*, vol. 42, no. 2, pp. 277–288, 1998.

[14] M. Yamamoto, Y. Nagata, K. Okajima, T. Ishigaki, R. Murata, T. Mizowaki, M. Kokubo, and M. Hiraoka, "Differences in target outline delineation from CT scans of brain tumours using different methods and different observers," *Radiotherapy and Oncology*, vol. 50, no. 2, pp. 151–156, 1999.

[15] T. Nyholm, J. Jonsson, K. Söderström, P. Bergström, A. Carlberg, G. Frykholm, C. F. Behrens, P. F. Geertsen, R. Trepiakas, S. Hanvey, A. Sadozye, J. Ansari, H. McCallum, J. Frew, R. McMenemin, and B. Zackrisson, "Variability in prostate and seminal vesicle delineations defined on magnetic resonance images, a multi-observer, -center and -sequence study.," *Radiation oncology (London, England)*, vol. 8, no. 1, p. 126, 2013.

[16] J. S. Cooper, S. K. Mukherji, A. Y. Toledano, C. Beldon, I. M. Schmalfuss, R. Amdur, S. Sailer, L. a. Loevner, P. Kousouboris, K. K. Ang, J. Cormack, and J. Sicks, "An evaluation of the variability of tumor-shape definition derived by experienced observers from CT images of supraglottic carcinomas (ACRIN protocol 6658)," *International Journal of Radiation Oncology Biology Physics*, vol. 67, no. 4, pp. 972–975, 2007.

[17] D. P. Huyskens, P. Maingon, L. Vanuytsel, V. Remouchamps, T. Roques, B. Dubray, B. Haas, P. Kunz, T. Coradi, R. Bühlman, R. Reddick, A. V. Esch, and E. Salamon, "A qualitative and a quantitative analysis of an auto-segmentation module for prostate cancer," *Radiotherapy and Oncology*, vol. 90, no. 3, pp. 337–345, 2009.

[18] R. J. H. M. Steenbakkers, J. C. Duppen, I. Fitton, K. E. I. Deurloo, L. Zijp, A. L. J. Uitterhoeve, P. T. R. Rodrigus, G. W. P. Kramer, J. Bussink, K. De Jaeger, J. S. a. Belderbos, A. a. M. Hart, P. J. C. M. Nowak, M. Van Herk, and C. R. N. Rasch, "Observer variation in target volume delineation of lung cancer related to radiation oncologist-computer interaction: A 'Big Brother' evaluation," *Radiotherapy and Oncology*, vol. 77, no. 2, pp. 182–190, 2005.

[19] J. Canny, "A computational approach to edge detection.," *IEEE Transactions on Pattern Analysis and Machine Intelligence*, vol. 8, no. 6, pp. 679–698, 1986.

[20] C. Li, C. Xu, C. Gui, and M. Fox, "Level set evolution without re-initialization: a new variational formulation," in *Proceedings of the IEEE Computer Society Conference on Computer Vision and Pattern Recognition 2005 (CVPR'05)*, vol. 1, pp. 430–436, 2005.

[21] M. Kass, A. Witkin, and D. Terzopoulos, "Snakes: Active contour models," *International Journal of Computer Vision*, vol. 1, no. 4, pp. 321–331, 1988.

[22] D. Pham, "Spatial Models for Fuzzy Clustering," *Computer Vision and Image Understanding*, vol. 84, no. 2, pp. 285–297, 2001.

[23] T. Ojala, M. Pietikäinen, and D. Harwood, "A comparative study of texture measures with classification based on feature distributions," *Pattern Recognition*, vol. 29, no. 1, pp. 51–59, 1996.

[24] R. O. Duda and P. E. Hart, "Use of the Hough transformation to detect lines and curves in pictures.," *Communications of the ACM*, vol. 15, no. 1, pp. 11–15, 1972.

[25] J. A. Sethian, *Level set methods and fast marching methods: evolving interfaces in computational geometry, fluid mechanics, computer vision, and materials science*, vol. 3. Cambridge University Press, 1999.

[26] T. F. Cootes, C. J. Taylor, D. Cooper, and J. Graham, "Active shape models-their training and application," *Computer Vision and Image Understanding*, vol. 61, no. 1, pp. 38–59, 1995.

[27] T. F. Cootes, G. J. Edwards, and C. J. Taylor, "Active appearance models," *IEEE Transactions on Pattern Analysis & Machine Intelligence*, pp. 681–685, 2001.

[28] G. P. Mazzara, R. P. Velthuizen, J. L. Pearlman, H. M. Greenberg, and H. Wagner, "Brain tumor target volume determination for radiation treatment planning through automated MRI segmentation," *International Journal of Radiation Oncology Biology Physics*, vol. 59, no. 1, pp. 300–312, 2004.

[29] A. Rasoulian, R. Rohling, and P. Abolmaesumi, "Group-wise registration of point sets for statistical shape models," *IEEE Transactions on Medical Imaging*, vol. 31, no. 11, pp. 2025–2034, 2012.

[30] A. W. Toga and P. Thompson, "The role of image registration in brain mapping," *Image and Vision Computing*, vol. 19, no. 1-2, pp. 3–24, 2001.

[31] M. Rousson, A. Khamene, M. Diallo, J. C. Celi, and P. Sauer, "Constrained surface evolutions for prostate and bladder segmentation in CT images," in *Computer Vision for Biomedical Image Applications*, vol. 3765 LNCS, pp. 251–260, Springer, 2005.

[32] G. Litjens, R. Toth, W. van de Ven, C. Hoeks, S. Kerkstra, B. van Ginneken, G. Vincent, G. Guillard, N. Birbeck, J. Zhang, R. Strand, F. Malmberg, Y. Ou, C. Davatzikos, M. Kirschner, F. Jung, J. Yuan, W. Qiu, Q. Gao, P. E. Edwards, B. Maan, F. van der Heijden, S. Ghose, J. Mitra, J. Dowling, D. Barratt, H. Huisman, and A. Madabhushi, "Evaluation of prostate segmentation algorithms for MRI: The PROMISE12 challenge," *Medical Image Analysis*, vol. 18, no. 2, pp. 359–373, 2014.

[33] A. Assumus, "Early History of X Raus," *Beam Line*, pp. 10 – 24, 1995.

[34] D. L. Bailey, D. W. Townsend, P. E. Valk, and M. N. Maisey, *Positron emission tomography*. Springer, 2005.

[35] R. C. Orth, M. J. Wallace, and M. D. Kuo, "C-arm Cone-beam CT: General Principles and Technical Considerations for Use in Interventional Radiology," *Journal of Vascular and Interventional Radiology*, vol. 20, no. 7 SUPPL., pp. S538–S544, 2009.

[36] L. W. Goldman, "Principles of CT and CT technology," *Journal of Nuclear Medicine Technology*, vol. 35, no. 3, pp. 115–128; quiz 129–130, 2007.

[37] R. Y. L. Chu, *Radiological Imaging: The Theory of Image Formation, Detection, and Processing. Volume 2 by H. H. Barrett and W. Swindell.* Academic Press, New York, 1983.

[38] R. Acharya, R. Wasserman, J. Stevens, and C. Hinojosa, "Biomedical imaging modalities: a tutorial," *Computerized Medical Imaging and Graphics*, vol. 19, no. 1, pp. 3–25, 1995.

[39] Open MRI, "How MRI Works." `http://www.openmrimtpleasant.com/Microsites/open-mri-mt-pleasant/about/howmriworks/`. [Online; accessed 12-August-2015].

[40] P. Sukovic, "Cone beam computed tomography in craniofacial imaging.," *Orthodontics & Craniofacial Research*, vol. 6 Suppl 1, no. s1, pp. 31–36; discussion 179–182, 2003.

[41] K. Tsiklakis, C. Donta, S. Gavala, K. Karayianni, V. Kamenopoulou, and C. J. Hourdakis, "Dose reduction in maxillofacial imaging using low dose Cone Beam CT," *European Journal of Radiology*, vol. 56, no. 3, pp. 413–417, 2005.

[42] J. Hsieh, *Computed tomography: principles, design, artifacts, and recent advances*. SPIE Bellingham, WA, 2003.

[43] R. L. Drake, *Gray's atlas of anatomy*. Elsevier Health Sciences, 2008.

[44] A. M. R. Agur, A. F. Dalley, and J. C. B. Grant, *Grant's atlas of anatomy*. Lippincott Williams & Wilkins, 2012.

[45] A. R. Padhani, V. S. Khoo, J. Suckling, J. E. Husband, M. O. Leach, and D. P. Dearnaley, "Evaluating the effect of rectal distension and rectal movement on prostate gland position using cine MRI," *International Journal of Radiation Oncology Biology Physics*, vol. 44, no. 3, pp. 525–533, 1999.

[46] F. H. Netter, *Atlas of human anatomy*. Elsevier Health Sciences, 2014.

[47] A. H. Jacobs, L. W. Kracht, A. Gossmann, M. a. Rüger, A. V. Thomas, A. Thiel, and K. Herholz, "Imaging in neurooncology.," *NeuroRx : the journal of the American Society for Experimental NeuroTherapeutics*, vol. 2, no. 2, pp. 333–347, 2005.

[48] D. N. Louis, H. Ohgaki, O. D. Wiestler, W. K. Cavenee, P. C. Burger, A. Jouvet, B. W. Scheithauer, and P. Kleihues, "The 2007 who classification of tumours of the central nervous system," *Acta Neuropathologica*, vol. 114, no. 2, pp. 97–109, 2007.

[49] D. F. Gleason, "Histologic grading of prostate cancer: A perspective," *Human Pathology*, vol. 23, no. 3, pp. 273–279, 1992.

[50] Prostate Cancer Centre, "What does the stage of prostate cancer mean?." `http://prostatecancercentre.co.uk/whatis.html`, 2008. [Online; accessed 19-July-2015].

[51] Varian Medical Systems, "Oncology Solutions." `https://www.varian.com/oncology/solutions`. [Online; accessed 12-Sep-2015].

[52] C. Weltens, J. Menten, M. Feron, E. Bellon, P. Demaerel, F. Maes, W. Van Den Bogaert, and E. Van Der Schueren, "Interobserver variations in gross tumor volume delineation of brain tumors on computed tomography and impact of magnetic resonance imaging," *Radiotherapy and Oncology*, vol. 60, no. 1, pp. 49–59, 2001.

[53] S. Bhide and C. Nutting, "Recent advances in radiotherapy," *BMC Medicine*, vol. 8, no. 1, p. 25, 2010.

[54] A. Wang-Chesebro, P. Xia, J. Coleman, C. Akazawa, and M. Roach, "Intensity-modulated radiotherapy improves lymph node coverage and dose to critical structures compared with three-dimensional conformal radiation therapy in clinically localized prostate cancer," *International Journal of Radiation Oncology Biology Physics*, vol. 66, no. 3, pp. 654–662, 2006.

[55] W. P. M. Mayles, T. Cooper, R. Mackay, J. Staffurth, and M. Williams, "Progress with Intensity-modulated Radiotherapy Implementation in the UK," *Clinical Oncology*, vol. 24, no. 8, pp. 543–544, 2012.

[56] S. S. Ahmad, S. Duke, R. Jena, M. V. Williams, N. G. Burnet, *et al.*, "Advances in radiotherapy," *BMJ*, vol. 345, 2012.

[57] C. Li, R. Huang, Z. Ding, J. C. Gatenby, D. N. Metaxas, and J. C. Gore, "A level set method for image segmentation in the presence of intensity inhomogeneities with application to MRI," *IEEE Transactions on Image Processing*, vol. 20, no. 7, pp. 2007–2016, 2011.

[58] T. F. Chan and L. A. Vese, "Active contours without edges," *IEEE Transactions on Image Processing*, vol. 10, no. 2, pp. 266–277, 2001.

[59] T. F. Cootes, G. J. Edwards, and C. J. Taylor, "Active Appearance Models," in *Proceedings of the European Conference on Computer Vision 1998 (H.Burkhardt & B. Neumann Ed.s)*, vol. 2, pp. 484–498, Springer, 1998.

[60] A. Lanitis, C. J. Taylor, and T. F. Cootes, "Automatic interpretation and coding of face images using flexible models," *IEEE Transactions on Pattern Analysis and Machine Intelligence*, vol. 19, no. 7, pp. 743–756, 1997.

[61] P. M. Pierorazio, P. C. Walsh, A. W. Partin, and J. I. Epstein, "Prognostic Gleason grade grouping: Data based on the modified Gleason scoring system," *BJU International*, vol. 111, no. 5, pp. 753–760, 2013.

[62] M. A. Grayson, "The heat equation shrinks embedded plane curves to round points," *Journal of Differential Geometry*, vol. 26, no. 2, pp. 285–314, 1987.

[63] J. Sethian, "Level Set ethods: An Act of Violence," *American Scientist*, vol. 85, no. 3, 1997.

[64] P. S. Liao, T. S. Chen, and P. C. Chung, "A fast algorithm for multilevel thresholding," *Journal of Information Science and Engineering*, vol. 17, no. 5, pp. 713–727, 2001.

[65] M. Iwanowski and J. Serra, "Morphological interpolation and color images," in *Proceedings of the International Conference on Image Analysis and Processing, ICIAP 1999*, pp. 50–57, IEEE, 1999.

[66] B. Jähne, "Texture," in *Digital Image Processing*, pp. 383–394, Springer Berlin Heidelberg, 1997.

[67] D. Montgomery, K. Cheng, Y. Feng, D. McLaren, S. Erridge, S. McLauglin, S. Campbell, and W. Nailon, "Predicting the occurrence of radiation induced pneumonitis by texture analysis of ct images from lung cancer patients," in *MICCAI Workshop on Pulmonary Image Analysis*, 2013.

[68] C. E. Shannon, "A mathematical theory of communication," *ACM SIGMOBILE Mobile Computing and Communications Review*, vol. 5, no. 1, p. 3, 2001.

[69] B. Van Ginneken, A. F. Frangi, J. J. Staal, B. M. Ter Haar Romeny, and M. A. Viergever, "Active shape model segmentation with optimal features," *IEEE Transactions on Medical Imaging*, vol. 21, no. 8, pp. 924–933, 2002.

[70] N. Aggarwal, "First and Second Order Statistics Features for Classification of Magnetic Resonance Brain Images," *Journal of Signal and Information Processing*, vol. 03, no. 02, pp. 146–153, 2012.

[71] C. Xu, J. L. Prince, and B. Hall, "Snakes , Shapes , and Gradient Vector Flow 1 Introduction," *IEEE Transactions on Image Processing*, vol. 7, no. 3, pp. 1–23, 1997.

[72] D. Marr and E. Hildreth, "Theory of edge detection," *Proceedings of the Royal Society of London B: Biological Sciences*, vol. 207, no. 1167, pp. 187–217, 1980.

[73] T. F. Cootes and C. J. Taylor, "Statistical models of appearance for medical image analysis and computer vision," *Medical Imaging 2001*, vol. 8, pp. 236–248, 2001.

[74] R. De Maesschalck, D. Jouan-Rimbaud, and D. L. Massart, "The Mahalanobis distance," *Chemometrics and Intelligent Laboratory Systems*, vol. 50, no. 1, pp. 1–18, 2000.

[75] N. Betrouni, A. Iancu, P. Puech, S. Mordon, and N. Makni, "ProstAtlas: A digital morphologic atlas of the prostate," *European Journal of Radiology*, vol. 81, no. 9, pp. 1969–1975, 2012.

[76] D. Rueckert, L. I. Sonoda, C. Hayes, D. L. Hill, M. O. Leach, and D. J. Hawkes, "Nonrigid registration using free-form deformations: application to breast MR images.," *IEEE transactions on medical imaging*, vol. 18, no. 8, pp. 712–721, 1999.

[77] O. Van Kaick, H. Zhang, G. Hamarneh, and D. Cohen-Or, "A survey on shape correspondence," in *Proceedings of the Computer Graphics Forum*, vol. 30, pp. 1681–1707, Wiley Online Library, 2011.

[78] P. J. Besl and N. D. McKay, "A method for registration of 3-D shapes," *IEEE Transactions on Pattern Analysis and Machine Intelligence*, vol. 14, no. 2, pp. 239–256, 1992.

[79] Z. Zhang, "Iterative point matching for registration of free form curves and surfaces," *International Journal of Computer Vision*, vol. 12, no. 2, pp. 119–152, 1994.

[80] K. S. Arun, T. S. Huang, and S. D. Blostein, "Least-squares fitting of two 3-d point sets," *IEEE Transactions on Pattern Analysis and Machine Intelligence*, no. 5, pp. 698–700, 1987.

[81] S. Gold, A. Rangarajan, C. P. Lu, S. Pappu, and E. Mjolsness, "New algorithms for 2d and 3d point matching: Pose estimation and correspondence," *Pattern recognition*, vol. 31, no. 8, pp. 1019–1031, 1998.

[82] H. Chui and A. Rangarajan, "A new algorithm for non-rigid point matching," in *Proceedings of the IEEE Conference on Computer Vision and Pattern Recognition,2000*, vol. 2, pp. 44–51, IEEE, 2000.

[83] R. Sibson and G. Stone, "Computation of thin-plate splines," *SIAM Journal on Scientific and Statistical Computing*, vol. 12, no. 6, pp. 1304–1313, 1991.

[84] A. Myronenko, X. Song, and M. A. Carreira-Perpinán, "Non-rigid point set registration: Coherent point drift," in *Advances in Neural Information Processing Systems*, pp. 1009–1016, 2006.

[85] A. L. Yuille and N. M. Grzywacz, "The Motion Coherence Theory," in *Proceedings of the Second International Conference on Computer Vision*, pp. 344–353, 1988.

[86] J. P. Pluim and J. M. Fitzpatrick, "Image registration," *Medical Imaging, IEEE Transactions on Medical Imaging*, vol. 22, no. 11, pp. 1341–1343, 2003.

[87] D. L. Hill, P. G. Batchelor, M. Holden, and D. J. Hawkes, "Medical image registration," *Physics in Medicine and Biology*, vol. 1, no. 3, p. R1, 2001.

[88] B. Glocker, N. Komodakis, G. Tziritas, N. Navab, and N. Paragios, "Dense image registration through mrfs and efficient linear programming," *Medical Image Analysis*, vol. 12, no. 6, pp. 731–741, 2008.

[89] Y. Feng, K. Cheng, Y. Lawrence, L. Forrest, D. B. McLaren, S. McLaughlin, D. J. Argyle, and W. H. Nailon, "A new image registration framework for improving radiotherapy delivery," in *Proceedings of the Symposium on Small Animal RadioTherapy , Maastricht, the Netherlands*, 2013.

[90] G. B. Huang, M. Ramesh, T. Berg, and E. Learned-Miller, "Labeled faces in the wild: A database for studying face recognition in unconstrained environments," tech. rep., Technical Report 07-49, University of Massachusetts, Amherst, 2007.

[91] S. Lee, G. Wolberg, and S. Y. Shin, "Scattered data interpolation with multiple B-splines," *IEEE Transactions on Visualization and Computer Graphics*, vol. 3, no. 3, pp. 228–244, 1997.

[92] J. Talairach and P. Tournoux, "Co-Planar Stereotaxis Atlas of the Human Brain: : an approach to cerebral imaging.," *Direct*, vol. 270, p. 132, 1988.

[93] M. Lorenzo-Valdes, G. I. Sanchez-Ortiz, R. H. Mohiaddin, and D. Rueckert, "Atlas-based segmentation and tracking of 3D cardiac MR images using non-rigid registration," in *International Conference on Medical Image Computing And Computer-Assisted Intervention -MICCAI 2002*, vol. 2488, pp. 642–650, Springer, 2002.

[94] X. Han, M. S. Hoogeman, P. C. Levendag, L. S. Hibbard, D. N. Teguh, P. Voet, A. C. Cowen, and T. K. Wolf, "Atlas-based auto-segmentation of head and neck CT images," in *Medical Image Computing and Computer-Assisted Intervention-MICCAI 2008*, pp. 434–441, Springer Berlin Heidelberg, 2008.

[95] A. Guimond, J. Meunier, and J. Thirion, "Average brain models: A convergence study," *Computer vision and image ...*, vol. 77, no. 2, pp. 192–210, 2000.

[96] T. Chen, S. Kim, S. Goyal, S. Jabbour, J. Zhou, G. Rajagopal, B. Haffty, and N. Yue, "Object-constrained meshless deformable algorithm for high speed 3D nonrigid registration between CT and CBCT.," *Medical Physics*, vol. 37, no. 1, pp. 197–210, 2010.

[97] U. Malsch, C. Thieke, P. E. Huber, and R. Bendl, "An enhanced block matching algorithm for fast elastic registration in adaptive radiotherapy.," *Physics in Medicine and Biology*, vol. 51, no. 19, pp. 4789–4806, 2006.

[98] M. J. Costa, H. Delingette, S. Novellas, and N. Ayache, "Automatic segmentation of bladder and prostate using coupled 3d deformable models," in *Medical Image Computing and Computer-Assisted Intervention-MICCAI 2007*, pp. 252–260, Springer, 2007.

[99] M. Prastawa, E. Bullitt, S. Ho, and G. Gerig, "A brain tumor segmentation framework based on outlier detection," *Medical Image Analysis*, vol. 8, no. 3, pp. 275–283, 2004.

[100] S. Osher and J. A. Sethian, "Fronts propagating with curvature dependent speed: Algorithms based on Hamilton-Jacobi formulations," *Journal of Computational Physics*, vol. 79, no. 1, pp. 12–49, 1987.

[101] I. G. Petrovsky, *Lectures on partial differential equations.* Courier Corporation, 2012.

[102] T. F. Chan and L. A. Vese, "Active contours without edges," *IEEE Transactions on Image Processing*, vol. 10, no. 2, pp. 266–277, 2001.

[103] N. Kozic, S. Weber, P. Buchler, C. Lutz, N. Reimers, M. a. Gonzalez Ballester, and M. Reyes, "Optimisation of orthopaedic implant design using statistical shape space analysis based on level sets.," *Medical Image Analysis*, vol. 14, no. 3, pp. 265–275, 2010.

[104] T. Dietenbeck, M. Alessandrini, D. Barbosa, J. D'hooge, D. Friboulet, and O. Bernard, "Detection of the whole myocardium in 2D-echocardiography for multiple orientation using a geometrically constrained level-set," *Medical Image Analysis*, vol. 16, pp. 386–401, 2012.

[105] C. Baillard, P. Hellier, and C. Barillot, "Segmentation of 3d brain structures using level sets and dense registration," in *Proceedings of the IEEE Workshop on Mathematical Methods in Biomedical Image Analysis, 2000.*, pp. 94–101, IEEE, 2000.

[106] H. Scherl, J. Hornegger, M. Prümmer, and M. Lell, "Semi-automatic level-set based segmentation and stenosis quantification of the internal carotid artery in 3D CTA data sets," *Medical Image Analysis*, vol. 11, no. 1, pp. 21–34, 2007.

[107] D. Mumford and J. Shah, "Optimal Approximations by piecewise smooth functions and associated variational problems," *Communications on Pure and Applied Mathematics*, vol. 42, no. 5, pp. 577–685, 1989.

[108] A. Desolneux, L. Moisan, and J.-M. Morel, "Variational Snake Theory," *Geometric Level Set Methods in Imaging, Vision, and Graphics*, pp. 79–99, 2003.

[109] P. A. Yushkevich, J. Piven, H. C. Hazlett, R. G. Smith, S. Ho, J. C. Gee, and G. Gerig, "User-guided 3D active contour segmentation of anatomical structures: significantly improved efficiency and reliability," *Neuroimage*, vol. 31, no. 3, pp. 1116–1128, 2006.

[110] S. Ho, L. Bullitt, and G. Gerig, "Level-set evolution with region competition: automatic 3-d segmentation of brain tumors," in *Proceedings of the 16th International Conference on Pattern Recognition, 2002*, vol. 1, pp. 532–535, IEEE, 2002.

[111] Y. Zhu and H. Yan, "Computerized tumor boundary detection using a Hopfield neural network.," *IEEE Transactions on Medical Imaging*, vol. 16, no. 1, pp. 55–67, 1997.

[112] D.-J. Kroon, "Active shape model (asm) and active appearance model (aam)." Matlab Exchange, Feb 2010.

[113] F. L. Bookstein, *Morphometric Tools for Landmark Data*, vol. 10. Cambridge University Press, 1992.

[114] I. Jolliffe, *Principal Component Analysis*. Wiley Online Library, 2002.

[115] T. F. Cootes, G. J. Edwards, and C. J. Taylor, "Comparing Active Shape Models with Active Appearance Models," in *Proceedings of the British Machine Conference (BMVC)*, 1999.

[116] J. V. Stough, R. E. Broadhurst, S. M. Pizer, and E. L. Chaney, "Regional appearance in deformable model segmentation," in *Information Processing in Medical Imaging*, pp. 532–543, Springer, 2007.

[117] Q. Fenga, M. Foskey, S. Tang, W. Chen, and D. Shen, "Segmenting ct prostate images using population and patient-Specific statistics for radiotherapy," in *Proceedings of the 2009 IEEE International Symposium on Biomedical Imaging: From Nano to Macro, ISBI 2009*, pp. 282–285, IEEE, 2009.

[118] Y. Jeong and R. J. Radke, "Modeling inter- and intra-patient anatomical variation using a bilinear model," in *Proceedings of the IEEE Computer Society Conference on Computer Vision and Pattern Recognition*, vol. 2006, p. 76, IEEE, 2006.

[119] R. E. Broadhurst, J. Stough, S. Pizer, and E. Chaney, "A Statistical Appearance Model Based on Intensity Quantile Histograms," in *Proceedings of the 3rd IEEE International Symposium on Biomedical Imaging: Macro to Nano,2006*, pp. 422–425, IEEE, 2006.

[120] R. E. Broadhurst, J. Stough, S. M. Pizer, and E. L. Chaney, "Histogram statistics of local model-relative image regions," in *Deep Structure, Singularities, and Computer Vision*, pp. 72–83, Springer, 2005.

[121] S. Chen, D. M. Lovelock, and R. J. Radke, "Segmenting the prostate and rectum in CT imagery using anatomical constraints," *Medical Image Analysis*, vol. 15, no. 1, pp. 1–11, 2011.

[122] P. A. Yushkevich, J. Piven, H. C. Hazlett, R. G. Smith, S. Ho, J. C. Gee, and G. Gerig, "User-guided 3D active contour segmentation of anatomical structures: significantly improved efficiency and reliability," *Neuroimage*, vol. 31, no. 3, pp. 1116–1128, 2006.

[123] K. Poon, G. Hamarneh, and R. Abugharbieh, "Segmentation of complex objects with non-spherical topologies from volumetric medical images using 3D livewire," in *SPIE Medical Imaging 2007*, pp. 1–10, 2007.

[124] C. J. Armstrong, B. L. Price, and W. a. Barrett, "Interactive segmentation of image volumes with Live Surface," *Computers and Graphics (Pergamon)*, vol. 31, no. 2, pp. 212–229, 2007.

[125] J. Zhou and J. C. Rajapakse, "Segmentation of subcortical brain structures using fuzzy templates," *NeuroImage*, vol. 28, no. 4, pp. 915–924, 2005.

[126] S. L. Hartmann, M. H. Parks, P. R. Martin, and B. M. Dawant, "Automatic 3-D segmentation of internal structures of the head in MR images using a combination of similarity and free-form transformations: Part II, validation on severely atrophied brains.," *IEEE transactions on medical imaging*, vol. 18, no. 10, pp. 917–926, 1999.

[127] N. Birkbeck, D. Cobzas, M. Jagersand, A. Murtha, and T. Kesztyues, "An interactive graph cut method for brain tumor segmentation," in *Workshop on Applications of Computer Vision, WACV 2009*, pp. 1–7, Dec. 2009.

[128] J. J. Corso, E. Sharon, S. Dube, S. El-Saden, U. Sinha, and A. Yuille, "Efficient multilevel brain tumor segmentation with integrated bayesian model classification," *IEEE Transactions on Medical Imaging*, vol. 27, no. 5, pp. 629–640, 2008.

[129] N. K. Subbanna, D. Precup, D. L. Collins, and T. Arbel, "Hierarchical probabilistic Gabor and MRF segmentation of brain tumours in MRI volumes," in *Medical Image Computing and Computer-Assisted Intervention–MICCAI 2013*, pp. 751–758, Springer, 2013.

[130] K. Aloui and M. S. Naceur, "3D Brain Tumor Segmentation Using Level- Sets Method and Meshes Simplification from Volumetric MR Images," *Engineering and Technology*, vol. 57, pp. 127–131, 2009.

[131] M. Schmidt, I. Levner, R. Greiner, A. Murtha, and A. Bistritz, "Segmenting brain tumors using alignment-based features," in *Proceedings of the ICMLA 2005: Fourth International Conference on Machine Learning and Applications*, vol. 2005, pp. 218–220, 2005.

[132] J. Weickert and H. Scharr, "A Scheme for Coherence-Enhancing Diffusion Filtering with Optimized Rotation Invariance," *Journal of Visual Communication and Image Representation*, vol. 13, no. 1-2, pp. 103–118, 2002.

[133] R. C. Gonzalez and R. E. Woods, *Digital Image Processing*. Prentice Hall, 2001.

[134] R. D. Nowak, "Wavelet-based Rician noise removal for magnetic resonance imaging," *IEEE Transactions on Image Processing*, vol. 8, pp. 1408–1419, Oct. 1999.

[135] A. Macovski, "Noise in MRI," *Magnetic Resonance in Medicine*, vol. 36, no. 3, pp. 494–497, 1996.

[136] M. A. Yousuf and M. N. Nobi, "A New Method to Remove Noise in Magnetic Resonance and Ultrasound Images," *Journal of Scientific Research*, vol. 3, no. 1, pp. 81–89, 2010.

[137] H. Gudbjartsson and S. Patz, "The Rician distribution of noisy MRI data," *Magnetic Resonance in Medicine*, vol. 34, no. 6, pp. 910–914, 1995.

[138] A. Fick, "On liquid diffusion," *Journal of Membrane Science*, vol. 100, no. 1, pp. 33–38, 1995.

[139] T. Sørensen, "A method of establishing groups of equal amplitude in plant sociology based on similarity of species and its application to analyses of the vegetation on danish commons," *Biologiske Skrifter*, vol. 5, pp. 1–34, 1948.

[140] R. T. Rockafellar and R. J.-B. Wets, *Variational analysis*, vol. 317. Springer Science & Business Media, 2009.

[141] B. Menze, A. Jakab, S. Bauer, J. Kalpathy-Cramer, K. Farahani, J. Kirby, Y. Burren, N. Porz, J. Slotboom, R. Wiest, L. Lanczi, E. Gerstner, M.-A. Weber, T. Arbel, B. Avants, N. Ayache, P. Buendia, D. Collins, N. Cordier, J. Corso, A. Criminisi, T. Das, H. Delingette, C. Demiralp, C. Durst, M. Dojat, S. Doyle, J. Festa, F. Forbes, E. Geremia, B. Glocker, P. Golland, X. Guo, A. Hamamci, K. Iftekharuddin, R. Jena, N. John, E. Konukoglu, D. Lashkari, J. Mariz, R. Meier, S. Pereira, D. Precup, S. Price, T. Riklin Raviv, S. Reza, M. Ryan, D. Sarikaya, L. Schwartz, H.-C. Shin, J. Shotton, C. Silva, N. Sousa, N. Subbanna, G. Szekely, T. Taylor, O. Thomas, N. Tustison, G. Unal, F. Vasseur, M. Wintermark, D. H. Ye, L. Zhao, B. Zhao, D. Zikic, M. Prastawa, M. Reyes, and K. Van Leemput, "The multimodal brain tumor image segmentation benchmark (brats)," *Medical Imaging, IEEE Transactions on*, vol. 34, pp. 1993–2024, Oct 2015.

[142] X. Guo, L. Schwartz, and B. Zhao, "Semi-automatic segmentation of multimodal brain tumor using active contours," *Multimodal Brain Tumor Segmentation*, p. 27, 2013.

[143] P. A. Humphrey, *Prostate Pathology*. American Society for Clinical Pathology Chicago, Ill, 2003.

[144] B. G. Hollmann, B. van Triest, G. Ghobadi, G. Groenendaal, J. de Jong, H. G. van der Poel, and U. A. van der Heide, "Gross tumor volume and clinical target volume in prostate cancer: How do satellites relate to the index lesion," *Radiotherapy and Oncology*, 2015.

[145] M. Andreoiu and L. Cheng, "Multifocal prostate cancer: biologic, prognostic, and therapeutic implications," *Human Pathology*, vol. 41, no. 6, pp. 781–793, 2010.

[146] C. G. Roehrborn and J. D. McConnell, "Benign prostatic hyperplasia: etiology, pathophysiology, epidemiology, and natural history," *Campbell-Walsh Urology. 9th ed. Philadelphia, Pa: Saunders Elsevier*, 2007.

[147] V. Pekar, T. McNutt, and K. Michael, "Automated model-based organ delineation for radiation therapy planning in the prostate region," *International Journal of Radiation Oncology Biology Physics*, vol. 57, no. 2, p. S206, 2003.

[148] D. Freedman, R. Radke, T. Z. T. Zhang, Y. J. Y. Jeong, and G. Chen, "Model-Based Multi-Object Segmentation via Distribution Matching," in *Computer Vision and Pattern Recognition Workshop, 2004. CVPRW'04. Conference on*, p. 11, IEEE, 2004.

[149] Q. Song, Y. Liu, Y. Liu, P. K. Saha, M. Sonka, and X. Wu, "Graph search with appearance and shape information for 3-D prostate and bladder segmentation," in *Medical Image Computing and Computer-Assisted Intervention-MICCAI 2010*, pp. 172–180, Springer, 2010.

[150] A. Khamene, D. Zikic, M. Diallo, T. Boettger, and E. Rietzel, "A novel intensity similarity metric with soft spatial constraint for a deformable image registration problem in radiation therapy," in *Medical Image Computing and Computer-Assisted Intervention-MICCAI 2009*, pp. 828–836, Springer, 2009.

[151] C. Lu, S. Chelikani, Z. Chen, X. Papademetris, L. H. Staib, and J. S. Duncan, "Integrated segmentation and nonrigid registration for application in prostate image-guided radiotherapy," in *Medical Image Computing and Computer-Assisted Intervention-MICCAI 2010*, pp. 53–60, Springer, 2010.

[152] S. Thörnqvist, J. B. Petersen, M. Höyer, L. N. Bentzen, and L. P. Muren, "Propagation of target and organ at risk contours in radiotherapy of prostate cancer using deformable image registration.," *Acta oncologica (Stockholm, Sweden)*, vol. 49, no. 7, pp. 1023–1032, 2010.

[153] F. Martínez, E. Romero, G. Dréan, A. Simon, P. Haigron, R. De Crevoisier, and O. Acosta, "Segmentation of pelvic structures for planning ct using a geometrical shape model tuned by a multi-scale edge detector," *Physics in medicine and biology*, vol. 59, no. 6, p. 1471, 2014.

[154] Y. Shao, Y. Gao, Q. Wang, X. Yang, and D. Shen, "Locally-constrained boundary regression for segmentation of prostate and rectum in the planning ct images," *Medical image analysis*, vol. 26, no. 1, pp. 345–356, 2015.

[155] G. Vincent, G. Guillard, and M. Bowes, "Fully automatic segmentation of the prostate using active appearance models," in *Medical Image Computing and Computer Assisted Intervention - MICCAI 2012 Grand Challenge: Prostate MR Image Segmentation*, vol. 7, 2012.

[156] D. J. Kroon, P. Kowalski, W. Tekieli, E. Reeuwijk, D. Saris, and C. H. Slump, "MRI based knee cartilage assessment," in *Proceedings of the SPIE Medical Imaging 2012*, pp. 83151V–83151V, International Society for Optics and Photonics, 2012.

[157] J. L. H. R. Bosch, K. Tilling, a. M. Bohnen, C. H. Bangma, and J. L. Donovan, "Establishing normal reference ranges for prostate volume change with age in the population-based Krimpen-study: Prediction of future prostate volume in individual men," *The Prostate*, vol. 67, no. 16, pp. 1816–1824, 2007.

[158] M. Sheikh, O. Al-Saeed, E. O. Kehinde, T. Sinan, J. T. Anim, and M. Sheikh, "Utility of volume adjusted prostate specific antigen density in the diagnosis of prostate cancer in Arab men," *International Urology and Nephrology*, vol. 37, no. 4, pp. 721–726, 2005.

[159] A. Tanimoto, J. Nakashima, H. Kohno, H. Shinmoto, and S. Kuribayashi, "Prostate cancer screening: The clinical value of diffusion-weighted imaging and dynamic MR imaging in combination with T2-weighted imaging," *Journal of Magnetic Resonance Imaging*, vol. 25, no. 1, pp. 146–152, 2007.

[160] T. Hambrock, C. Hoeks, C. Hulsbergen-Van de Kaa, T. Scheenen, J. Fütterer, S. Bouwense, I. van Oort, F. Schröder, H. Huisman, and J. Barentsz, "Prospective

assessment of prostate cancer aggressiveness using 3-T diffusion-weighted magnetic resonance imaging-guided biopsies versus a systematic 10-core transrectal ultrasound prostate biopsy cohort," *European Urology*, vol. 61, no. 5, pp. 177–184, 2012.

[161] R. Toth, B. N. Bloch, E. M. Genega, N. M. Rofsky, R. E. Lenkinski, M. A. Rosen, A. Kalyanpur, S. Pungavkar, and A. Madabhushi, "Accurate prostate volume estimation using multifeature active shape models on T2-weighted MRI," *Academic radiology*, vol. 18, no. 6, pp. 745–754, 2011.

[162] J. E. Sylvester, P. D. Grimm, J. C. Blasko, J. Millar, P. F. Orio, S. Skoglund, R. W. Galbreath, and G. Merrick, "15-Year biochemical relapse free survival in clinical Stage T1-T3 prostate cancer following combined external beam radiotherapy and brachytherapy; Seattle experience," *International Journal of Radiation Oncology Biology Physics*, vol. 67, no. 1, pp. 57–64, 2007.

[163] T. Y. Lim, R. J. Stafford, R. J. Kudchadker, M. Sankaranarayanapillai, G. Ibbott, A. Rao, K. S. Martirosyan, and S. J. Frank, "MRI characterization of cobalt dichloride-N-acetyl cysteine (C4) contrast agent marker for prostate brachytherapy.," *Physics in Medicine and Biology*, vol. 59, no. 10, pp. 2505–2516, 2014.

[164] G. Li, D. Citrin, K. Camphausen, B. Mueller, C. Burman, B. Mychalczak, R. W. Miller, and Y. Song, "Advances in 4D medical imaging and 4D radiation therapy," *Technology in Cancer Research & Treatment*, vol. 7, no. 1, pp. 67–81, 2008.